



**DEVELOPMENT AND CHARACTERISATION OF  
A NOVEL OPTICAL SURFACE DEFECT  
DETECTION SYSTEM**

By

Mohammad Abu Hana Mustafa Kamal, B.Sc. Eng.

This thesis is submitted as the fulfilment of the  
requirement for the award of degree of

Master of Engineering (M. Eng)

by research

Research Supervisors:

Dr. Dermot Brabazon and Professor M.S.J. Hashmi

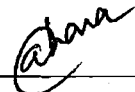
September 2005

School of Mechanical & Manufacturing Engineering  
Dublin City University

## DECLARATION

I hereby certify that this material, which I now submit for assessment on the programme of study leading to the award of Master of Engineering is entirely my own work and has not been taken from the work of others save to the extent that such work has been cited and acknowledged within the text of my work

Signed: \_\_\_\_\_

  
Candidate

ID No.: 52175103

Date: 19 September 2005

## ACKNOWLEDGEMENTS

I would like to express my sincere thanks and gratitude to my project supervisor Dr. Dermot Brabazon for his supervision and guidance at all stages of my research. I am also very much grateful to my other supervisor Professor M.S.J. Hashmi for giving me the opportunity and facilities to carry out my study.

I am indebted to Michael May, Liam Domican, Keith Hickey and all other staffs in the school for the contribution they made and the co-operation they offered to the success of the project.

Finally, I would like to thank to all of my family members, especially my wife Sultana Begum for her love and help throughout my study periods.

---

*Dedicated*

To

*My Wife Sultana Begum*

---

## Abstract

# Development and characterisation of a novel optical surface defect detection system

By

Mohammad Abu Hana Mustafa Kamal

The objective of this project was to develop and characterise a novel optical high-speed online surface defect detection system. The inspection system is based on the principle of optical triangulation and provides a non-contact method of determining 3D profile of a diffuse surface. Primary components of the developed system consist of a diode laser, CCf15 CMOS camera, and two PC controlled servomotors. Control of the sample movement, image capturing, and generation of 3D surface profiles was programmed in LabView software. Inspection of the captured data was facilitated by creating a program to virtually present the 3D scanned surface and calculate requested surface roughness parameters. The servomotors were used to move the sample in the X and Y directions with a resolution of 0.05  $\mu\text{m}$ . The developed non-contact online surface-profiling device allows for quick high-resolution surface scanning and inspection. The developed system was successfully used to generate automated 2D surface profiles, 3D surface profiles and surface roughness measurement on different sample material surfaces. This automated inspection facility has X-Y scanning area capacity of 12 by 12 mm. In order to characterise and calibrate the developed profiling system, surface profiles measured by the system were compared to optical microscope, binocular microscope, AFM and Mitutoyo Surftest – 402 measurement of the same surfaces.

## Table of contents

	Page No.
Title	I
Declaration	II
Acknowledgements	III
Dedication	IV
Abstract	V
Table of Contents	VI
List of Tables	X
List of Figures	XI
Glossary	XV
CHAPTER ONE      INTRODUCTION	
1      Introduction	1
CHAPTER TWO      LITERATURE SURVEY	
2.1      Surface profile	4
2.2      Roughness profile	4
2.3      Surface inspection	5
a. On-line Inspection	
b. Off-line Inspection	
2.4      Surface defects	7
2.5      Surface roughness	7
2.6      Surface roughness parameters	8
2.6.1    Arithmetic mean roughness ( $R_a$ )	9
2.6.2    Root-mean-square average ( $R_q$ )	10
2.6.3    Skewness, Kurtosis and Maximum height	10
2.7      Roughness measurement	11
2.8      Types of scanner for surface profiling	11
2.8.1    Contact scanning - Touch probe	12
2.8.2    Non-contact scanning	12
a. Laser strip triangulation	12

	b. Optical triangulation using structured light	13
2.9	Laser technology	14
2.9.1	Laser diode module	14
2.9.2	Line generators	15
2.9.3	Intensity distribution of laser line	16
2.9.4	Laser line length	17
2.9.5	Focal spot size and depth of focus (DOF) of the laser beam	18
2.9.6	Laser applications	20
	a. Low-power application	
	b. High-power application	
2.9.7	Advantages & disadvantages of laser	21
2.10	Servo technology	22
2.11	Triangulation	23
2.11.1	Optical triangulation principle	23
2.11.2	Error in Triangulation System	25
	a. Random Error	
	b. Systematic Error	
2.11.3	Advantages and Disadvantages of Triangulation System	25
2.11.4	Angle of triangulation and shadow effect	26
2.11.5	Spot size	27
2.11.6	Brightness and contrast	27
2.11.7	Peak detection algorithms	28
2.11.8	Image resolution	28
2.12	Interferometry	29
2.12.1	Speckle interferometry	30
2.12.2	Electronic speckle-pattern interferometry (ESPI)	31
2.12.3	Speckle pattern shearing interferometry	32
2.12.4	Application of interferometry	32
2.13	Nomarski microscope	33
2.14	X-ray micro tomography	34

### CHAPTER THREE                      LASER TRIANGULATION SCANNING (LTS) SYSTEM EXPERIMENTAL SETUP

3.1	Laser diode module	37
3.2	Image capturing system	38
3.3	Motorised translation stage	40
3.3.1	Motion Integrator	41
3.3.2	Tuning servos with Motion Integrator	42
3.3.3	Quadrature incremental encoder	42
3.3.4	Setting the Allowable Following Error	42
3.3.5	Servo tuning procedure	43

### CHAPTER FOUR                      SOFTWARE DEVELOPMENT

4.1	Software development for automated surface scanning	45
4.1.1	Camera interfacing in LabView	47
4.1.2	Control sample movement and data processing procedure	49
4.1.3	3D surface reconstruction	51
4.2	Software development for laser line scanning system	53
4.3	Surface roughness measurement	56
4.4	2D profiles from 3D surface map	58

### CHAPTER FIVE                      AUTOMATED SCANS RESULTS

5.1	Introduction	59
5.2	System parameters	59
5.2.1	Camera viewing length, focal spot size and depth of focus	59
5.2.2	Noise threshold for data processing	62
5.2.3	Depth calibration factor	63
5.2.4	Depth calibration factor from known $R_a$ sample	65
5.3	Automated surface scan	66
5.3.1	Automated scan of a copper sample	67
5.3.2	Automated scan of a stainless steel sample	70
5.3.3	Automated scan of a plastic sample	73
5.3.5	Automated scan with different lens system	76

5.4	Compare with optical microscope	79
5.5	System depth repeatability	80
5.6	Surface roughness parameters measurement results	82
5.7	Surface scan by the automated line scan system	84

## CHAPTER SIX                      DISCUSSION

6.1	Discussion	87
6.2	Measurement error	89
6.3	Effect of spot size on the surface profiling system	94
6.4	System speed	96
6.5	System resolution	96

## CHAPTER SEVEN                      CONCLUSIONS AND RECOMMENDATIONS

7.1	Conclusions	98
7.2	Recommendations for future work	99

REFERENCES	100
------------	-----

## APPENDIX

Appendix A	OPERATION PRINCIPLE	105
Appendix B	PROPERTIES OF LASER LIGHT	112
Appendix C	LASER DIODES MODULES SPECIFICATIONS	119
Appendix D	CAMERA SPECIFICATIONS	123
Appendix E	MOTION CONTROL HARDWARE'S	127
Appendix F	SERVO TUNING PROCEDURE	131
Appendix G	CALL LIBRARY FUNCTION GENERAL CONFIGURATION	136
Appendix H	CCAPI.H HEADER FILE	141
Appendix I	CAMERA PROGRAM	147

LIST OF TABLES	Page
Table 3.1	Specifications of the laser diode modules 38
Table 3.2	Technical specifications of Fuga15 sensor 39
Table 5.1	Camera viewing length with different focusing lens 60
Table 5.2	Depth calibration factor in micrometers per pixel for different filter values 64
Table 5.3	Depth calibration factor from precision specimen sample 65
Table 5.4	Scan parameters for the copper sample 67
Table 5.5	Scan parameters for the steel sample 71
Table 5.6	Scan parameters for the plastic sample 74
Table 5.7	Depth repeatability of the automated surface scanning system 82
Table 5.8	Surface roughness parameters of a stainless steel surface 83
Table 5.9	Surface roughness parameters of a copper surface 83
Table 5.10	Surface roughness parameters measurements results 84
Table 5.11	Line scans scanning parameters 85
Table 6.1	Summary of the automated LTS scans results 88
Table 6.2	Error in the automated LTS scans results 89
Table 6.3	LTS system speed 96

LIST OF FIGURES		Page
Figure 2.1	Surface profiling system	4
Figure 2.2	Schematic representation of a rough surface	8
Figure 2.3	Surface roughness profile	9
Figure 2.4	Laser strip triangulation	13
Figure 2.5	Triangulation using laser light	13
Figure 2.6	Physical construction of a laser diode module	15
Figure 2.7	Laser line generator	15
Figure 2.8	Standard intensity distribution (Gaussian distribution)	16
Figure 2.9	Uniform intensity distributions	17
Figure 2.10	Relation between fan angle, laser line length and working distance	17
Figure 2.11	Focus pattern of parallel light	18
Figure 2.12	Focal spot size	19
Figure 2.13	Depth of focus of a laser light	19
Figure 2.14	Graphical representation of a typical servo system	22
Figure 2.15	Optical triangulation technique	24
Figure 2.16	Shadow effect is inherent when using optical triangulation	27
Figure 2.17	System for electronic speckle-pattern interferometry (ESPI)	31
Figure 2.18	Schematic diagram of a Nomarski microscope showing detail of two shared images on a sample surface	33
Figure 2.19	X-ray microtopography	34
Figure 3.1	Diagram of the laser triangulation scanning (LTS) system for surface defect inspection	35
Figure 3.2	A photograph of the LTS system	37
Figure 3.3	Fuga15 image sensor	38
Figure 3.4	Frame speed for Fuga15 sensor	39
Figure 3.5	Automated XY translation stage	40
Figure 3.6	Motion system setup	41
Figure 4.1	Automated scanning and 3D surface reconstruction	46
Figure 4.2	LabView GUI of the automated LTS system	47
Figure 4.3	Camera program flow diagram	48
Figure 4.4	Motor moving procedures for the X and Y- axis	50
Figure 4.5	LabView Front Panel of the motor mover program	50

Figure 4.6	Scanning and image capturing paths	51
Figure 4.7	Programming flow diagram of 3D surface reconstruction	52
Figure 4.8	LabView GUI showing an example of a reconstructed 3D surface profile	52
Figure 4.9	Block diagram for automated line scan	54
Figure 4.10	Programming flow for calculate image center from line scan data	54
Figure 4.11	LabView front panel of the laser line scanning	55
Figure 4.12	Front panel of the laser line scanning system showing an example of a 3D surface profile	56
Figure 4.13	Programming block diagram of surface roughness parameters measurement	57
Figure 4.14	LabView front panel of the automated surface roughness parameters measurement showing surface roughness profiles	57
Figure 4.15	LabView GUI for 2D profiles from 3D surface map	58
Figure 4.16	LabView CWGraph3D control properties	58
Figure 5.1	Camera viewing length	60
Figure 5.2	Camera image of a ruler with camera lens and additional 50 mm focal length lens (mm scale)	61
Figure 5.3	Intensity distributions of the laser spot	61
Figure 5.4	Laser spot intensity profile	63
Figure 5.5	System calibration curve with a filter value 160	64
Figure 5.6	Binocular microscopic image of a 3 mm blind hole of the Cu sample surface	67
Figure 5.7	3D surface map of the 3 mm blind hole	68
Figure 5.8	Perspective view from 3D surface map of the 3 mm hole in the YZ plane	68
Figure 5.9	A 2D surface profile from the 3D surface map of the 3 mm hole along the Y-axis	69
Figure 5.10	Perspective view from the 3D surface map of the 3 mm hole in XZ plane	69
Figure 5.11	A 2D surface profile from 3D surface map of the 3 mm hole along the X-axis	70

Figure 5.12	Binocular microscopic image of a 5.9 mm blind hole from the stainless steel sample surface	71
Figure 5.13	3D surface map of the 6 mm blind hole	71
Figure 5.14	Perspective view from 3D surface map of the 5.9 mm stainless steel surface blind hole in XY plane	72
Figure 5.15	A 2D surface profile from the 3D surface of the 5.9 mm stainless steel blind hole along the X-axis	72
Figure 5.16	A 2D surface profile from the 3D surface of the 5.9 mm stainless steel blind hole along the Y-axis	73
Figure 5.17	Binocular microscopic image of a blind hole from the plastic sample surface	74
Figure 5.18	3D surface of the plastic sample blind hole	74
Figure 5.19	XY perspective for the 3D surface map of the plastic sample	75
Figure 5.20	A 2D profile from the 3D surface map along the X-axis	75
Figure 5.21	A 2D profile from the 3D surface map along the Y-axis	76
Figure 5.22	Binocular microscopic image of an 8 mm blind hole from a stainless steel sample	77
Figure 5.23	3D surface map of the 8 mm blind hole	77
Figure 5.24	Binocular microscopic image of a 4 mm blind hole from a copper sample surface	78
Figure 5.25	3D surface map of the 4 mm blind hole	78
Figure 5.26	XY perspective view from 3D surface map of a key surface zero	79
Figure 5.27	Optical microscopic image of a key surface zero	80
Figure 5.28	A 2D profile from the 3D surface map of the key surface zero	80
Figure 5.29	2D surface profile of the 5 mm blind hole from first scans	81
Figure 5.30	2D surface profile of the 5 mm blind hole from second scans	81
Figure 5.31	2D surface profile of the 5 mm blind hole from third scans	81
Figure 5.32	3D surface map of the copper sample surface blind hole	85
Figure 5.33	3D surface map of the stainless steel sample surface blind hole	86
Figure 6.1	(a) Measurement error due to height transition; (b) laser spot image at point A	90
Figure 6.2	Intensity distribution of the image shown in the 6.1 figure (b)	91
Figure 6.3	3D surface map of a sample surface scan from the upper surface to the lower surface	92

Figure 6.4	2D profile of the surface scans from the upper surface to the lower surface	92
Figure 6.5	3D surface map of a sample surface scan from the lower surface to the upper surface	93
Figure 6.6	2D profile of the surface scans from the lower surface to the upper surface	93
Figure 6.7	Effect of beam diameter to detect object size	95
Figure 6.8	Effect of laser beam incident on spot size	95

## GLOSSARY

$R_a$	arithmetic mean roughness
$R_q$	root-mean-square average
$R_y$	maximum height
$R_z$	ten-point mean roughness
$R_p$	highest peak
$R_v$	lowest valley
$R_{sk}$	skewness
$R_{ku}$	kurtosis
LLF	line length factor
DOF	depth of focus
$\theta$	triangulation angle
LTS	laser triangulation system
ADC	analogue to digital converter
DLL	dynamic link library
WOI	window of interest
GUI	graphical user interface
AFM	atomic force microscope
CCD	charge couple device
ESPI	electronic speckle pattern interferometry

# Chapter One

## Introduction

Surface engineering provides an important means of engineering product differentiation in terms of quality, performance and life-cycle cost. Surface inspection is used for quality assurance of surface engineered products. There are many types of inspection methods for surface inspection, generally categorised as destructive and non-destructive inspection (NDT). The main NDT systems for defect inspection include eddy current, liquid penetrant inspection, radiography, ultrasonic, and optical techniques. NDT inspection techniques have great advantages over destructive testing. The demand for greater quality and product reliability has created a need for better techniques of NDT [1]. The optical methods include imaging radar, interferometry, active depth-from-defocus, active stereo, and triangulation. Among them optical triangulation is one of the most popular optical range finding approaches [2].

Over the last few years there has been a significant increase in research into the development and application of optical methods for surface inspection. This has been due to a number of factors such as greater familiarity with laser techniques, the availability of new commercial equipment, and developments in solid-state detector arrays and image processing. There are two types of measurement data acquiring methods: contact measurement and non-contact measurement. Contact measurement is a measuring method that acquires surface geometric information by physically touching the parts, using tactile sensors such as gauges and probes. One example is the co-ordinate measuring machine (CMM). Without physically contacting the part, non-contact measurement is used to acquire surface information by using some sensing devices, such as laser or optical scanners, X-rays or CT scans [3].

Scratches, cracks, wear or checking for proper finish, roughness and texture, are typical tasks of surface quality inspection or surface inspection. Laser scanning inspection systems using the triangulation or stereovision principles are the most common and useful methods for 3D surface profiling [4]. Optical scanning

technologies are generally preferred because of their greater flexibility in the digitization of surfaces, non-contact measurement, sub-micrometer resolution, simple structure and accuracy compared to mechanical systems [5,6]. Four types of light projection patterns are commonly used for 3D profiling include single point, strip, grating and grid [7,8]. Desirable features for on-line profiling systems are:

- a) Non- contact measurement to prevent surfaces from being damaged
- b) High vertical resolution
- c) Immunity to environmental vibration, air disturbance, translation stage error and other error sources and
- d) Easy installation and convenient automated operation [9].

The accurate measurement of surface roughness is very important to ensure the quality of parts and products. A stylus type instrument is commonly used tool for measuring surface roughness parameters. Difficulties for this device in on-line measurements include potential surface scratches, wear of the stylus tip, and danger of instrument damage for high speed and long duration measurements [10]. As an alternative optical techniques have other key advantages including high speed, greater accuracy and reliability [11,12]. Different parameters can be used for the characterization of surface roughness. Statistical parameter such as the arithmetic mean of the roughness,  $R_a$  and the root mean square roughness,  $R_q$ , are most frequently used [13].

In this work an automated laser, based on a previous manual surface scanning system, has been developed. The inspection principle of the optical triangulation provides a non-contact method of determining the displacement of a diffuse surface. Main components of the developed 3D surface-profiling device are a light source, a CMOS camera, and two PC controlled servomotors. Point and a strip pattern of laser light were used as a light sources. The light of a laser diode was focused onto the target surface. A lens imaged this reflected laser light onto the CMOS camera. As the target surface height changes, the image shifts on the CMOS camera due to parallax.

The developed non-contact online surface inspection system allows for quick high-resolution surface scanning and inspection. In the developed inspection system the control of the sample movement, image capturing, and generation of 3D surface

profiles was programmed by LabView and interfaced with a Graphical User Interface (GUI). A separate GUI has been developed for surface roughness parameters measurement.

This thesis is separated into seven chapters and nine appendixes. Chapter two deals with the literature survey for the developed automated surface defect detection system. In the first section of this chapter reviews surface inspection, surface defect, surface roughness, roughness parameters, surface roughness measurement technique and different 3D surface profiling methods. Also reviews the laser as a light source, lasers applications and servo technology.

Chapter three describes the operation principle and experimental setup of this project.

Chapter four presents the software development for the automated surface inspection system. This chapter gives detailed descriptions of the develop software, which include CCAM CCf15 camera interfacing with LabView, automated surface scanning system, and 3D surface reconstruction. This chapter also present that procedure for surface roughness determination.

Chapter five presents experimental results achieved with the system. Surface roughness parameters results are compared with commercial systems including a Pacific Nanotechnology atomic force microscope (AFM) and a stylus instrument Mitutoyo Surftest-402.

Chapter six presents a discussion on the automated LTS system scans results.

Chapter seven presents a conclusions and recommendations for future work.

# Chapter Two

## Literature survey

### 2.1 Surface profile

A profile is the line of intersection of a surface with a sectioning plane which is perpendicular to the surface. It is a two-dimensional slice of the three-dimensional surface. Profiles are almost always measured across the surface in a direction perpendicular to the lay of the surface, as shown in figure 2.1.

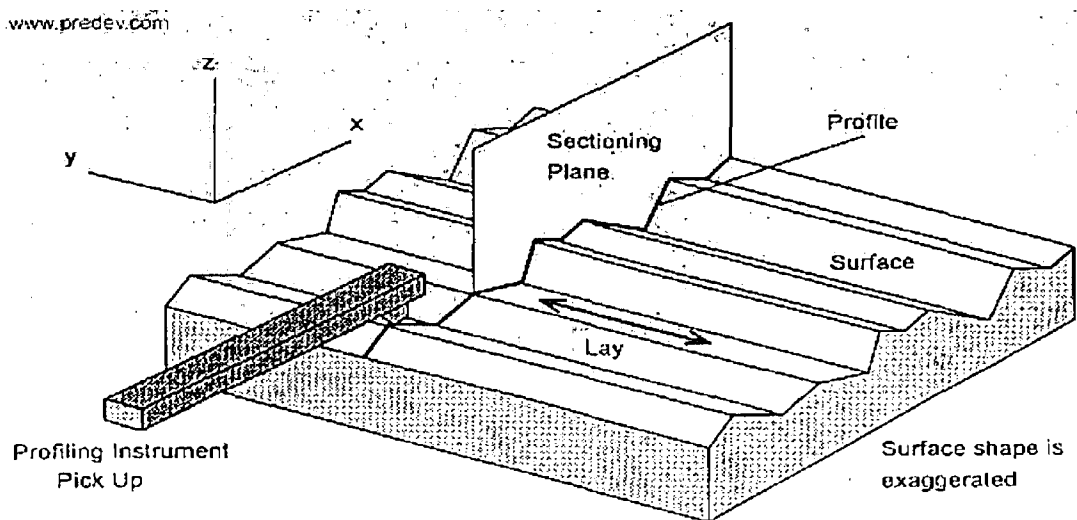


Figure 2.1: Surface profiling system [13].

### 2.2 Roughness profile

Roughness is of significant interest in manufacturing because it is the roughness of a surface that determines its friction in contact with another surface. The roughness of a surface defines how that surfaces feels, how it looks, how it behaves in a contact with another surface, and how it behaves for coating or sealing. For moving parts the roughness determines how the surface will wear, how well it will retain lubricant, and how well it will hold a load.

The roughness profile includes only the shortest wavelength deviations of the measured profile from the nominal profile. The roughness profile is the modified profile obtained by filtering a measured profile to attenuate the longer wavelengths

associated with waviness and form error. Optionally, the roughness may also exclude (by filtering) the very shortest wavelengths of the measured profile, which are considered noise or features smaller than those of interest [13].

### **2.3 Surface inspection**

Surface inspection is usually a bottleneck in many production processes. The visual inspection for appearance of metal components in most manufacturing processes depend mainly on human inspectors whose performance is generally inadequate, subjective and variable. The human visual inspection system is adapted to perform in a world of variety and change. However, the accuracy of the human visual inspection declines with dull, endlessly routine jobs. The inspection is therefore, slow, expensive, erratic, and particularly, subjective. As visual inspection processes only require the analysis of the same type of images repeatedly to detect anomalies, automatic visual inspection is the alternative to the human inspector to objectively conduct such an inspection [14]. Visual surface inspection of plastic, steel, fabric, wood, and other techniques can be easily performed using machine vision. Inspection of products on high speed manufacturing lines can be boring, exhausting, and dangerous for human operators. The manual activity of inspection could be subjective and highly dependent on the experience of human personnel [15]. These reasons lead to humans not always being consistent evaluators of quality. Automated inspection can relieve this work, and provide more consistent quality of inspection untiringly. Furthermore, automated inspection can find defects that are too subtle for detection by an unaided human and can operate at higher speeds than the human eye, for example, products moving several meters per second [16]. Image analysis techniques are being increasingly used to automate industrial inspection.

Lasers are used in inspection and measurement systems because laser light provides a bright, unidirectional, and collimated beam of light with a high degree of temporal (frequency) and spatial coherence. These properties can be useful either singularly or together. For example, when lasers are used in interferometry, the brightness, coherence, and collimation of laser light are all important. However, in the scanning, sorting, and triangulation applications, lasers are used because of brightness, unidirectionality, and collimated qualities of their light; temporal coherence is not a

factor. The various types of laser-based measurement systems have applications in three main areas:

- Dimensional measurement,
- Velocity measurement, and
- Surface inspection.

The use of lasers may be desirable when these applications require high precision, accuracy, or the ability to provide rapid, non-contact gauging of soft, delicate, hot, or moving parts. Photo detectors are generally needed in all the applications, and the light variations can be directly converted into electronic form [17]. Surface inspection with low-power lasers is done either by evaluating the specular or diffuse light reflected from the surface being interrogated. The laser beam used is almost always scanned so that the surfaces involved can be inspected in the shortest period of time. Evaluation of specular reflected laser light to detect surface defects has been highly successful for machine parts where the machined surfaces are specular and surface defects are filled with black residue from the machining process. Evaluation of diffuse laser light to determine differences in the surface finish has been successful in some cases [18].

#### **a. On-line Inspection**

On-line inspection is the acquisition of maintenance data using a computer-based system, revolving around real time data acquisition and processing, giving warning if any of the monitored parameters fall outside pre-configuration levels.

#### **b. Off-line Inspection**

Off-line inspection is the collection of data from a product, which has been removed from the production. Data are collected via a sensor. Sensor and part are moved from point to point as needed. This is obviously different from on line inspection, where the sensor must stay in place to provide instantaneous data acquisition [19].

## **2.4 Surface defects**

In practice the quality determination of component parts often involves the identification and subsequent quantification of characteristic defects that pertain to the particular manufacturing process employed. In consequence it is often possible to associate specific products, materials and manufacturing processes, with particular types of observable surface defect. For example, injection moulded components may tend to exhibit undesired sink or tooling marks, and/or incomplete or additional topological features, whose form, position and orientation, directly relate to both component and tool design. Similarly, cutting, grinding and polishing operations may produce characteristic surface markings, including an altered texture and excessive burrs due to tool wear or the inclusion of foreign abrasive materials. Other characteristic defects include a distinctive wrinkled aspect to sheet metal components, and defective solder joints, which exhibit a predictable abnormal surface appearance and shape. Further examples are the excessive splatter and surface discoloration observed during welding and laser machining, and various surface imperfections on semi-conductor wafers, and in the glaze of ceramic tableware, both of which can result in characteristic observable surface traits [20].

## **2.5 Surface roughness**

The finer irregularities of the surface texture usually result from the inherent action of the production process and material condition [21]. Roughness is a measure of the topographic relief of a surface. Examples, of surface relief include polishing marks on optical surfaces, machining marks on machined surfaces, grains of magnetic material on memory disks, undulations on silicon wafers, or marks left by rollers on sheet stock.

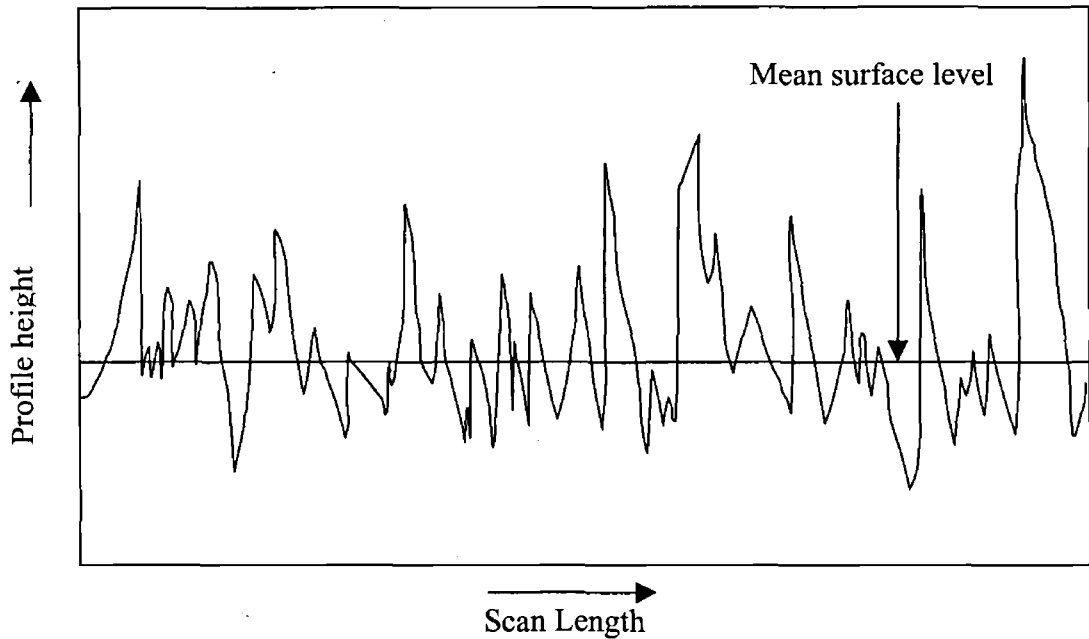


Figure 2.2: Schematic representation of a rough surface [22].

Figure 2.2 shows a schematic representation of a rough surface and some parameters used for describing the surface. Note that the surface height variations are measured from a mean surface level and expressed as a root mean square (RMS) roughness value. The separations between similar surface features along the surface (laterally) are generally referred to as surface spatial wavelengths or statistically as a correlation length. Generally a surface profile is scaled more on the height axis. If both vertical and horizontal scales were the same, the profile would appear as a straight line, and no height detail could be seen [22].

## 2.6 Surface roughness parameters

Surface roughness parameters are used to qualify various conditions of the material surface [23]. Due to the need for different parameters in a wide variety of machining operations, a large number of surface roughness parameters have been developed. They include arithmetic mean roughness ( $R_a$ ), root-mean-square average ( $R_q$ ), maximum height ( $R_y$ ), ten-point mean roughness ( $R_z$ ), highest peak ( $R_p$ ), and lowest valley ( $R_v$ ) [21,23,24,25].

### 2.6.1 Arithmetic mean roughness ( $R_a$ )

The average roughness is by far the most commonly used parameter in surface finish measurement. The average surface roughness, or average deviation, of all points from a plane fit to the test part surface [24]. This parameter is also known as average roughness, AA (arithmetic average), and CLA (center line average).  $R_a$  is universally recognized and is the most used roughness parameter [26]. Therefore,

$$R_a = \frac{1}{L} \int_0^L |Z(x)| dx$$

Where  $R_a$  = the arithmetic average deviation from the mean line.

$L$  = the sampling length

$Z$  = the ordinate of the profile curve.

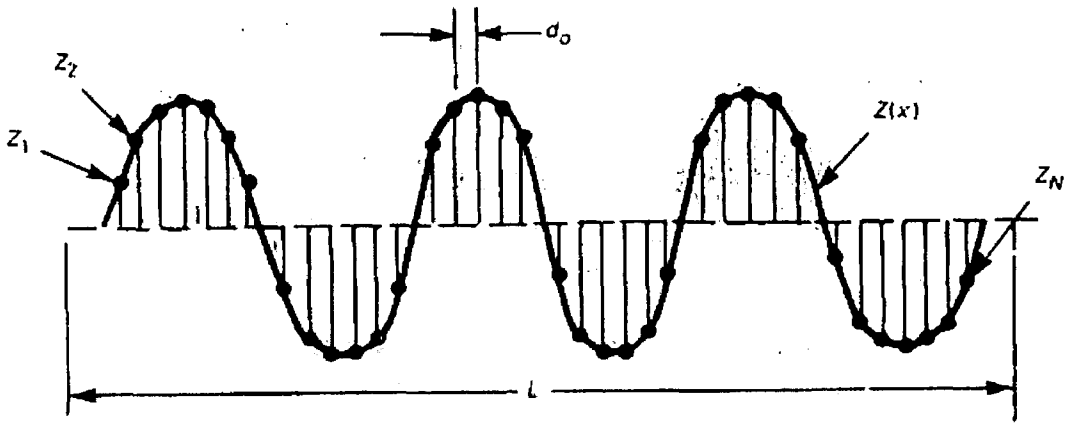


Figure 2.3: Surface roughness profile [21].

For digital instruments approximation of the  $R_a$  value may be obtained by adding the individual  $Z_i$  values without regard to sign and dividing the sum by the number of data points,  $N$ .

$$R_a = (|Z_1| + |Z_2| + |Z_3| + \dots + |Z_N|) / N \quad 2.1$$

As shown in figure 2.3,  $Z(x)$  is the profile height function used to represent the point-by-point deviations between the measured profile and the reference mean line [21]. Distance between two successive points or step size denoted by  $d_0$ .

### 2.6.2 Root-mean-square average ( $R_q$ )

The root-mean-square average of the height deviations measured from the mean linear surface taken within the evolution length or area,  $R_q$  is used in computations of Skew and Kurtosis [24].

In mathematical symbols:

$$R_q = \sqrt{\frac{1}{L} \int_0^L Z(x) dx}$$

The digital approximation  $R_q$  is [21]:

$$R_q = \sqrt{(Z_1^2 + Z_2^2 + Z_3^2 + \dots + Z_N^2) / N} \quad 2.2$$

### 2.6.3 Skewness, Kurtosis and Maximum height

Skewness is a measure of the asymmetry of the profile about the mean line. For digital data the useful formula for skewness is as follows:

$$R_{sk} = \frac{1}{R_q^3} \frac{1}{N} \sum_{j=1}^N Z_j^3 \quad 2.3$$

Kurtosis is a measure of the peakedness of the profile about the mean line [21]. The digital approximation for kurtosis is:

$$R_{ku} = \frac{1}{R_q^4} \frac{1}{N} \sum_{j=1}^N Z_j^4 \quad 2.4$$

Maximum height is the distance between two lines parallel to the mean line that contacts the extreme upper and lower points on the profile within the roughness sampling length [26].

## **2.7 Roughness measurement**

Roughness can be obtained directly from surface-profile measurements, or it can be calculated from a scattering measurement using a theory-relating scattering to surface roughness. Height variations on a surface can be obtained directly from a profile measurement, but one must realize that the instrument is averaging over some area of the surface. Scattering measurements, though easier to make, yield only a statistical average of the surface roughness. [22]. The measurement technique can be divided into two board categories:

- (1) Contact, and
- (2) Non-contact

On the microscopic scale of surface measurements, a contact type stylus profiler (SP) using electronic amplification is the most popular, but the disadvantage here is that it is possible to damage the surface being measured. The probe is also subject to wear after prolonged use, thus affecting the readings. More recently, a non-contact optical profiler based on the two-beam optical interferometry was developed and is now widely used in industry. On a finer scale of surface measurements, two techniques, namely scanning tunnelling microscopy (STM) and atomic force microscopy (AFM) have recently been developed to measure fine details of surface on a molecular scale [28].

Several optical or non-contact methods are applicable to surface-roughness measurement. The most common of these are interferometry, speckle, light scattering, and focus [29,30]. The main advantages of optical methods are that they can be used for measurements, applicable to in-process measurement, and are relatively fast measurement system [31].

## **2.8 Types of scanner for surface profiling**

They are two main types of scanners, which use different methods of scanning:

### **1.Contact**

- Touch probe

### **2.Non-contact**

- a. Laser strip triangulation
- b. Optical triangulation using structured sight

### **2.8.1 Contact scanning - Touch probe**

The object to be scanned is placed anywhere on the machine bed. A probe extends downwards and touched every point on the object to be scanned. This method can be time consuming and scanning may prove difficult for some odd shaped objects.

### **2.8.2 Non-contact scanning**

This enables capturing of surface data in a fraction of the time required by contact probes. With non-contact scanning, chances of inaccuracies or damage occurring to the object you wish to scan are eliminated and it gives precise x, y, and z locations.

Advantages:

- Capable of full profiling and topographical analysis
- Non-contact feature may be advantageous for soft surfaces
- Can generate filtered or unfiltered profiles

Disadvantages:

- Measurements may vary with sample material or reflectivity
- May have difficulty measuring surface features with steep slopes
- Parameters and available filter types may vary with instrument

#### **a. Laser strip triangulation**

A laser diode and strip generator is used to project a laser line onto the object shown in figure 2.4. The line is viewed at an angle by cameras so that height variations in the object can be seen as changes in the shape of the line. The resulting captured image of the strip is a profile that contains the shape of the object.

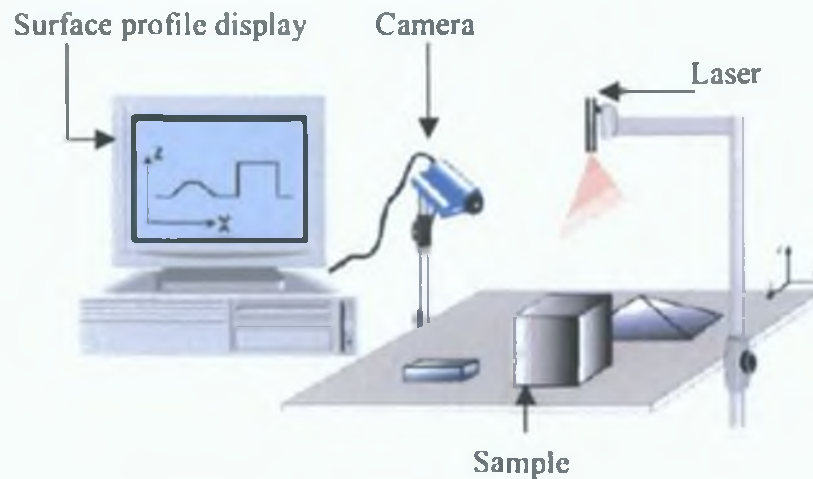


Figure 2.4: Laser strip triangulation [27].

#### b. Optical triangulation using structured light

This type of 3D scanner use a projector and camera pair to scan and capture an object using structured light patterns. The light patterns are horizontal parallel bars called fringes. The scanning process involves the strips being projected onto the object, the light is then reflected off the object into a receiving camera in which it is connected to a frame grabber card as shown in figure 2.5.

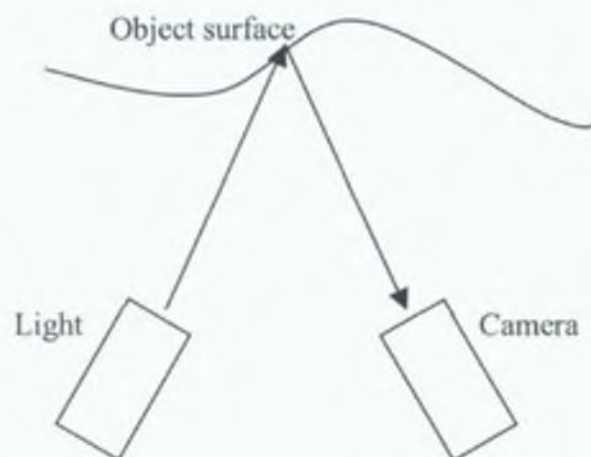


Figure 2.5: Triangulation using laser light.

To process the image, each of the projected lines are tracked and compared with other fringes. This gives the distance information (from the camera to the object) and

thereby the part surface height data,  $z$  data. The lateral surface  $x$  and  $y$  data can be acquired directly from any 2D camera image. After the image is captured, it needs to be processed. During processing, the point clouds go through stages of alignment [32].

## **2.9 Laser technology**

The most important hardware in optical metrology is light source. Laser is an acronym for Light Amplification by Stimulated Emission Radiation. Stimulated emission is the process by which light passing through a fluorescing substance is amplified. With sufficient amplification, a powerful, highly directional beam can be propagated. The laser is a unique source that simultaneously produces both coherent (in-phase) and monochromatic (single-wavelength) radiation. Laser light has propagation characteristics that make possible numerous applications that cannot be achieved with random or collimated sources [33]. A laser is constructed around on an energy pump, which irradiates the laser-active medium and that way, excites particles from the ground into high laying electronic stat, from which they relax by emitting photons. A resonator exerts a selective feedback to the system by restricting the number of allowed eigenfrequencies (modes) that can start oscillating and by coupling the emitted particles. If the total gain per round trip of photons in the resonator exceeds the total loss, then the condition for self-excited oscillation is fulfilled and the laser starts lasing [34].

### **2.9.1 Laser diode module**

Most inspection systems require a continuous wave (CW) laser input whose wavelength is in the visible range. TEM<sub>00</sub> Gaussian mode beams, focused to a high intensity, and to the smallest possible spot are standard requirements for surface inspection. Laser diode modules make cost effective solutions for many laser alignment, measurement, automation, scientific, security, and industrial applications involving batch processing and positioning. Laser diode modules include circuits, a laser diode, and optics packaged in a protective housing as shown in figure 2.6. All that is required for operation is an appropriate external power supply [42].

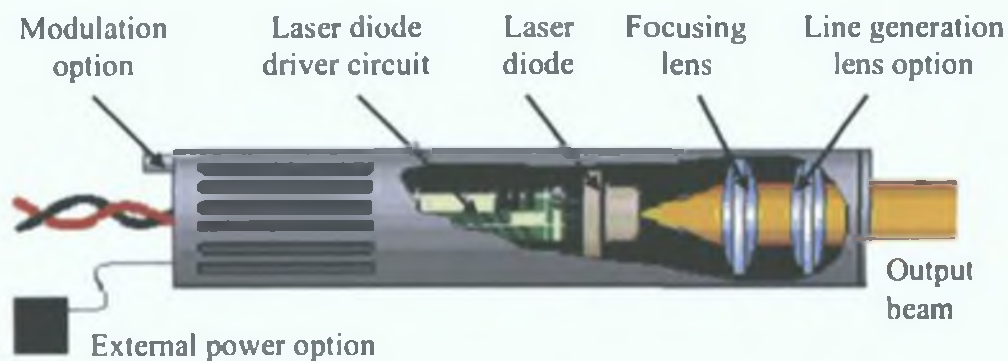


Figure 2.6: Physical construction of a laser diode module [43].

### 2.9.2 Line generators

Line generators are used to project a single straight laser line onto a sample surface. They are available with the option of standard or uniform intensity, as well as virtually any line length. Line generators are often used for machine vision, material inspection, alignment and positioning applications. Standard line generators produce a laser line, which has a Gaussian intensity distribution. This ensures that the line appears bright in the centre and fades off towards the edges. A uniform intensity line has no hotspots, making it the solution of choice for applications requiring easy viewing and receiver calibration, see figure 2.7 [44, 45].

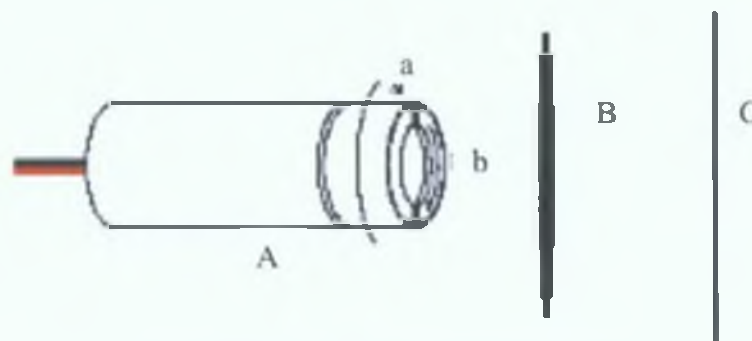


Figure 2.7: Laser line generator [45].

The line generator lens assembly consists of a spherical lens assembly *a* and cylindrical lens assembly *b*. Lens assembly *a* adjusts the thickness of the line or spot and lens assembly *b* ensures a flat line shape. A indicates the laser line generator, B

indicates the laser line generated with lens  $a$  only and C indicates the generate laser line generated with both lens combination.

### 2.9.3 Intensity distribution of laser line

Most laser line generators on the market today use cylindrical optics to generate a line. The Gaussian or non-Gaussian distribution refers to the distribution of power over the projected laser line. The phrase Gaussian distribution (also called Normal Distribution) is a statistical term that refers to a bell-shaped graph. The light intensity of a Gaussian line fades away towards the ends of the line, eventually falling below the threshold level of the detector and becoming invisible to the system. Depending on the settings of the detector and the level of uniformity required by the application, as much as 50% of the available power can be lost. The power intensity is lowest at the tips of the projector laser line, and highest in the middle. Point A and B in figure 2.8 shows the different intensity of the laser line with a Gaussian distribution.

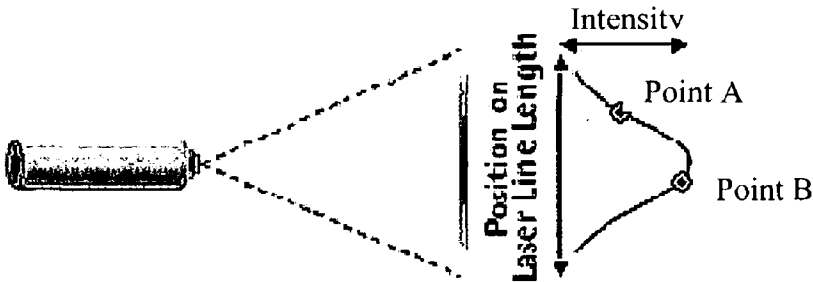


Figure 2.8: Standard intensity distribution (Gaussian distribution) [46].

As the light intensity of Gaussian lines is non-uniform, the calibration of the system can become difficult. Separate calibrations must be made for pixels in the bright central area and for those in the transition area. The low intensity area cannot contribute to the calibration because it is invisible to the system. Figure 2.9 shows the distribution of a standard uniform intensity line generator. Point A and B shows similar intensity. These generators are efficient and easy to calibrate because of their uniform intensity distributions [46].

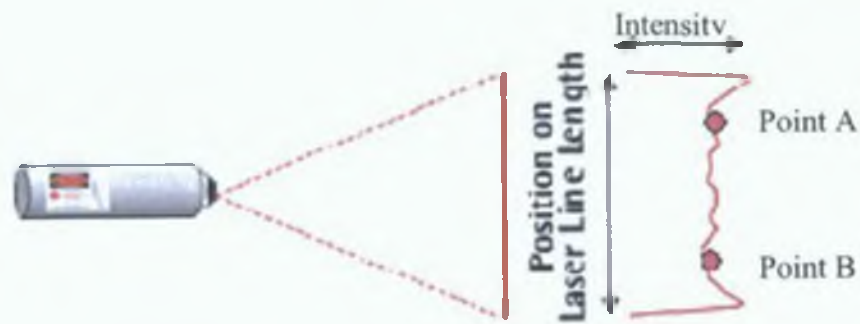


Figure 2.9: Uniform intensity distribution [46].

#### 2.9.4 Laser line length

The fan angle determines the length of the laser line for a set distance as shown in figure 2.10. The line length at a distance,  $D$ , from the laser module is calculated using the line length factor, LLF, as follows:

$$\text{Line length} = D \times \text{LLF}$$

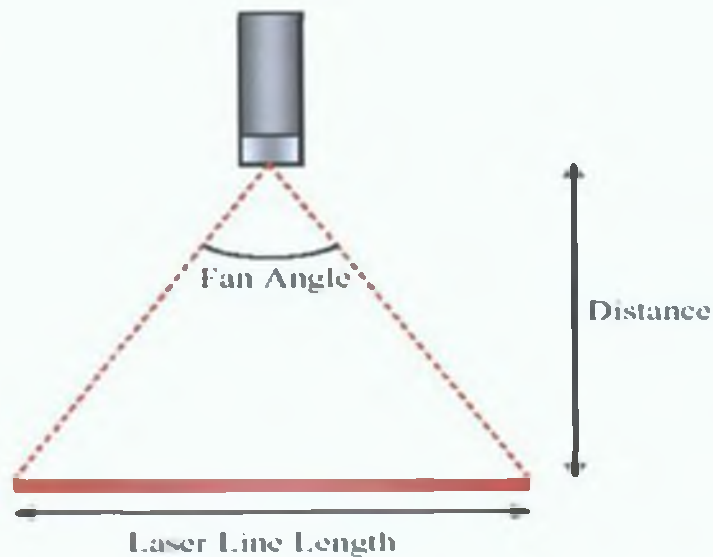


Figure 2.10: Relation between fan angle, laser line length and working distance [44].

#### Line length factors:

30-degree fan angle 0.5359

45-degree fan angle 0.8284

60-degree fan angle 1.1547

90-degree fan angle 2.0000

### 2.9.5 Focal spot size and depth of focus (DOF) of the laser beam

The focusing lens is used to obtain a smaller laser beam spot on the object than at the exit of the laser diode module. Reshaping of the laser beam spot is necessary to get higher resolution from the system. Smaller focal length results in a smaller spot diameter, which may become diffraction limited. The focusing of a laser beam is trade off between beam diameter and depth of field. If the beam diameter were to be smaller, the depth of field would be larger [33].

When a beam of finite diameter,  $D$ , is focused by a lens onto a plane, the individual parts of the beam striking the lens can be imaged to be point radiators of a new wave front. The light rays passing through the lens will converge on the focal plane and interfere with each other, thus constructive and destructive superposition takes place. Light energy is the distributed as shown in figure 2.11. The central maximum contains about 86% of the total power.

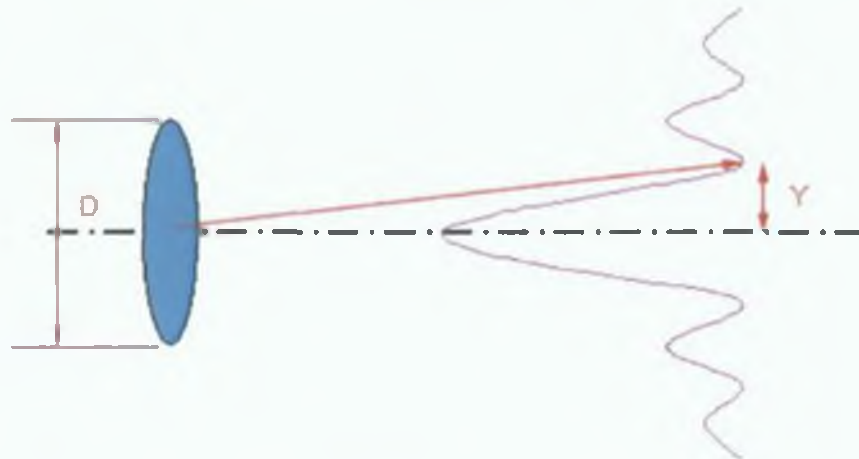


Figure 2.11: Focus pattern of parallel light [40].

Focal spot size determines the maximum energy density that can be achieved when the laser beam power is set, so the focal spot size is very important for inspection systems. If  $2W$  is the incident beam diameter of a laser as shown in figure 2.12 and the beam passes through a lens with a focal length,  $f$ , then focal spot size is calculated by the following equation [41, 47]:

$$D_{\min} = \frac{4 f M^2 \lambda}{\pi D} \quad 2.6$$

Here  $M^2$  is the beam quality factor,  $D_{\min} = 2W_0$  is the minimum focal spot size,  $D = 2W$  is the unfocused beam diameter and  $\lambda$  is the wavelength of the laser beam.

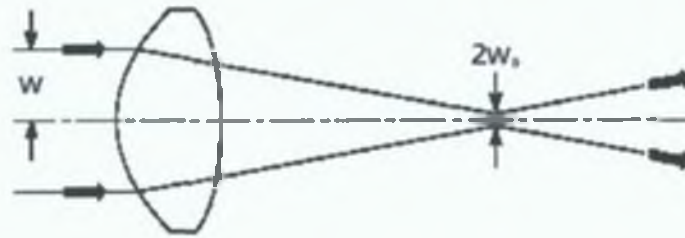


Figure 2.12: Focal spot size [41].

The laser light is first converged at the lens focal plane, and then diverges to wider beam diameter again. The depth of focus is the distance over which the focused beam has about the same intensity. This is defined as the distance over which the focal spot size changes  $-5\%$  to  $5\%$ [40]. Depth of focus (DOF) can also be defined as follows:

$$DOF = 2.44\lambda(f/d)^2 \quad 2.7$$

where  $\lambda$  is the wavelength,  $f$  is the lens focal length,  $d$  is the unfocussed beam diameter as shown in figure 2.13.

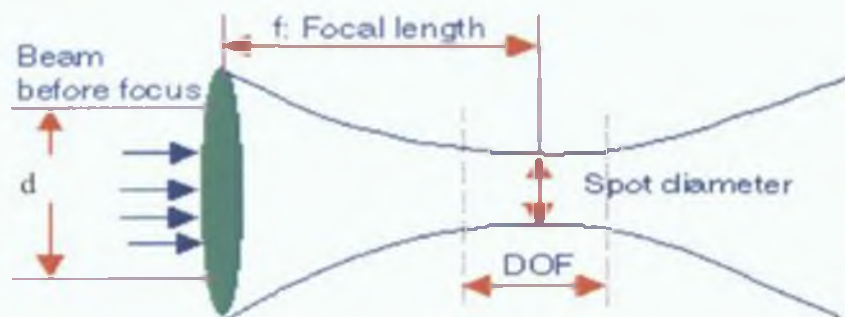


Figure 2.13: Depth of focus of a laser light [40].

### **2.9.6 Laser application**

In the time which has elapsed since Maiman first demonstrated laser action in ruby in 1960, the applications of lasers have multiplied to such an extent that almost all aspects of our daily lives are touched upon, albeit often indirectly, by laser. They are used in many types of industrial processing, engineering, metrology, scientific research, communications, holography, medicine, and for military purpose [35].

#### **a. Low-power application**

Lasers generally in the 1 – 50 mW range fall into this category and are often HeNe or diode lasers. Applications of this type are easy to decide on because invariably there is no other way to do the job. The characteristics of lasers, which make them useful in this type of application, are high monochromaticity (frequency stability), coherence and high radiance (low beam divergence) [36]. The high brightness permits the use of low power lasers for accurate triangulation measurements of absolute distance for both measurements and control of machines such as robots [15]. Low power lasers can be used for less mechanical purposes, for example telecommunications [19].

#### **b. High-power application**

Materials processing applications are more difficult to analyze than most low-power applications. Laser systems also provide powerful deep drilling capability in the aerospace and automotive industries, often at angles and with hole diameters not achievable by conventional, non-laser systems [15]. High power lasers are applied increasingly in various fields of material processing, such as welding, cutting, melting, hardening, and others [19]. There are many competing technologies in welding, heat-treating and material removal. What one has to look for is some unique aspect of the application, which would make good use of one more of the laser's unique capabilities [36].

### **2.9.7 Advantages & disadvantages of laser**

The laser, in its many different forms, is one of the most versatile manufacturing tools. Advantages and disadvantages of laser discuss below.

Advantages:

The advantages of the laser are direct or indirect results of the unique properties of laser light. All such properties are not important in all applications. In fact, in a few cases a unique property may be a disadvantage [36].

The major advantages are:

- High monochromaticity
- High coherence
- Small beam divergence (high radiance)
- Can be focused to small spot
- Easy to direct beam over considerable distances
- Small heat-affected zone (HAZ) in material processing
- Propagates through most gases
- Can be transmitted through transparent materials
- No inertia or force exerted by beam
- Easily adapted to computer control or automated manufacturing system
- Not affected by electromagnetic fields
- Wide range of power levels, mW to tens of kW
- Wide range of pulse energies,  $\mu\text{J}$  to tens of J
- Wide range of pulse repetition rates, pulse lengths and pulse shapes

Disadvantages:

To be cost effective an application must take advantage of unique characteristics of the laser. When these types of applications are identified, the disadvantages often become incidental. Nevertheless, they must be considered in the decision-making process when determining the viability of using a laser for a specific application [36].

The major disadvantages are:

- High capital cost
- Low efficiency
- High technology

- Extra safety consideration
- Operator training

## 2.10 Servo technology

Servo control technology is used in industrial processes to move a specific load in a controlled fashion. Servo drives and amplifiers are used extensively in motion control systems where precise control of position and/or velocity is required. These systems can use either pneumatic, hydraulic, or electromechanical actuation technology. The choice of the actuator type is based on power, speed, precision, and cost requirements. Electromechanical systems are typically used in high precision, low to medium power, and high-speed applications. These systems are flexible, efficient, and cost-effective. Motors are the actuators used in electromechanical systems. Through the interaction of electromagnetic fields, they generate power. These motors provide either rotary or linear motion.

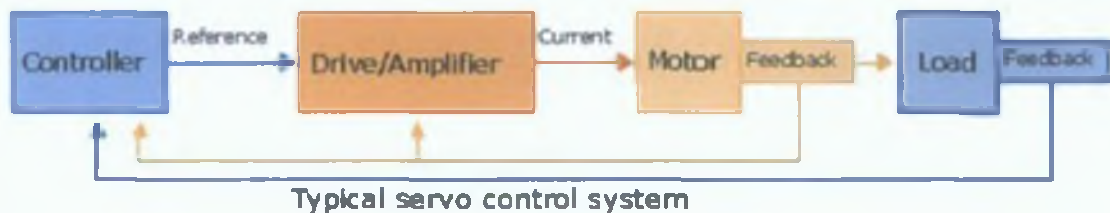


Figure 2.14: Graphical representation of a typical servo system [48].

The type of system shown in figure 2.14 is a feedback system, which is used to control position, velocity, and/or acceleration. The controller contains the algorithms to close the desired loop (typically position or velocity) and also handle machine interfacing with inputs/outputs, terminals, etc. The drive or amplifier closes another loop (typically velocity or current) and represents the electrical power converter that drives the motor according to the controller reference signals. The motor can be of the brushed or brushless type, rotary or linear. The motor is the actual electromagnetic actuator, which generates the forces required to move the load. Feedback elements such as tachometers, LVSTs, encoders and resolvers, are mounted on the motor and/or load in order to close the various servo loops [48].

## **3D data measurement techniques**

### **2.11 Triangulation**

The optical triangulation technique is the simplest method to measure distances between an image acquisition system and the points on target surfaces. The laser diode provides an active light source and the CCD is used to analyze the intensity profile of the reflected laser beam. A target surface is placed at a fixed distance from the video camera. The laser illuminates a spot on the scene and then the camera receives the reflected light and focuses the light on the CCD [6]. Optical triangulation provides a non-contact method of determining the displacement of a diffuse surface. This method has been used in a variety of applications as its speed and accuracy has increased with the development of imaging sensors such as CCD's and lateral effect photodetectors. Due to its simplicity and robustness, optical triangulation has been recognized as the most common method of commercial three-dimensional sensing [33].

#### **2.11.1 Optical triangulation principle**

Basic elements of such a range finding system are: a light source, a scanning mechanism to project the light spot onto the object surface, a collecting lens and a position sensitive photodetector [15]. Figure 2.15 is a simplified diagram of a laser-based system that is successfully used in many industrial applications [18]. A laser beam projects a spot of light onto a diffuse surface of an object and a lens collects part of the light scattered from this surface. If the object is displaced from its original position, the centre of the image spot will also be displaced from its original position. Therefore, the displacement of the object can be determined by measuring the displacement of this spot centre on the position sensor. By using a laser beam to scan the object, the object's shape can be determined with knowledge of the projection angle of this beam and the spot displacement on the position sensor.

In the figure the triangulation device is built with the detector surface perpendicular to the axis of the converging lens. Assuming the surface displacement,  $\Delta$ , to be small

and the angle,  $\theta$ , to be constant as the surface is displaced, the CCD image displacement,  $\delta$ , in relation to  $\Delta$  is

$$\delta = \Delta m \sin \theta \quad 2.8$$

where,  $m = d_i/d_o$  is the magnification factor [18,33].

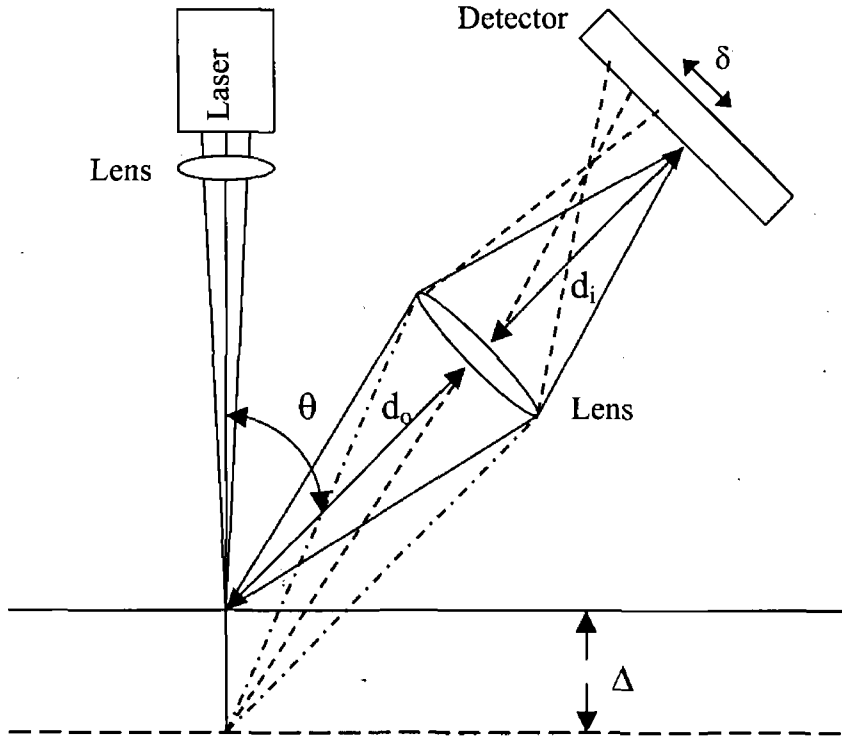


Figure 2.15: Optical triangulation technique [18,33].

Range acquisition literature contains many descriptions of optical triangulation range scanners. The variety of methods differs primarily in the structure of the illuminate (typically point, strip, multi-point, or multi-strip), the dimensionality of the sensor (linear array or CCD grid), and the scanning method (move the object or move the scanner hardware). For optical triangulation systems that extract range data from a single imaged pulse can contain errors due to variations in surface reflectance and spot shape. Several researchers have observed one or both of these accuracy limitations. The images of reflections from rough surfaces are also subject to laser speckle noise, which introduces noise into the range measurement data [15].

### **2.11.2 Error in Triangulation System**

For optical triangulation systems, the accuracy of the range data depends on proper interpretation of imaged light reflections. The most common approach is to reduce the problem to one of finding the “centre” of a one-dimensional spot, where the “centre” refers to the position on the sensor, which hopefully maps to the centre of the illuminate. Typically, researchers have opted for a statistic such as mean, median or peak of the imaged light as representative of the centre. These statistics give the correct answer when the surface is perfectly planar, but they are generally inaccurate to some degree whenever the surface perturbs the shape of the illuminate [2,15].

#### **a. Random Error**

Random error in the laser-scanned data comes from a number of sources and is difficult to control. For triangulation-based laser scanners, the speckle noise caused by the summation of light waves on the CCD is one of the main sources contributing to the random error. The light wave summation often involves random phasors. These phasors may cancel or reinforce each other, leading to dark or bright speckles, respectively. This random process creates uncertainties in the determination of the exact centroid position of the CCD laser image.

#### **b. Systematic Error**

Systematic error in the laser-scanned data is the repeatable component in the digitizing error. It always has the same value under the same scanning conditions. As the systematic error corresponds to the repeatable misinterpretation of the laser images on the CCD photo detector, the three scanning process parameters (scan depth, incident angle, and projected angle) affecting the CCD laser image properties are considered to have primary effects on the systematic error [49].

### **2.11.3 Advantages and Disadvantages of Triangulation System**

The advantages of a triangulation measuring system are speed (data rates up to 10,000 measurements per second are possible) and accuracy (resolution of 2,000:1 to

20,000:1). When such a system is rotated about a central axis, it is possible to measure structures, which are relatively large with reasonable speed and accuracy for most practical purposes [30].

A disadvantage of the use of triangulation systems is that the measurement does not take place coaxial with the light source, leading to problems of shading and in the physical size of the measuring instrument. If the distance between the sensor and the light probe is reduced to minimize these problems then, the non-linearity inherent in the simple triangulation geometry becomes a serious limitation. The light source used has to maintain a high signal to noise ratio at the detector compared to the ambient light reflection in the area of interest, and this can lead to problems of eye safety. Resolution of the triangulation system is limited up to certain extent, so is suitable for bounded situations where it is known that all objects of interest will fall within the range of the measuring equipment. The lens system and laser launching system may present problems in dirty environments with ensuring clear optical path to the target surface [30,33]. The following section represents other control factors for triangulation system

#### **2.11.4 Angle of triangulation and shadow effect**

Usually, we have to make a trade-off between height resolution and shading. Good resolution requires a large triangulation angle. On the other hand, the triangulation angle should be as small as possible in order to avoid shading. The later restriction is a strong motivation to optimise optics, detector and signal evaluation in order to localize the spot image with the highest resolution possible [29]. In laser triangulation, there are two shadow effects as shown in figure 2.16;

- (a) Points on the surface that the projection beam cannot reach; and
- (b) Points on the surface that the sensor cannot detect. Triangulation angle  $\theta_1$  or  $\theta_2$  should be as small as possible in order to avoid these effects [29,33].

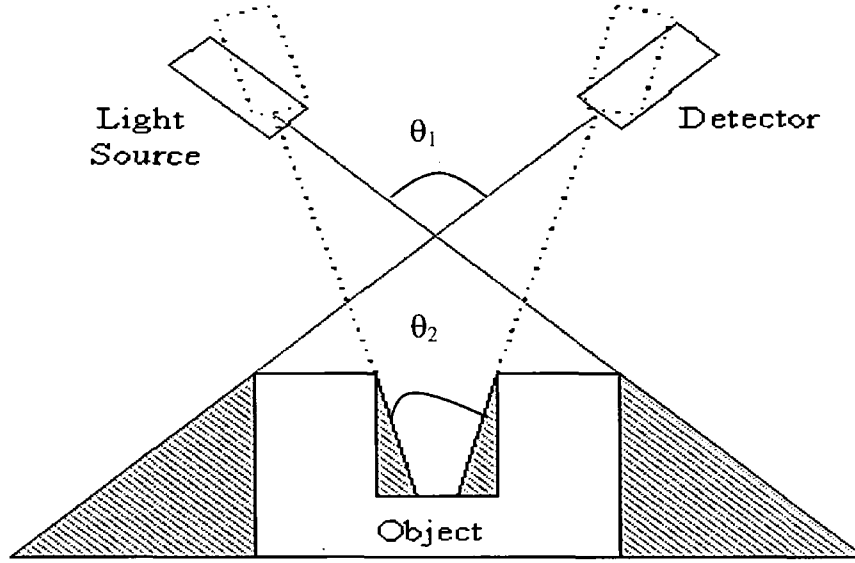


Figure 2.16: Shadow effect is inherent when using optical triangulation [50].

### 2.11.5 Spot size

The projected spot should be small, for two reasons: firstly, to achieve higher lateral resolution on the object. Secondly, the image on the detector should not be too large, to ensure better localization on the detector, i.e., for a better resolution of depth [29].

### 2.11.6 Brightness and contrast

Brightness and contrast are two major factors related the quality of an image. A possible definition of the brightness of an image is its average gray level. For an image with  $M \times N$  pixels, the average gray level can be mathematically expressed as

$$\bar{B} = \frac{1}{MN} \sum_{x=1}^M \sum_{y=1}^N I_{x,y} \quad 2.9$$

where  $I_{x,y}$  represents the intensity of the pixel at coordinate  $(x,y)$ . The contrast in an image can be regarded as the amount of variation of its gray levels. One-way of quantifying this value is to calculate the root-mean-squared difference of the gray level from their mean. Therefore, the contrast also means the standard deviation of the gray levels. As stated in the definition, the contrast can be mathematically expressed as

$$\bar{C} = \sqrt{\frac{1}{MN} \sum_{x=1}^M \sum_{y=1}^N (I_{x,y} - \bar{B})^2} \quad 2.10$$

### 2.11.7 Peak detection algorithm

Theoretically, if we do know the exact forming position of the laser spot in the image, we can compute the distance from the target to the sensor. As mentioned previously, obtaining a good laser beam-profile measurement of even an ideal Gaussian beam is difficult; the task is more difficult with non-Gaussian beams. In general, a commercially available CCD is reported to have signal-to-noise ratio of 40 to 50 dB, which represents the ratio of the RMS noise to the peak signal level. Since peak-to-peak noise is about six times RMS noise, the real signal-to-noise ratio in terms of photocurrent is about 50:1. Therefore, even a pure Gaussian beam has detectable energy at more than twice the beam radius. This noise, particularly in the wings of the beam, can cause significant measurement errors. To increase the reliability of locating the laser spot in the image, using a good algorithm for peak detection is necessary. A good algorithm for peak detection should be insensitive to the variation of noise [51].

### 2.11.8 Image resolution

The resolution of an image is determined by the number of pixels within it and is measured in pixels per mm or dots per mm. The higher the resolution in the image with a fixed image size, the more pixels are to be stored. Most commercially available CCD cameras are equipped with the function of altering the display resolution of the captured image. The setting of the image resolution determines the level of detail recorded by the camera. Higher resolution allows for more detail and subtle color transitions in an image. At the same time, higher resolution means more memory that would be required to store and process an image on computer. On the quality of range finding, however, high resolution does not mean high precision. A higher image resolution might not yield significantly better results without a proper peak detection algorithm; but it is sure to waste a greater computing time. In contrast, a lower resolution image has a less focused look and its outline often appears jagged; but, on the other hand, it might have greater possibilities of increasing the

repeatability of calculations. That is to say, choosing an image resolution is a compromise between capturing all the data you need and reducing the noise you do not want [51].

## **2.12 Interferometry**

Phenomena caused by the interference of light waves can be seen all around us typical examples are the colours of an oil slick or a thin soap film. Only a few colored fringes can be seen with light. As the thickness of the film increases, the optical path difference between the interfering waves increases, and the changes of colour become less noticeable and finally disappear. However, if monochromatic light is used, interference fringes can be seen with quite large optical path differences.

Since the wavelength of visible light is quite small (approximately half a micrometer for green light), optical interferometry permits extremely accurate measurements and has been used as a laboratory technique for almost a hundred years. Several new developments have extended its scope and accuracy and have made the use of optical interferometry practical for a very wide range of measurements.

The most important of these new developments was the invention of the laser. Lasers have removed many of the limitations imposed by conventional sources and have made possible many new interferometric techniques. New applications have also been opened up by the use of single-mode optical fibres to build analogs of conventional interferometers. Yet another development that has revolutionized interferometry has been the increasing use of photo detectors and digital electronics for signal processing.

Some of the current application of optical interferometry are accurate measurements of distances, displacements and vibrations, tests of optical systems, studies of gas flows and plasmas, microscopy, measurements of temperature, pressure, electrical and magnetic fields, rotation sensing, and high resolution spectroscopy. There is little doubt that in the near future many more will be found [52].

### 2.12.1 Speckle interferometry

When the scattered light from a diffuser illuminated by a coherent source such as a laser falls on a screen, a stationary granular pattern results, called a speckle pattern [45]. The image of any object with a rough surface that is illuminated by a laser appears covered with a random granular pattern known as laser speckle. In speckle interferometry the speckled image of an object is made to interfere with a reference field. Any displacement of the surface then results in changes in the intensity distribution in the speckle pattern. Changes in the shape of the object can be studied by superposing two photographs of the object taken in its initial and final states. If the shape of the object has changed, fringes are obtained, corresponding to changes in the degree of correlation of the two speckle patterns. These fringes form a contour map of the surface displacement [52].

Speckle interferometry differs from speckle photography in two main respects. The first is that it involves recording the speckle pattern formed by interference between the speckled image of the object and a uniform reference field or, more commonly, another speckle field. The second is that fringes are obtained due to local changes in the degree of correlation between two such speckle patterns. The sensitivity of the fringes to surface displacements is similar to that obtained with holographic interferometry [53].

Hologram interferometry is based on the use of holograms, which contain more information about the object shape and reflectance than is needed to measure only displacements. These holograms require a recording medium with a high resolving power and this, in practice, means a low sensitivity. Sufficient information for obtaining displacements is contained in the speckle pattern produced by the object and this can be recorded with lower resolving power. As holograms can store waves and reconstruct them later, they introduce a new variable, time, into interferometry. This ability is shared by the speckle techniques.

The two waves in a Michelson interferometer in which one or both mirrors are replaced by a flat diffuser still have the same average phase difference as they had from the mirrors, but on this are superimposed the random phase of the surface roughness. They interfere to produce a speckle pattern that changes if one surface is moved. If the two patterns, before and after the change, are compared, the phase change caused by the movement can be derived. For every  $2N\pi$  change of phase the

speckle returns to its original form so that the correlation pattern of the speckle before and after the change appears as an interferogram that gives contours of changes of  $2N\pi$  [54].

### 2.12.2 Electronic speckle-pattern interferometry (ESPI)

A typical system used to study movement of an object along the line of sight is shown schematically in figure 2.17. The object is imaged by a lens, stopped down to about  $f / 16$ , on a silicon target vidicon on which is also incident a reference beam which diverges from a point located effectively at the centre of the lens aperture. The resulting image interferogram has a coarse speckle structure, which can just be resolved by the camera. The video signal from the camera is electronically processed and signal processed to obtain optimum fringe contrast. This has been studied by Slettemoen, who has also described a modified system, which uses a speckle reference beam [53]. ESPI as it is usually called is now the most widely used method of speckle interferometry. It can observe vibrating surfaces directly to give quantitative results [54].

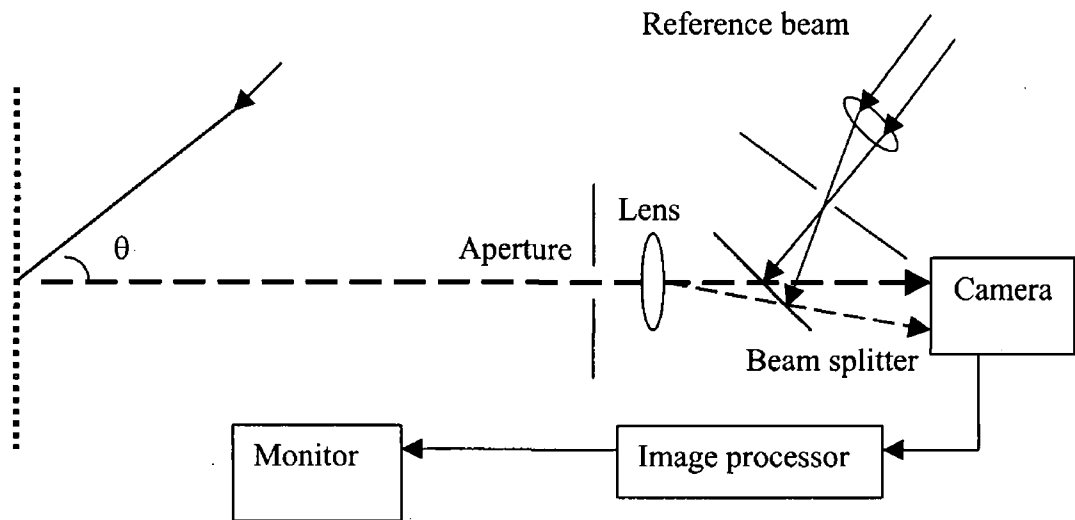


Figure 2.17: System for electronic speckle-pattern interferometry (ESPI) [54].

### **2.12.3 Speckle pattern shearing interferometry**

Speckle pattern interferometry (SPI) is a technique in which a speckle pattern interferes with a reference coherent light wave or with another speckle pattern. Speckle pattern shearing interferometry (SPSI) shows some analogy with SPI, but it uses the interference of two slightly laterally sheared speckle patterns produced by an image-shearing element, and therefore, it is known as a "self-referencing" technique. When measuring, the object to be studied is illuminated by laser light. The speckle pattern produced by the diffusing object surface interferes with a reference light wave or with another speckle pattern on the image plane of an imaging lens, where a Holotest film or a CCD array is positioned, producing a random interference pattern. When the object is deformed, this interference pattern is slightly modified. Superposition or subtraction of the two interference patterns (deformed and undeformed) yields a fringe pattern depicting the surface displacements of the object in SPI and depicting the surface displacement gradients of the object in SPSI [55].

### **2.12.4 Application of interferometry**

Interference occurs when the radiation follows more than one path from its source to the point of detection. It may be described as the local departures of the resultant intensity from the law of addition, for, as the point of detection is moved, the intensity oscillates about the sum of the separate intensities from each path. Light and dark bands are observed, called interference fringes. The phenomenon of interference is a striking illustration of the wave nature of light and it has had a considerable influence on the development of physics. Derived from interference is the technique of interferometry, now one of the important methods of experimental physics, with applications extending into other branch of science [54].

Important application of interferometry [56]:

1. Non-destructive testing
2. Experimental engineering design investigation
3. The quantitative measurement of static surface displacements and strain
4. Experimental vibration analysis
5. Component inspection and quality control
6. Fluid flow visualization

### 2.13 Nomarski microscope

The differential interference contrast (DIC) or Nomarski microscope is a useful instrument for observing surface roughness and other surface defects. The Nomarski microscope emphasizes surface detail by the use of polarized light. Light from the illuminator passes through a polarizer and then through a Wollaston prism, shown in figure 2.18, where it is split into two beams polarized at right angles to each other. The microscope lens focuses this light into two spots on the surface separated by a distance (typically  $\sim 1\mu\text{m}$ ) that depends on the magnification of the objective. Any small defects on the surface will introduce a relative phase difference between the beams. The reflected beams again pass through the microscope objective and the Wollaston prism, interfering in the image plane. Each colour or shade is associated with a specific phase change between the two beams. By using a retarder / polarizer combination the background colour can be cancelled, and the only part of the beam that is visible is that caused by surface defects. Thus, any features that have differences in height or optical constants between them and the rest of the surface will be visible.

Nomarski microscopes are usually used for taking photographs of surfaces; it is also possible to do special data processing of the micrographs to emphasize surface defects and to obtain quantitative information about surface heights and slopes [22].

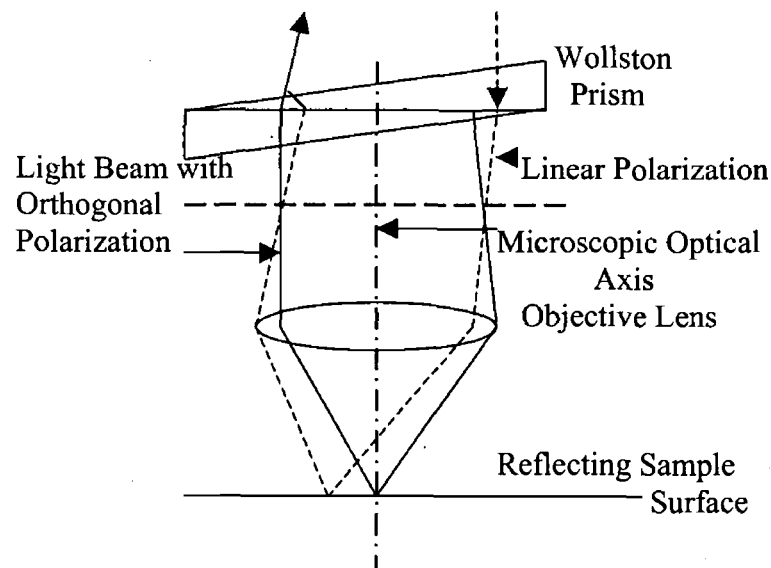


Figure 2.18: Schematic diagram of a Nomarski microscope showing detail of two shared images on a sample surface.

## 2.14 X-ray micro tomography

The 3D X-ray computer tomography is a non-destructive test that generates a stack of images of a testing body (all parallel among each other) as shown in figure 2.19. The computer tomography was initially developed for medical applications but it is being used in other scientific and technological areas nowadays [57].

X-ray microtomography is a 3D radiographic imaging technique. It is similar to conventional X-ray computed tomography systems used in medical and industrial applications. Unlike those systems, which typically have a maximum spatial resolution of about 1 mm, X-ray microtomography is capable of achieving a spatial resolution close to 1  $\mu\text{m}$ . In both conventional tomography and microtomography, hundreds of 2D projection radiographs are taken of a specimen at many different angles. This series of radiographs is mathematically reconstructed to produce a quantitative 3D map of the objects X-ray absorption. Because X-ray absorption is a function of the elemental composition of the object, these X-ray absorption maps can be directly related to the microstructure of the material.

The high resolution of the microtomography system used in this research is the result of using an extremely bright collimated synchrotron X-ray source and a high-resolution scintillator and CCD as the X-ray detector [58].

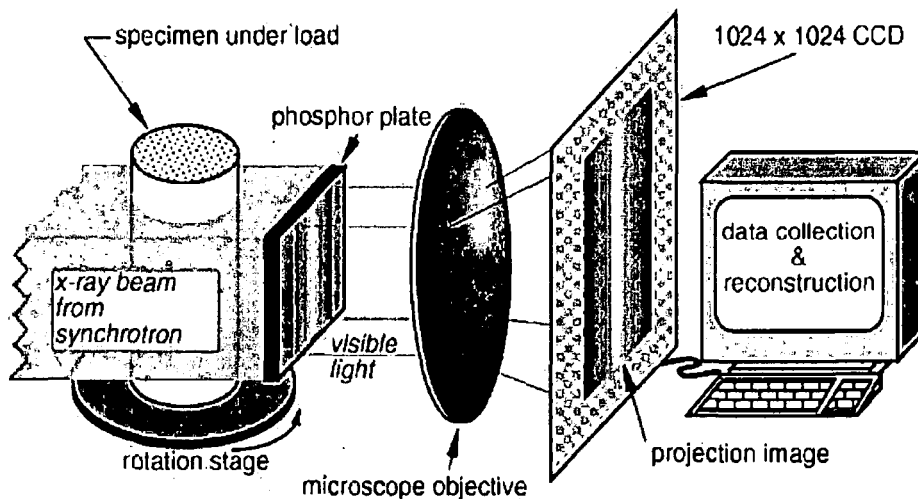


Figure 2.19: X-ray microtomography [58].

# Chapter Three

## Laser Triangulation Scanning System (LTS) Experimental Setup

Detail operation principle of the inspection system would be described in this section. The method is based on the triangulation procedure. The surface being inspected is swept point by point by an oblique light beam, which create a bright spot on it by diffuse reflection [60]. Figure 3.1 illustrates the diagram of automated inspection system and figure 3.2 illustrates the working principle. The theory of the principle of operation was discussed in section 2.11.1 of chapter two and further detailed discussed in Appendix A.

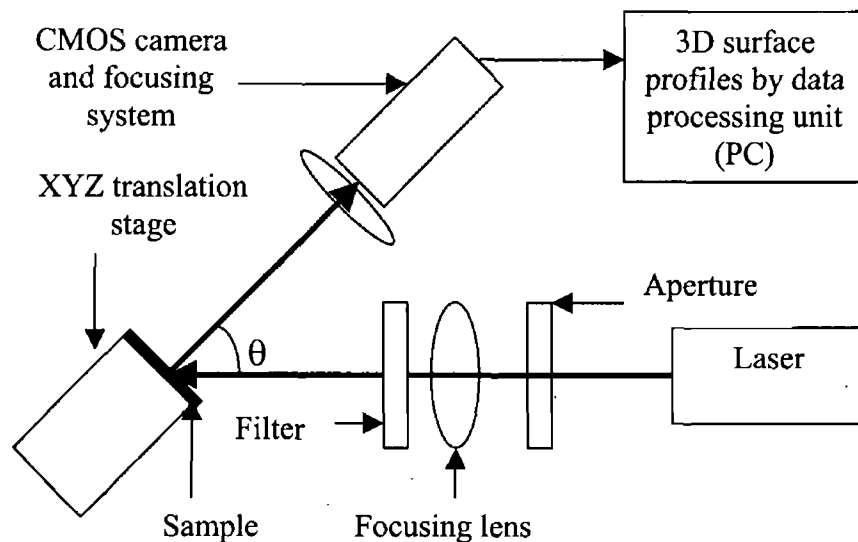


Figure 3.1: Diagram of the laser triangulation scanning (LTS) system for surface defect inspection.

The main components of the developed inspection system were a diode laser, a CCf15 CMOS camera, and two PC controlled servomotors. The light of a laser diode was focused onto a target surface. An image of the laser spot was reflected from the

sample surface onto the CMOS camera. As the target surface height changes, the image spot shifts on the CMOS camera due to the parallax. For spot triangulation the laser diode used was a Thorlabs, CPS186, 4mW output power and 670nm wavelength. The beam shape was a 4.4 mm by 1.2 mm elliptical shape. An aperture was used to generate a 1 mm circular beam from the elliptical laser beam. For line scanning a different laser diode used. This was a Laserex standard laser diode module, LDM-4 series, 650nm wavelength, 25mW output power, glass optics, with 60-degree line generating optic and optimized for 25mm working distance. Two Thorlabs servomotors, Z612B, were used to move the sample in the X and Y directions with a resolution of 0.05  $\mu\text{m}$ . A 100 mm focal length plano-convex lens was used as the focusing lens for the laser beam. The CCf15 CMOS camera was used to capture the signal of the laser beam spot on the sample. An objective lens (L25F1.4) and another plano-convex lens with a focal length 50 mm were used as the imaging lenses for the camera. A photograph of the experimental set up for the automated surface scanning system is shown in figure 3.2.

In the developed inspection system the control of the sample movement, image capturing, and generation of 3D surface profiles was programmed in one LabView program. The developed optical inspection system was also used to calculate surface roughness parameters. Data acquisition, analysis and display program details are presented in software development chapter. The PC used to control this system, acquire the data and analyse the data was a Pentium III model. The PC had a Windows 2000 operating system, 256 MB RAM, 40 GB hard drives and 1000 MHz processor speed. Two PCI cards were installed one to control the camera and one to control the servomotors.

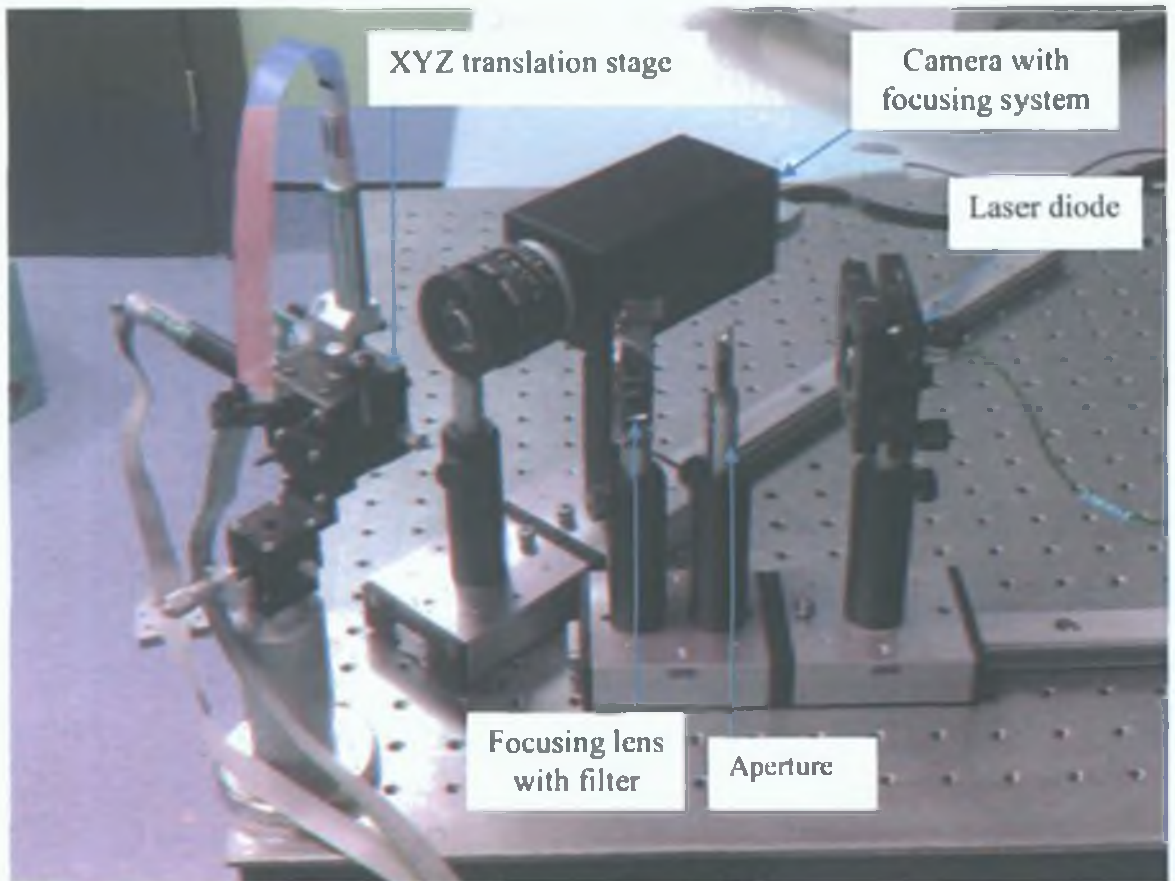


Figure 3.2: A photograph of the LTS system.

### 3.1 Laser diode module

Selecting a laser diode module is dependent on the types of applications for which it is being used. In the developed automated laser spot triangulation system the laser beam spot must be small enough to detect the defects with high precision and for line scanning system laser line thickness must also be thin enough to detect small defects. Properties of laser light are discussed in Appendix B. Specifications of these laser diodes used for the LTS system are shown in table 3.1 and in more detail in Appendix C.

Table 3.1: Specifications of the laser diode modules

Properties	Laser spot generator	Laser line generator
Wavelength	670 nm	650 nm
Beam diameter /Line thickness	4.4mm by 1.2mm	18 micrometer
Operating voltage	- 4.5 to -5.5 V	3 to 6 V
Laser class	3B	3B
Focus distance	Focusable	25 mm

3.2 Image capturing system

A C-Cam CCf15 CMOS camera, with of a Fuga15 image sensor was used in this work and is shown in figure 3.3. The camera was interfaced to the PC via a PCI data acquisition card. The Fuga15 is a random addressable image sensor with some on-chip image processing capabilities. It has 512 x 512 pixels with a logarithmic response, which gives a dynamic range of more than 120 dB. This allowed the sensor to see very bright and very dark parts in the same image. It has an on-chip flash 8-bit analogue to digital converter and automatic illumination control and an analogue output, see table 3.2 for summary specifications and Appendix D for further details.

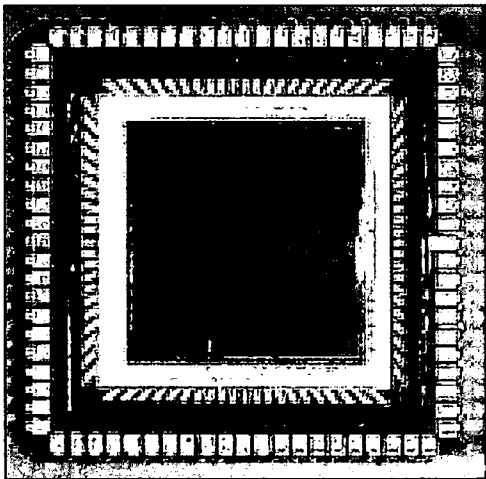


Figure 3.3: Fuga15 image sensor [64].

Table 3.2: Technical specifications of Fuga15 sensor

Active pixels	512 x 512 randomly addressable
Pixel pitch	12.5 x 12.5 $\mu\text{m}^2$ (2032 dots per inch horizontally and vertically)
Optical active area	6.4 x 6.4 $\text{mm}^2$ (0.252 x 0.252 sq. inch)
ADC	On chip 8 bit flash ADC
Color	Black & White
Supply voltage	5V

The Fuga15 camera has some limitations in speed. Full frame images can be read out at 10 and 15 images a second. In extreme dark conditions, only about 8 images a second are possible. The limitations are at a PC and interface level. Due to the random access and possibility of sub-sampling, it is possible to readout the camera at higher frame rates. Typical industrial applications can access more than 1000 frames per second if the window of interest is limited [64], is shown figure 3.4. A table of maximum frame rate capabilities for the current system with different WOI is shown in Appendix D.

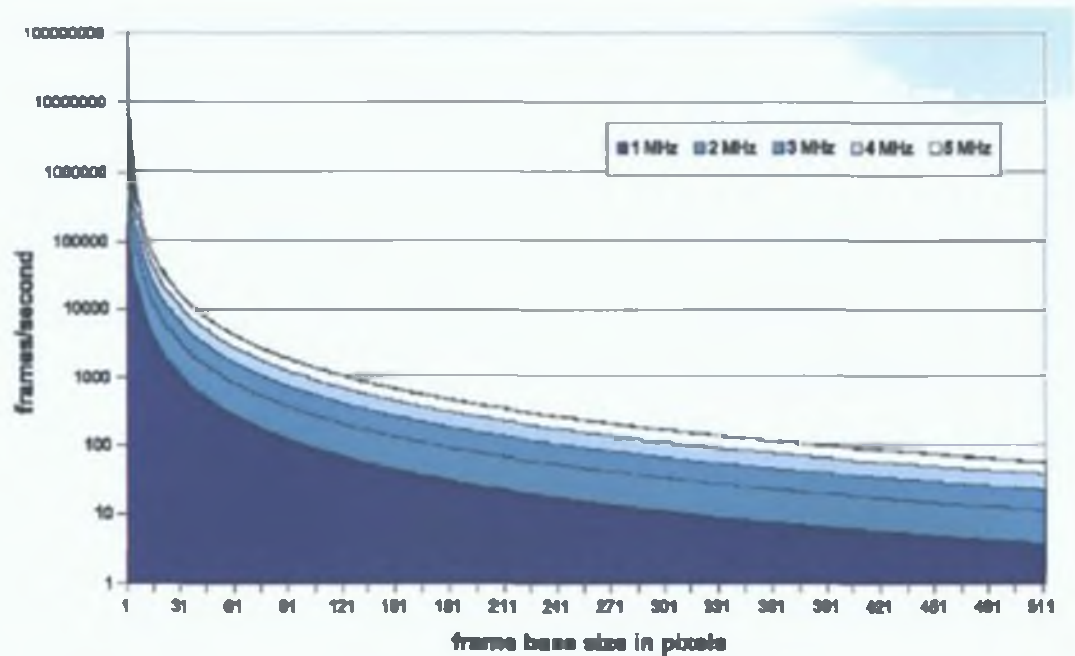


Figure 3.4 Frame speed for Fuga15 sensor [64].

### 3.3 Motorised translation stages

Automated translation stage consists of two Thorlabs servomotors, Z612B. These were used to move the sample in the X and Y directions with a resolution of  $0.05\text{ }\mu\text{m}$ . The traveling range speed of the servomotors is  $50\text{--}425\text{ }\mu\text{m/s}$  with a traveling range of 12 mm. Figure 3.5 shows the automated XY translation stage. The servomotors were interface with the PC via two MC110 motion control modules and a DCX-PCI100 motion control motherboard. Further specification details of these components are given in Appendix E. The automated XY translation stage was mounted on a manual micrometer was used to set the sample surface to sensor distance (i.e. the Z displacement). This micrometer was adjustable to  $10\text{ }\mu\text{m}$  gauge marking.

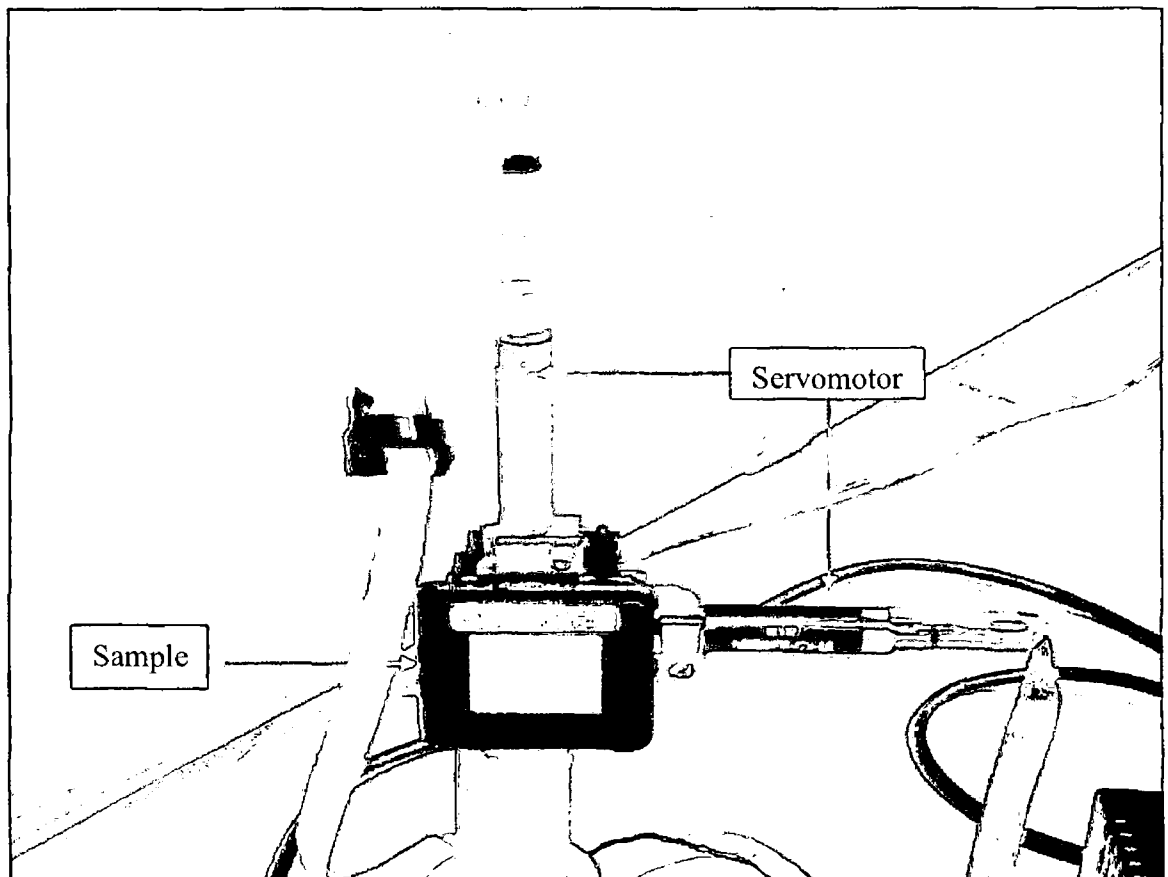


Figure 3.5: Automated XY translation stage.

### 3.3.1 Motion Integrator

Motion Integrator is a suite of powerful Windows tools, shown in figure 3.6 that are used to:

- Configure the DCX motion control system
- Verify the operation of the control system
- Execute and plot the results of single and/or multi-axes moves
- Connect and test I/O

Axis I/O (Home, Limits, Enable)

General purpose Digital I/O

General purpose Analog I/O

- Tune the servo axes
- Diagnose controller failures

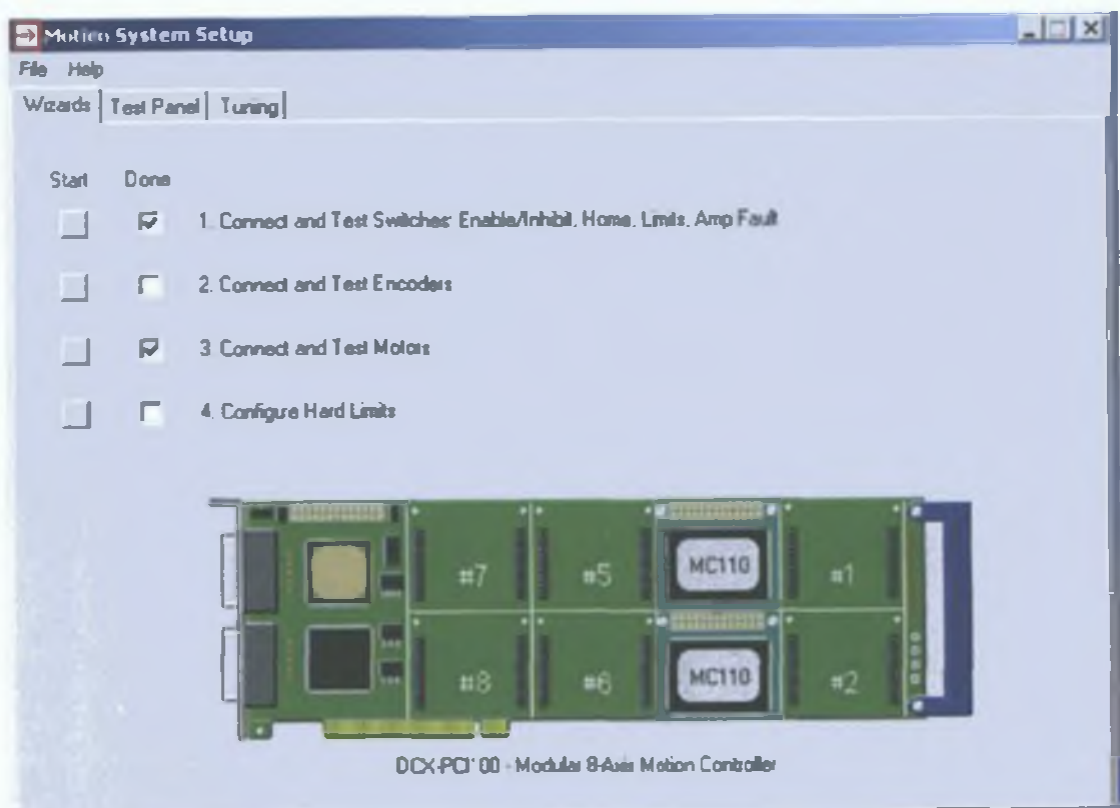


Figure 3.6: Motion system setup.

### **3.3.2 Tuning servo's with Motion Integrator**

Motion Integrator provides a powerful and easy to use tool for 'dialing in' the performance of servo systems. From simple current/torque mode amplifiers to sophisticated Digital Drives, Motion Integrator makes tuning a servo is quick and easy. By disabling the Trajectory generator, the user can execute repeated Gain mode (no ramping - maximum velocity or acceleration/deceleration) step responses to determine the optimal PID filter parameters:

- Proportional gain
- Derivative gain
- Derivative sampling period
- Integral gain
- Integration Limit

With the Trajectory generator turned on, the user can execute 'real world' moves displaying the calculated position, actual position, and following error plots.

The basic steps required to implement closed loop servo motion are:

1. Proper encoder operation
2. Setting the allowable following error
3. Verify proper motor/encoder phasing
4. Tuning the servo (PID)

### **3.3.3 Quadrature incremental encoder**

All closed loop servo systems require position or velocity feedback. These feedback devices output signals that relay position and/or velocity with which motion controller 'closes the loop'. The most common feedback device used with intelligent motion control systems is quadrature incremental encoder.

### **3.3.4 Setting the Allowable Following Error**

Following error is the difference between where an axis 'is' and where the controller has 'calculated it should be'. When a servo axis is turned on, if a position error exists, the PID algorithm will cause a command voltage to be applied to the servo to

correct the error. While an axis is executing a move, the following error will typically be between 20 and 100 encoder counts. Very high performance systems can be 'tightly tuned' to maintain a following error within 5 to 10 encoder counts. Systems with low-resolution encoders and/or high inertial loads will typically maintain a following error between 150 and 500 encoder counts during a move.

The three conditions that will typically cause a following error fault are:

- 1) Improper servo tuning (Proportional gain too low)
- 2) Velocity profile that the system cannot execute (moving too fast)
- 3) The axis is reversed phased (move positive causes encoder position to begin decrementing)

### **3.3.5 Servo tuning procedure**

A servo motor motion system is a closed loop system with negative feedback. Servo tuning is the process of adjusting the gains (proportional, derivative, and integral) of this axis controller to get the best possible performance from the system. A servomotor and its load both have inertia, which the servo amplifier must accelerate and decelerate while attempting to follow a change in the input (from the motion controller). The presence of inertia will tend to result in over-correction, with the system oscillating or "ringing" beyond either side of its target (under-damped response). This ringing must be damped, but too much damping will cause the response to be sluggish (over-damped response). Proper balancing will result in an ideal or critically damped system. The servo system is tuned by applying a command output or 'step response', plotting the resulting motion, then adjusting parameters of the digital PID filter until an acceptable system response is achieved. A step response is an output command by the motion controller to a specific position [65]. A typical step response distance used for tuning a servo is 100 encoder counts. Following Motion and PID values was used in the LTS system:

Acceleration = 10000 counts per second per second

Max. Velocity = 9000 counts per second

Proportional Gain = 1000 counts

Integral Gain = 500 counts

Integration Limit = 50 counts

Derivative Gain = 500 counts

Derivative Sampling = 0.005115 counts

Following Error = 32000 counts

Procedure for tuning the servomotors used in this work is presented in detail in Appendix F.

# Chapter Four

## Software development

The main intention of the software development was to develop an automated surface inspection system for laser spot and laser line scanning. In this chapter a detailed description of the software design is outlined. The following graphical user interfaces (GUI) have been developed in LabView, version 7.0

- a) Automated laser scanning system for laser spot triangulation,
- b) Automated laser line scanning system, and
- c) Surface roughness parameters measurement

For an automated inspection system, images capture by the camera, stage movement system and 3D surface reconstruction should be in same GUI. Camera interfacing with LabView was a very important part of this work because the CCAM camera interface was not previously available in the LabView program. A LabView Call Library Function was used for interfacing the camera with LabView. General configuration of the Call Library Function is presented in Appendix G.

### 4.1 Software development for automated surface scanning

These three main sections in the automated scanning GUI program:

- 1. Set scanning parameters,
- 2. Control sample movement and image capture, and
- 3. 3D reconstruction

A flow chart depicting the programmes developed for automated scanning and 3D surface reconstruction in LabView is shown in figure 4.1. WOI, brightness and delays are camera functions. A more detailed procedure of camera operation in LabView is discussed in the next section of this chapter. After setting X-Start, X-End, Y-Start, Y-End, delays, scan length of X and Y direction, and step size the interface ready to surface scan. In order to carry out the scanning of a sample surface, initially the sample part was mounted on the automated translation stage. The particular area on the plate to be scanned was positioned carefully so that the laser beam was incident at the starting position of the area. Scanning initiates by incrementing the X-axis

motor while keeping the Y- axis motor and Z-axis position constant. Every time the X-axis was displaced, the LabView GUI recorded 1D array of image data of the surface. Once the displacements along X-axis were finished, then the Y-axis motor was incremented by the specified step size and the next X-axis scan started in the reverse direction. After completing the define number of steps in both X and Y direction, the 3D surface was reconstructed from the image data.

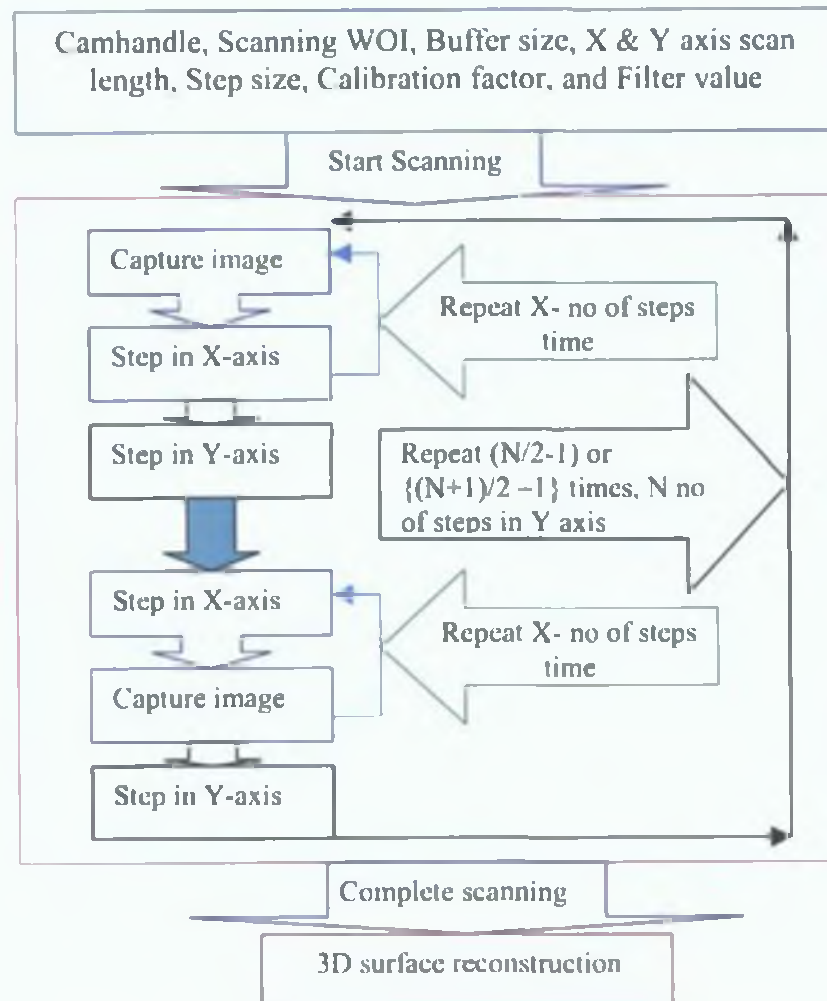


Figure 4.1: Automated scanning and 3D surface reconstruction.

In order to scan a sample surface by the developed system user has to set scanning WOI, scan length for both X and Y axis (mm), step size ( $\mu\text{m}$ ), filter value to remove unwanted information from the image and depth calibration factor ( $\mu\text{m}/\text{pixel}$ ) in input tabs of the LabView GUI, the LabView front panel of the automated LTS system is shown in figure 4.2. Outputs and errors are shown in another tabs on the

right hand side of this LabView GUI. Another tab control was used to display the capture image and the reconstructed 3D surface map.

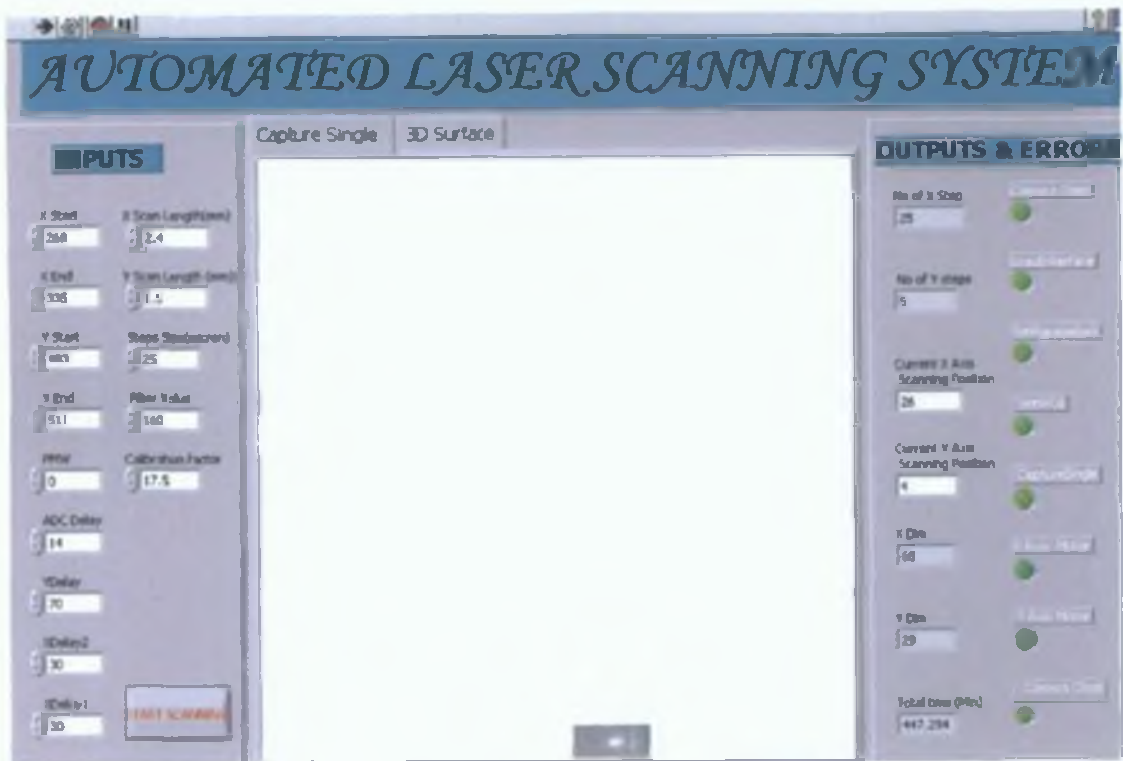


Figure 4.2: LabView GUI of the automated LTS system.

#### 4.1.1 Camera interfacing in LabView

This section explains the way to run a CCf15 camera by the LabView program developed. The Call Library Function node was used for interfacing between CCf15 camera and LabView program. A CAMERA.VI LabView interface was developed the camera through LabView using the already available CAPI.DLL Dynamic Link Library. CCAPI.H header file (Appendix H) and the CCf15.TTB logic file. The Dynamic Link Library (DLL) file is the link between the executable program and the camera driver. CCf15.TTB is the logic for the interface and the camera. A flow chart depicting the programmes developed for camera interface in LabView is shown in figure 4.3.

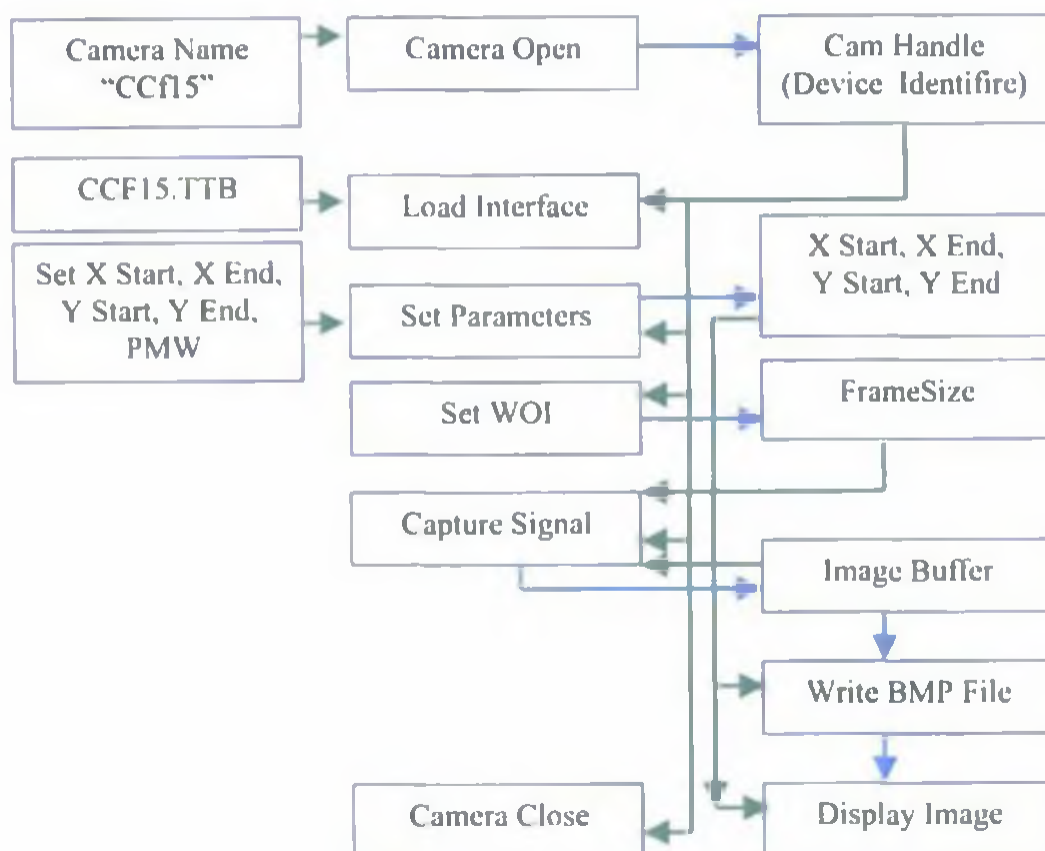


Figure 4.3: Camera programming flow diagram.

In order to make the program modular, every function call of the camera was placed in a subprogram (subVI). LabView front panel of the CAMERA.vi, front panel and block diagram of all subVI's are shown in Appendix I

As a first step, the program loads the CC\_Open function which open's the camera with the specific name and assigns specific minimum and maximum parameters to the 'camhandle'. Camhandle is generated on the basis of camera name, which for CCf15 camera should be "CCf15" input string in the block diagram. The other functions from CCAP1.DLL can be called after this function and use the camhandle as device identifier.

In the next step, the CCf15.TTB logic is send to the interface and the camera. This is done with the functions CC\_LoadInterface from the DLL. This operation should be performed whenever a power-down occurred because the camera looses its internal logic. If this function returns a non-zero value the interface should be ready for use.

Set Camera Parameter.vi allows the camera parameters to be set by the user. The user can set any size of window of interest (WOI) and brightness value (PMW). For setting WOI, the user has to set X-start, X-end, Y-start, and Y-end values. As the Fuga15 sensor has 512 x 512 pixels, the X and Y-values must be between 0 and 511. Another thing that must be taken into consideration the X-axis dimension of the set WOI must be multiple of 4. If the X-axis dimension is not a multiple of 4, the image will be displayed in an italic shape. The user must also ensure that the coordinates are given in the correct order (the end pixel value should be greater than the start pixel value). The following output come from this subVI: X-start, X-end, Y-start, and Y-end values set in front panel by the user. These values go through CC\_SetWOI function as inputs to produce the frame size. The camera is then ready to capture singles.

CC\_CaptureSignal function is used for capturing the camera signal. By calling this function an image is captured with the preset parameters and placed into a buffer. All the other DLL functions do not need to be repeated when no change in acquisition parameters or WOI is to be made. For an 8-bit black & white image, the serial buffer can be defined as: array [0.....262114] of byte.

Now we have the image in the buffer, we can display it on the screen and automatically write it as bit map file (BMP) by using WriteBMP.vi. A picture control object was used to displaying image on the computer screen.

At the end of image capture we need to close the device. CC\_Close function must be called before the windows application ends.

#### 4.1.2 Control sample movement and data processing procedure

Camhandle and buffer size or frame size are required for capture an image during scanning and all the other API functions do not need to be repeated because of no changes in acquisition parameters or a fixed WOI size set for scanning. Figure 4.4 shows the motor moving system algorithm and the LabView front panel of motor mover program is shown in figure 4.5.

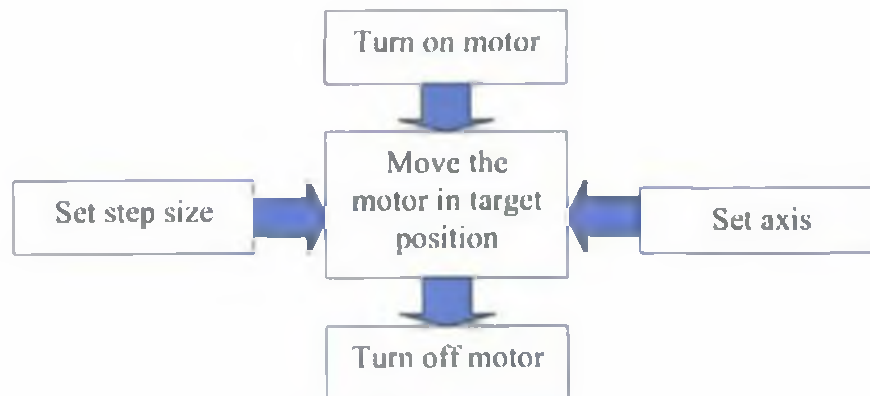


Figure 4.4: Motor moving procedures for the X and Y- axis.

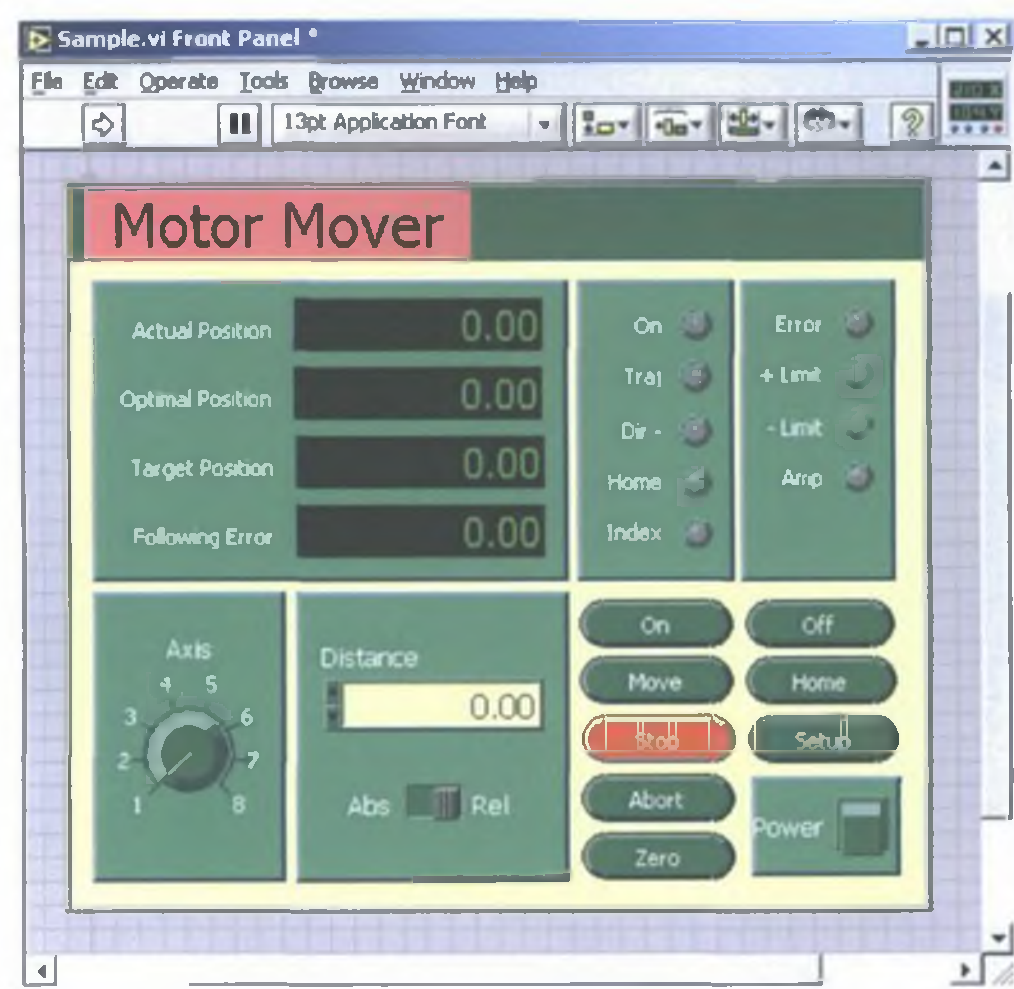


Figure 4.5: LabView Front Panel of the motor mover program.

A raster scanning pattern was used in this work. Scanning started from 0 and finish at  $(n - 1)$ , where  $n$  was the number of steps in the X-axis shown is in figure 4.6. After

completing one line scan in the X-axis, the Y-axis was moved by a define step size. Scanning then recommences in the reverse direction in the X-axis. During scanning in the backward direction the first position of the scan surface was  $(n - 1)$  and the finish was at 0. The program however saved this data in the reverse order (from 0 to  $(n-1)$ ),

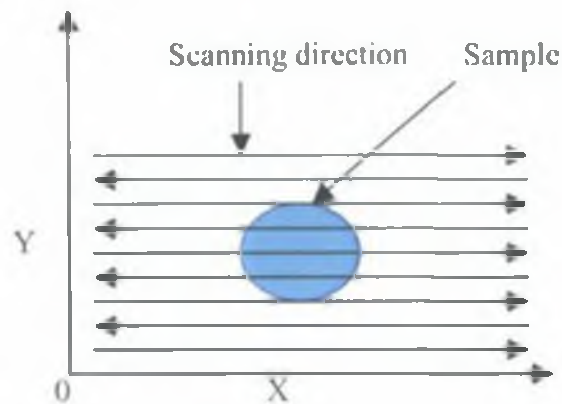


Figure 4.6: Scanning and image capturing paths.

#### 4.1.3 3D surface reconstruction

*3D parametric surface* LabView block diagram object was used for 3D surface reconstruction. X, Y and Z matrices are the input for this function. To calculate the image centre from the data was reorganised according to the scanning WOI (Y dimension and X dimension respectively the number of rows and columns for the 2D array). Programming flow for the 3D surface reconstruction algorithm is shown in figure 4.7. The beam shift was calculated for every increment in scanning direction in terms of number pixel. Multiplying by the calibration factor ( $\mu\text{m}/\text{pixel}$ ) the actual displacement in the depth direction for every step in scanning direction was calculated. X and Y-axis were known from the user input step size. Figure 4.8 shows an example of a 3D surface profile generated the Lab View GUI.

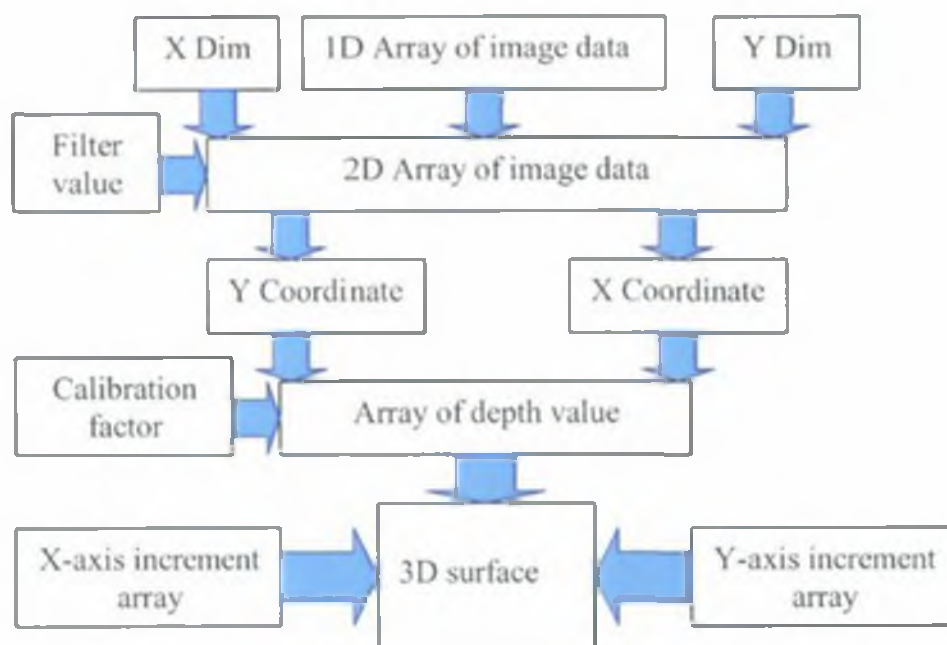


Figure 4.7: Programming flow diagram of 3D surface reconstruction.

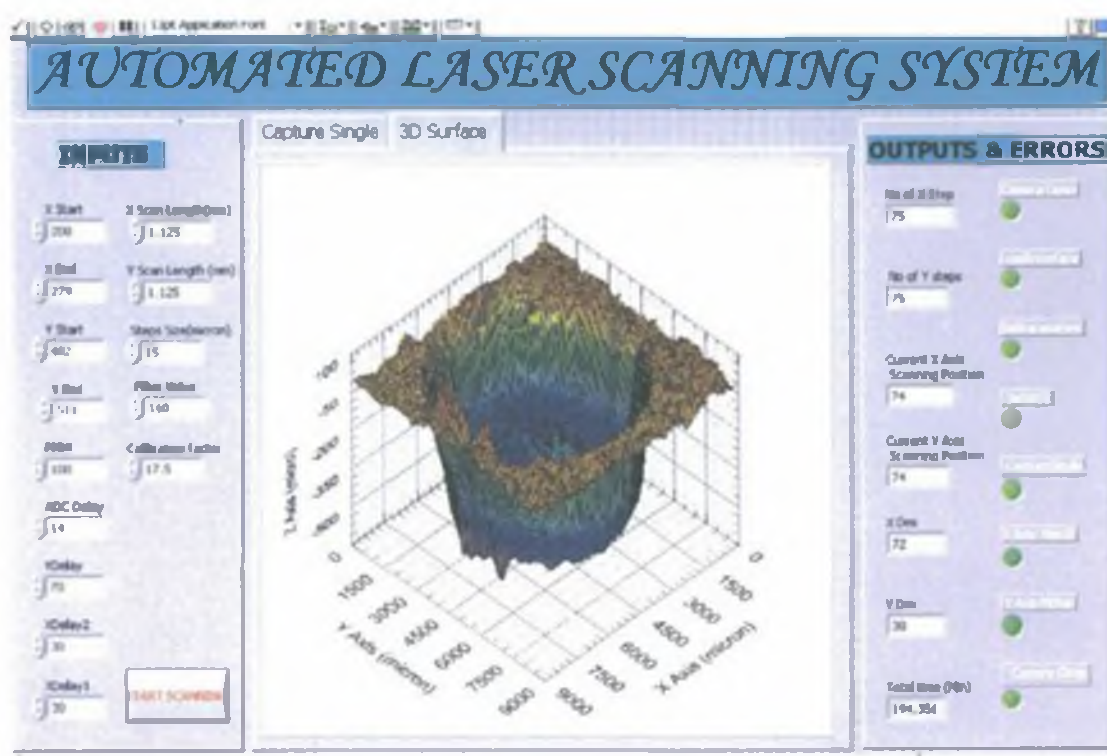


Figure 4.8: LabView GUI showing an example of a reconstructed 3D surface profile.

## 4.2 Software development for laser line scanning system

Figure 4.9 shows the program block diagram of automated laser line scanning system. WOI, brightness and delays are camera function. Detail procedure of camera operation in LabView already discuss in section 4.1.1. In order to scan a sample surface by the developed system the user has input the following variables in LabView GUI: scanning WOI, X-axis scan length (mm), X-axis step size ( $\mu\text{m}$ ), number of pixels for Y-axis step size, filter value to remove unwanted information from the image, depth calibration factor ( $\mu\text{m}/\text{pixel}$ ) and X-Y magnification calibration factor ( $\mu\text{m}/\text{pixel}$ ). For scanning of a sample surface, initially the sample part was mounted on the automated translation stage. The particular area on the plate to be scanned was positioned carefully so that the laser beam was incident at the starting position of the area. Scanning initiates by incrementing the X-axis motor while keeping the Y and Z-axis position constant. Every time the X-axis was displaced, the image was captured as a 1D array. Captured 1D array from the camera WOI was converted into 2D array. This array was then sectioned into array subset according to the selected Y step size. The programming block diagram for the image center calculation is shown in figure 4.10. Detail of the 3D surface reconstruction procedure was presented in the previous section of this chapter. Figure 4.11 and 4.12 respectively show the GUI for line scanning system and an example of reconstructed 3D surface by the laser line scanning.

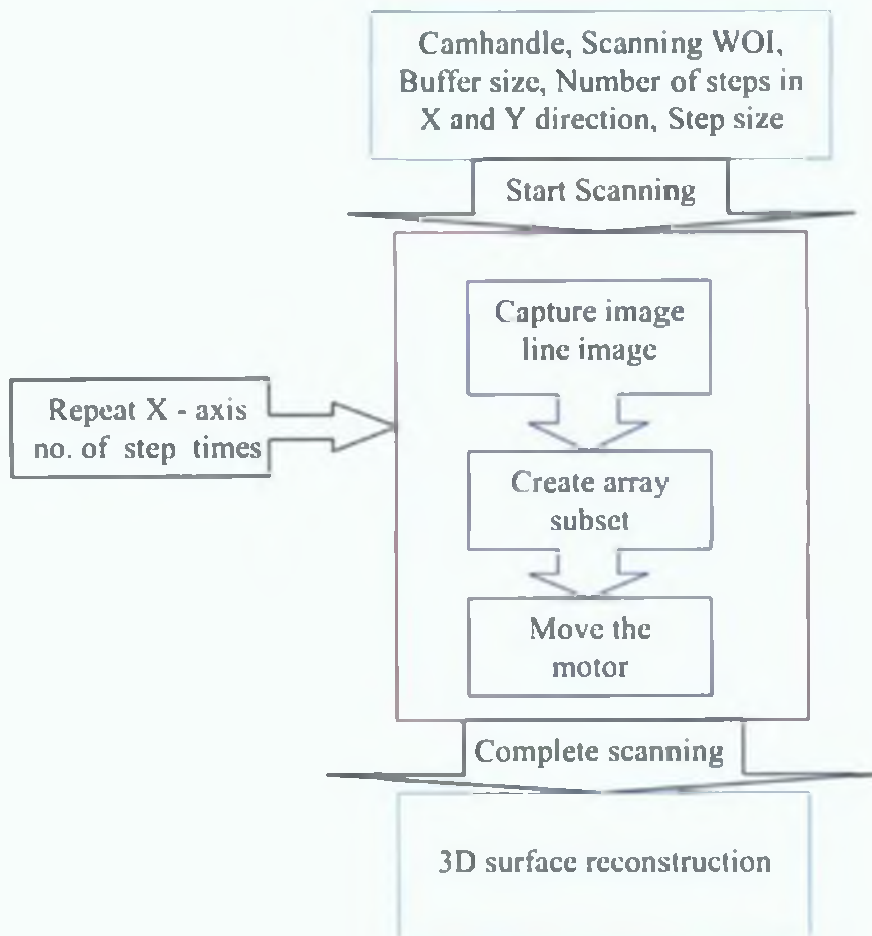


Figure 4.9: Block diagram for automated line scan.

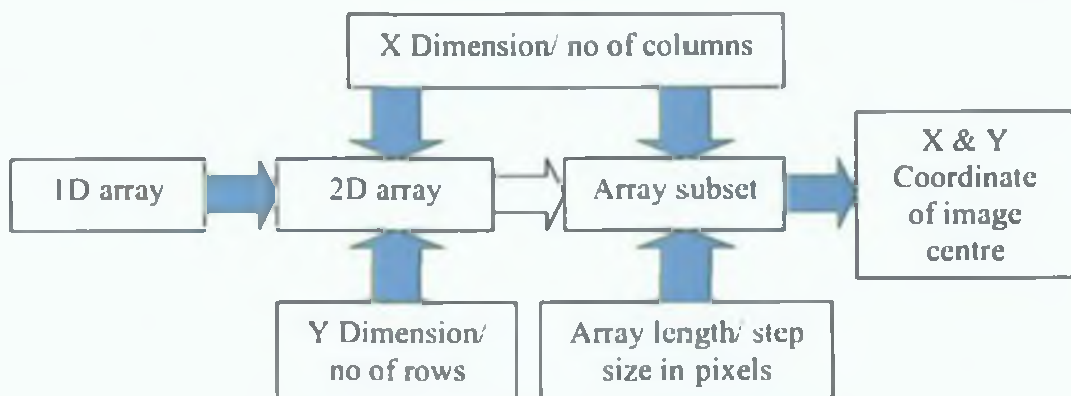


Figure 4.10: Programming flow for calculate image center from line scan data.

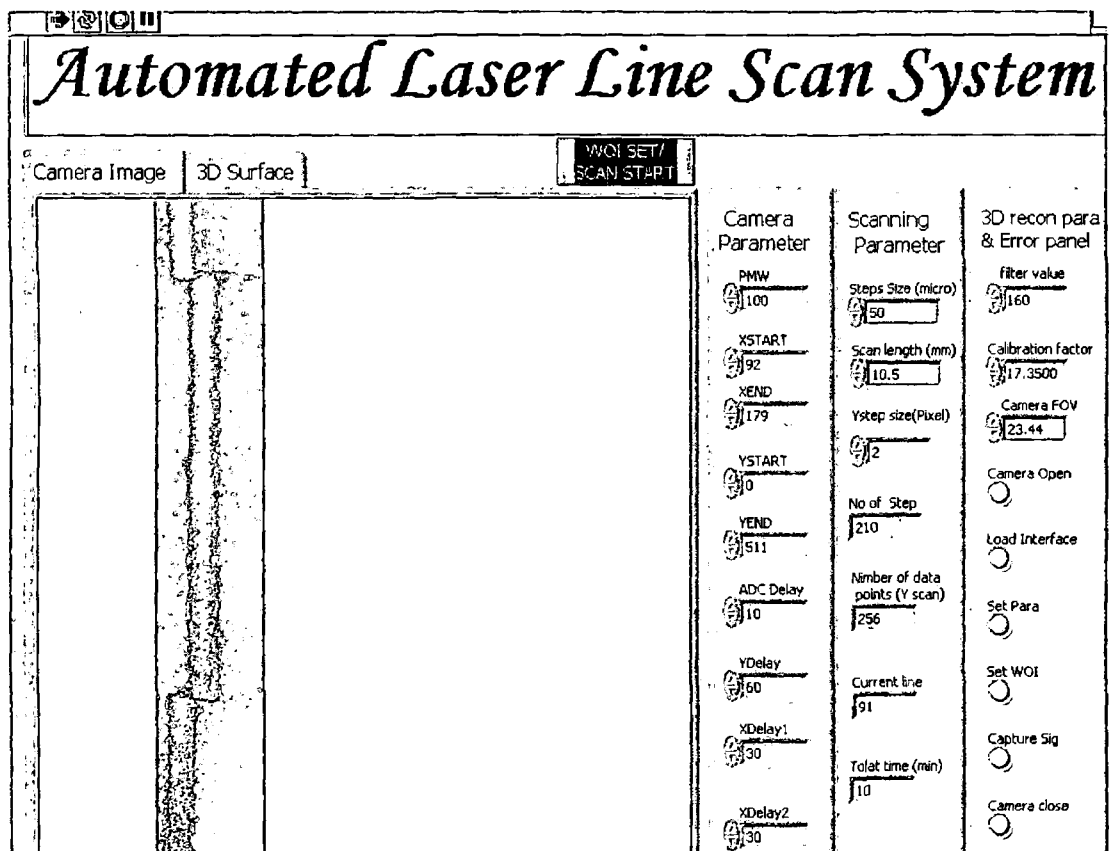


Figure 4.11: LabView front panel of the laser line scanning.

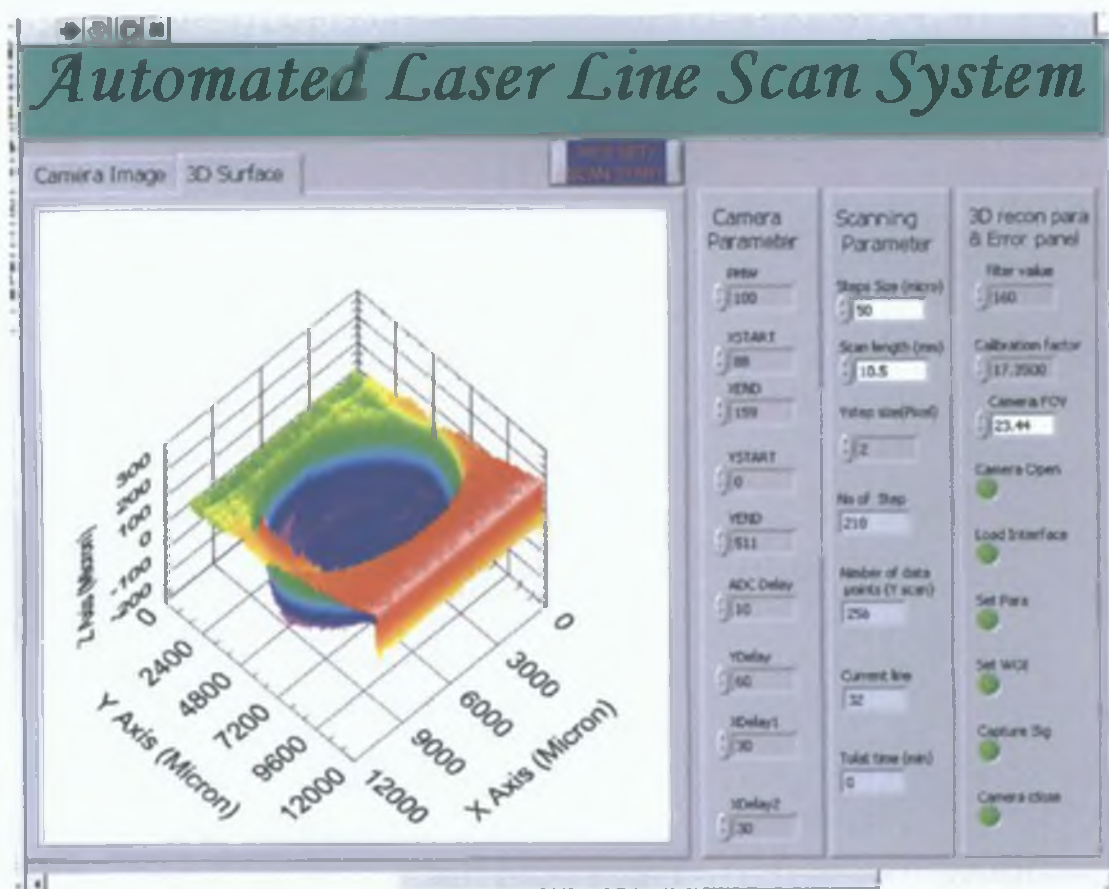


Figure 4.12: Front panel of the laser line scanning system showing an example of a 3D surface profile of stainless steel sample surface.

### 4.3 Surface roughness measurement

A graphical user interface (GUI) has been developed in LabView programme for roughness parameters measurement. Roughness parameters computed according to formulas describe in section 2.6 of Chapter two. These include average roughness  $R_a$ , the root mean square  $R_q$ , skewness  $R_{sk}$ , and kurtosis  $R_{ku}$ . This program takes an array of depth values from the scan surface as input. Figure 4.13 shows the programming block diagram for surface roughness parameters calculation. This GUI also works by the same scanning procedure discussed in section 4.1.

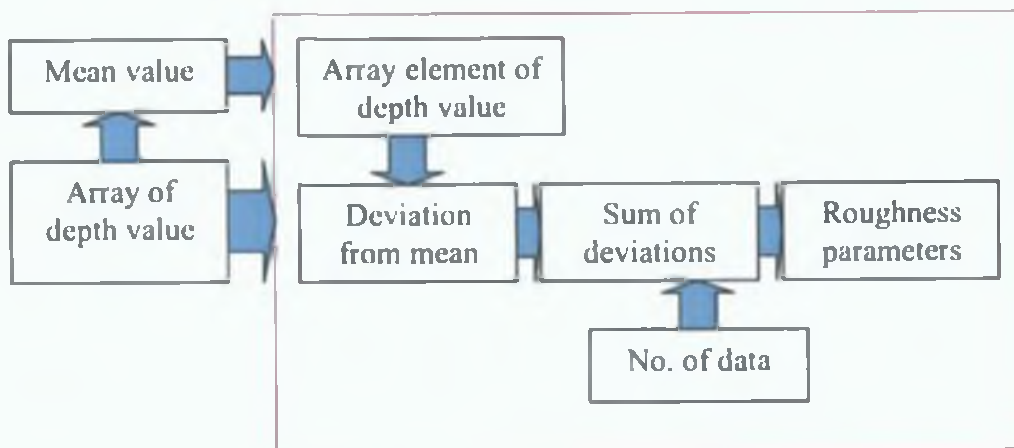


Figure 4.13: Programming block diagram of surface roughness parameters measurement.

LabView front panel with a surface roughness profile of the surface roughness parameters measurement system is shown in figure 4.14. In order to measure surface roughness parameters the user has to set WOI, filter value, depth calibration factor, scan length ( $\mu\text{m}$ ), step size ( $\mu\text{m}$ ), axis (X or Y) and direction. Inputs, outputs and errors control panel are shown on the right hand side of GUI.



Figure 4.14: LabView front panel of the automated surface roughness parameters measurement showing surface roughness profiles.

4.4 Generate 2D profiles from 3D surface map

Another GUI has been developed to generate 2D surface profiles from 3D surface map, shown in figure 4.15. From CWGraph3D control properties, the user has to add a cursor to extract data points from 3D surface map is shown in figure 4.16. The user can generate 2D profile along any line in the X and Y direction. A 3D surface map, number of steps in both direction, Y axis step index for 2D surface profile in the X direction and X axis step index for 2D profile in the Y direction are the inputs of this GUI.

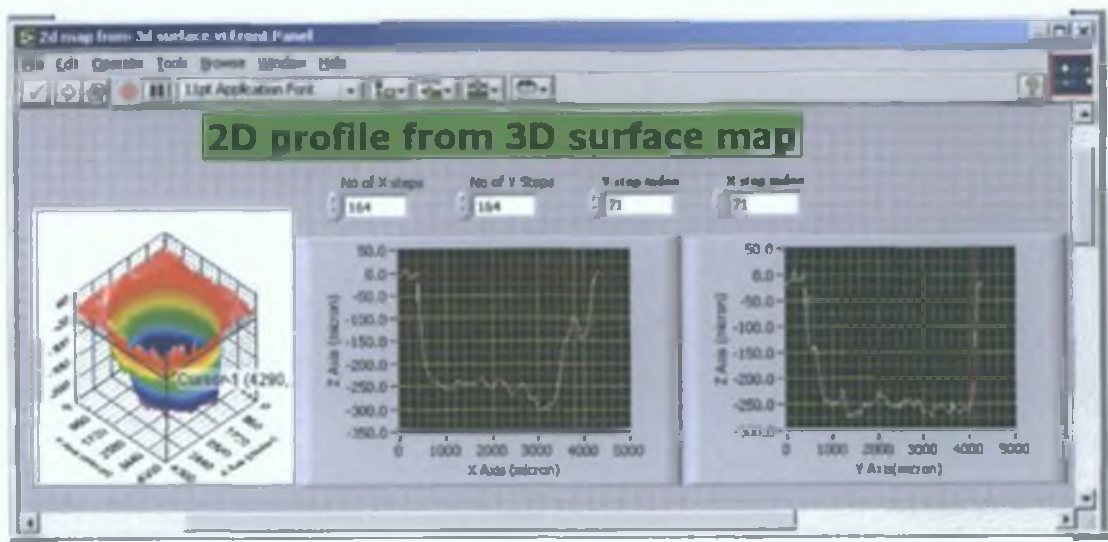


Figure 4.15: LabView GUI for 2D profiles from 3D surface map.

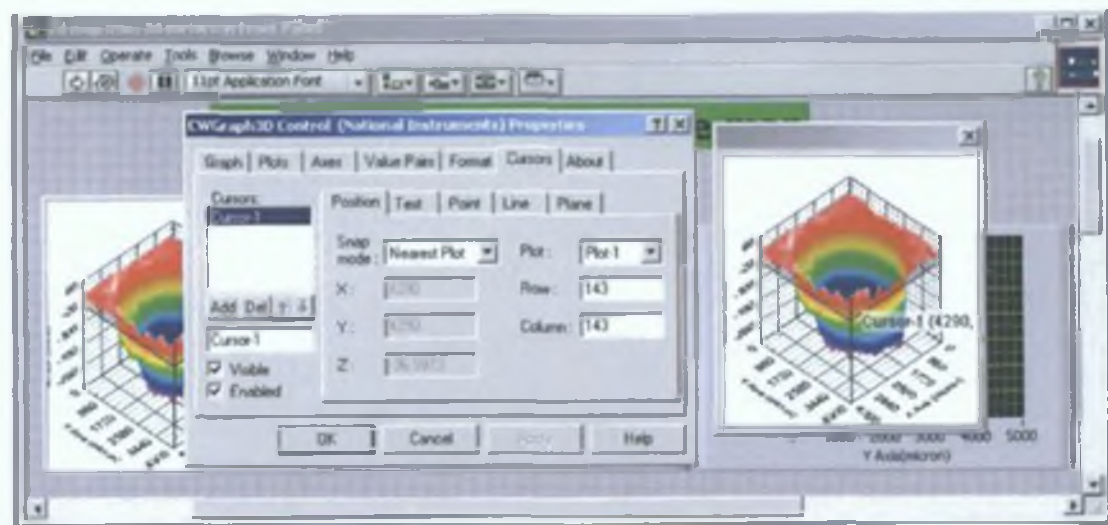


Figure 4.16: LabView CWGraph3D control properties.

# Chapter Five

## Automated surface scans results

### 5.1 Introduction

An automated surface inspection system was developed. Scan area capacity of this system is 12 mm by 12 mm area. This system was capable to create 2D and 3D surface profiles; also able measure surface roughness parameters from scan sample surface. Following data processing steps are involved in the developed system for a surface inspection:

- Capture laser spot image
- Threshold the spot image
- Calculate the image spot center
- Calculate the centre position shift with respect to a reference point and
- Calculate the depth value [depth value = image centre shift (pixel) \* calibration factor ( $\mu\text{m}/\text{pixel}$ )]

### 5.2 System parameters

System parameters such as camera viewing length by each pixel, focal spot size, depth focus of the laser beam, filter value and depth calibration factor are presented in this section.

#### 5.2.1 Camera viewing length, focal spot size and depth of focus

Camera viewing depends on the focusing system. If  $L$  is the camera viewing at a distance  $H$  between sample and focusing lens shown in figure 5.1; then camera viewing by each pixel  $P$ , expressed by the following relation:

$$P = \frac{L}{N}$$

where, N is the total number of pixels in one direction for N-by-N array detector. CCf15 CMOS camera consists of a 512 by 512 array detector. Camera viewing length for different lens conditions are summarized in the Table 5.1. Figure 5.2 shows a ruler image viewed by the camera with a 50 mm focal length additional lens.

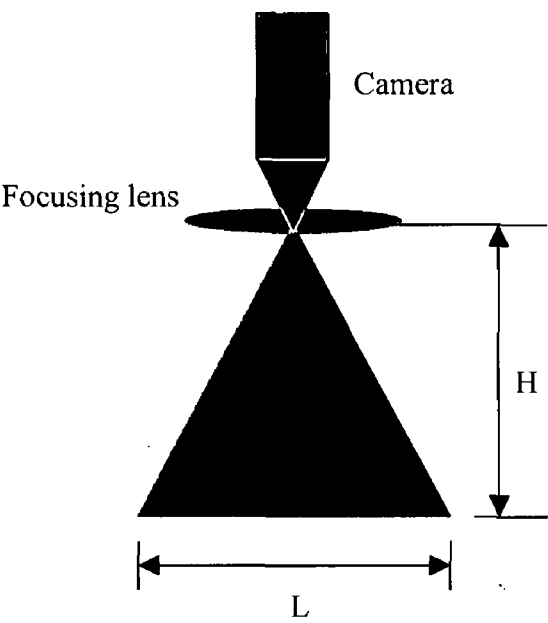


Figure 5.1: Camera viewing length.

Table 5.1: Camera viewing length with different focusing lens.

	Lens distance from sample surface, H (mm)	X & Y viewing length, L (mm)	Resolution (μm/pixel)
Camera lens only	450	105	205
	250	66	129
	150	40	78
With additional 100 mm focal length lens	150	24	46.88
	45	16	31.25
With additional 50 mm focal length lens	45	12	23.44
X5 objective lens	21	1.7	3.3
X10 objective lens	7.5	0.75	1.46



Figure 5.2: Camera image of a ruler with camera lens and additional 50 mm focal length lens (mm scale).

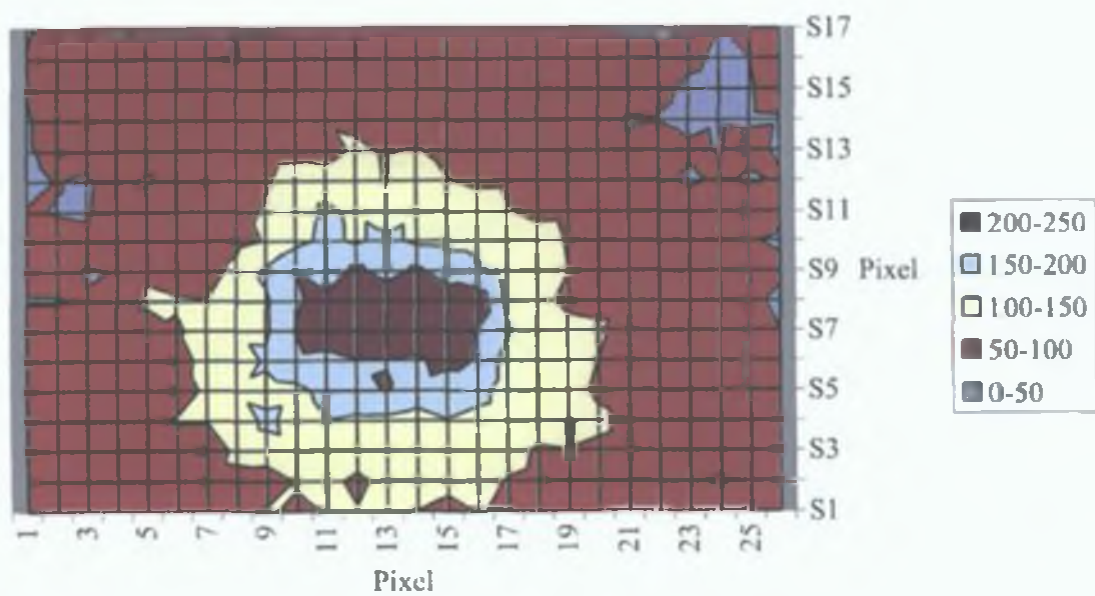


Figure 5.3: Intensity distributions of the laser spot.

A laser spot image intensity distribution for an additional 50 mm lens with camera shown in figure 5.3. The spot consist of 8 by 7 pixel at intensity 150. So spot size of the laser diode module is 187 by 164  $\mu\text{m}$ .

Depth of focus of the laser beam expressed by

$$DOF = 2.44\lambda(f/d)^2$$

For laser spot scanning, focal length of the beam focusing lens,  $f = 100 \text{ mm}$ , unfocused beam diameter,  $d = 1 \text{ mm}$  and wavelength of the laser diode,  $\lambda = 670 \text{ nm}$ .

So depth of focus of the laser beam is

$$DOF = 2.44 * 0.00067 \left( \frac{100}{1} \right)^2 \text{ mm}$$

$$DOF = 16.35 \text{ mm}$$

### 5.2.2 Noise threshold for data processing

The first step in the target location procedure is generally the subtraction of a threshold intensity value. The threshold subtraction is based on the supposition that there will always be background noise in any digital image.

In the inspection system laser beam was incident on the surface and it created a spot for laser spot triangulation. For laser line scanning system a laser line was projected on the surface. The CCf15 camera viewed the spot or line and was used to capture the image. The brightness of the beam spot or line on the surface was dependent upon the reflectance of the surface and the camera lens aperture. Images of the surfaces were represented by the gray scale intensity values ranging from 0 to 255. Figures 5.4 shows a beam intensity profile of laser spot image with a camera lens aperture 16. A 50 mm focal length additional lens with the camera and a 100 mm focal length lens used to focus the beam on to the sample surface. Profile image size or window of interest was 32 by 26 pixels.

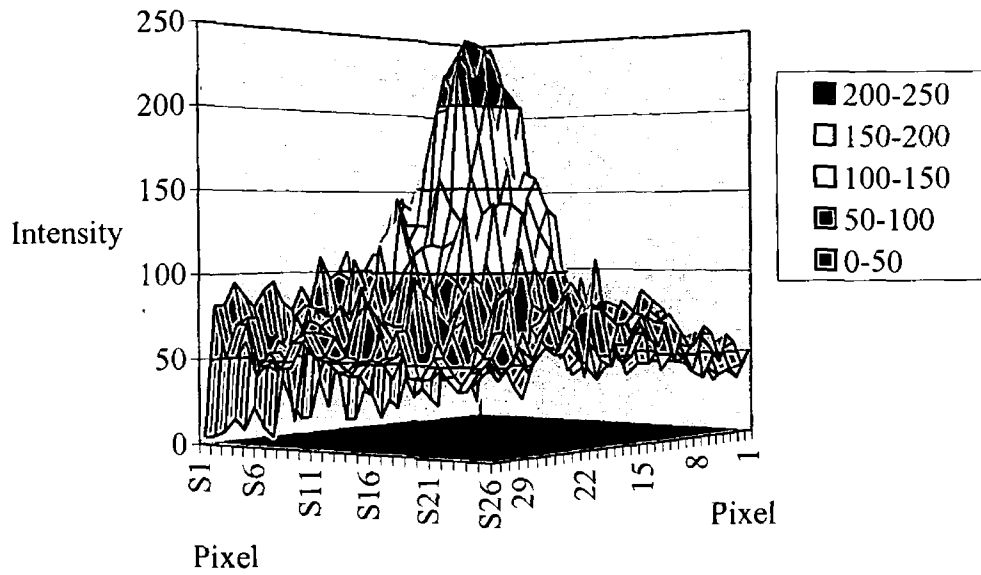


Figure 5.4: Laser spot intensity profile.

### 5.2.3 Depth calibration factor

From the triangulation theory, section 2.11.1 of chapter two and Appendix A, it is seen that the distance in depth direction is proportional to the lateral shift of the beam spot. The calibration factor represents the relationship of the depth displacement to the beam shift on the sensor surface and is measured in  $\mu\text{m}$  per pixel. The calibration factor is dependent on the triangulation angle, on the magnification of the reception optical system and the sensor dimension. In order to determine the calibration factor, the laser beam was incident on the sample held on the XY automated translation stage and the sample was moved along the Z-axis by  $20\ \mu\text{m}$  increments in order to calculate vertical shift of the sample surface. An image of the spot was recorded every time the Z stage was incremented and total number of steps in the Z direction was 25. Calibration factor for different filter values are shown in Table 5.2. The results shown in this table are the averages of seven measurements and deviations were calculated according to the student t-distribution. A linear curve fit to the average of seven calibration data for filter value 160 is shown in figure 5.5.

Table 5.2: Depth calibration factor in micrometers per pixel  
for different filter values.

Filter Value	200	190	180	170	160
Calibration 1	21.023	20.094	18.111	15.124	12.24
Calibration 2	29.796	27.597	25.419	22.61	20.641
Calibration 3	22.018	21.989	22.119	22.586	22.656
Calibration 4	29.476	24.534	20.594	17.345	16.131
Calibration 5	30.895	25.467	21.667	18.073	16.609
Calibration 6	26.484	23.331	20.248	18.120	17.533
Calibration 7	22.299	22.035	18.795	16.047	15.614
Average	26	23.578	20.993	18.558	17.345
Stan. Dev	4.184	2.508	2.421	2.962	3.420
Confidence interval (+/-)	3.072	1.842	1.778	2.175	2.511

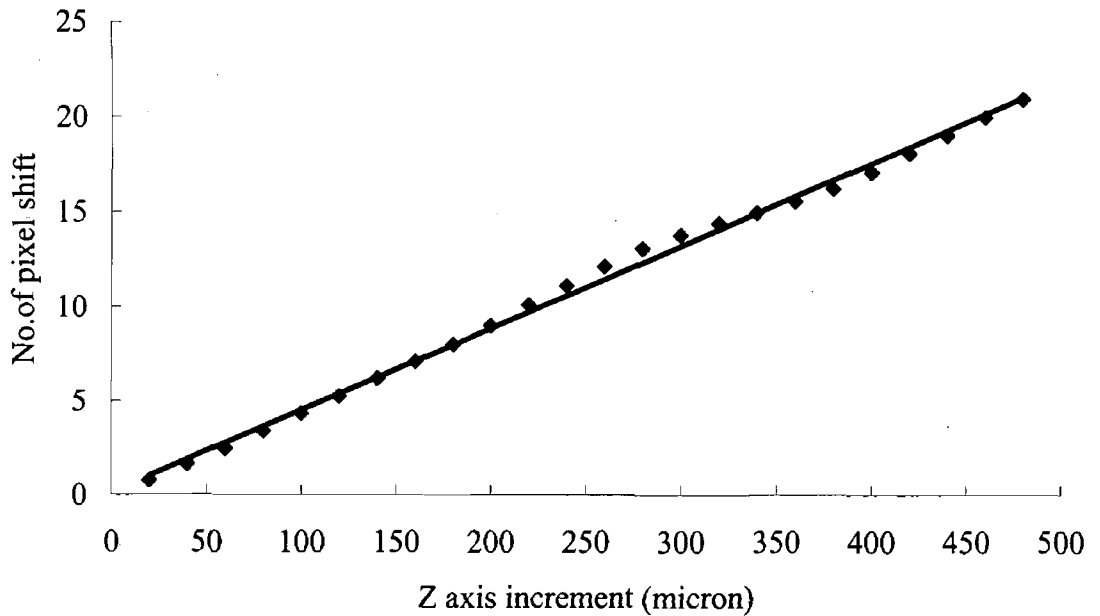


Figure 5.5: System calibration curve with a filter value 160.

### 5.2.4 Depth calibration factor from known $R_a$ sample

Mean surface roughness  $R_a$  expressed by the following equation

$R_a = \frac{\sum_0^N D}{N}$  where, D is the profile depth , and N is total number of data points. If B is the beam center shift in terms of pixel and Z is the depth calibration factor in  $\mu\text{m} / \text{pixel}$  then above equation can be expressed by:

$$R_a = \frac{\sum_0^N (B * Z)}{N}$$

$$\Rightarrow R_a = \frac{(B_1 + B_2 + B_3 + ..... + B_N) * Z}{N}$$

$$\Rightarrow R_a = X * Z$$

Here X is average beam centre shift in pixel. Finally depth calibration factor Z can be expressed by the following equation:

$$Z = \frac{R_a}{X} \tag{5.1}$$

The depth calibration factor was also calculated from a Mitutoyo precision calibration specimen surface with a known roughness value of 3.05  $\mu\text{m}$   $R_a$ . These scans were performed over a sample length of 800  $\mu\text{m}$  with a step size 20  $\mu\text{m}$ . Beam shift in terms of pixel were recorded during scanning and calibration factor calculated by the equation 5.1. Results from these scans are shown in Table 5.3. Deviations were calculated according to the student t-distribution.

Table 5.3: Depth calibration factor from precision specimen sample.

Test	X (pixel)	Z ( $\mu\text{m}/\text{pixel}$ )
1	0.1876	16.26
2	0.1780	19.66
3	0.1513	20.16
4	0.2145	14.22
5	0.1547	16.51
Average	0.1772	17.36
Stan. Dev.		2.233
Confidence interval (+/-)		2.129

### 5.3 Automated surface scan

Automated surface scans results are presented in this section. 3D surface profiles generated automatically by the developed LabView GUI from the sample surface. In order to scan a sample surface set the image size (WOI), scan area (X and Y axis length), step size, filter value and system calibration factor as inputs in the LabView GUI. According to the triangulation principle if the surface displace in the vertical direction from its original position the image centre shift proportionally on to the sensor. To generate 3D surface map first capture image data in every step then calculate centre of the image, calculate beam shift with a reference point and finally calculate depth value. Details measurement principles discuss in chapter 3, programming flow diagrams for scanning and 3D reconstruction are presented in chapter 4. All scans was performed with a 100  $\mu\text{m}$  step size in X and Y-axis, camera aperture was 16 and sample position was set perpendicular to the camera. Laser light was directed onto the target surface at a triangulation angle  $45^\circ(\theta)$ . A filter value of 160 and corresponding system calibration factor of 17.35  $\mu\text{m}$  per pixel was used throughout the scanning. A scanning window of interest size (WOI) of 68 by 30 pixels was also used for scans.

Scanning was carried out for copper, stainless steel and plastic sample surfaces with different sized blind hole. 3D surface maps generated during the automated scanning, are presented in this section. Data points were extracted from the generated 3D surface maps by using *2D profiles from 3D surface map.vi*. An Oxford precision digital calliper with a resolution 0.01 mm was used to measure diameter and depth of the scan holes.

5.3.1 Automated scan of a copper sample

A binocular microscopic image of a blind hole from the copper sample surface is shown in figure 5.6. Results from scanning this hole are shown in figure 5.7. A scan length of 5 mm was used for both X and Y-axis. All scan parameters are shown in Table 5.4. Figure 5.8 shows the YZ perspective view from the 3D surface map and figure 5.9 shows a corresponding 2D surface profile, which was generate from this 3D surface map along the 28<sup>th</sup> Y-axis scan line. Figure 5.10 shows ZX perspective view and figure 5.11 shows corresponding 2D surface profile, which was generate from this 3D surface map along the 30<sup>th</sup> X-axis scan line. These 2D profiles were chosen as it passed through the centre of the hole. Diameter and depth of the hole measured by the digital calliper 3 mm and 540 µm respectively, and from the developed system diameter 3.1 mm in the Y direction, 2.9 mm in the X direction, and depth 425 µm from figure 5.9 and figure 5.11. Diameter was measured along 350 µm depth for both directions.

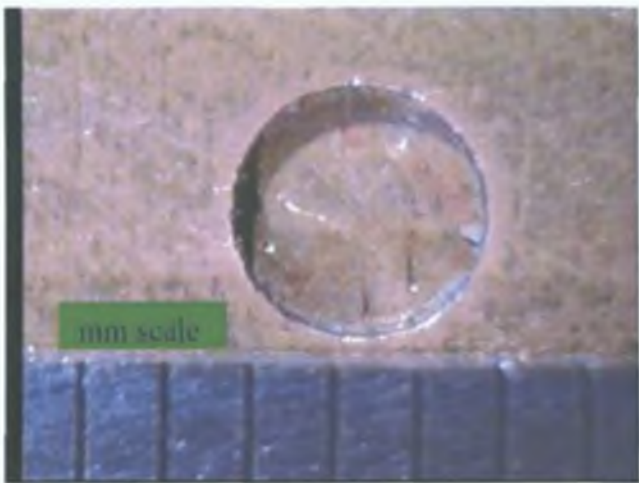


Table 5.4: Scan parameters.

Parameters	Inputs and outputs
Scan area	5 mm by 5 mm
No of steps	50 by 50
Total points	2500
Step size	100 µm
WOI	68 by 30
Total Time	84 minutes

Figure 5.6: Binocular microscopic image of a 3 mm blind hole of the Cu sample surface.

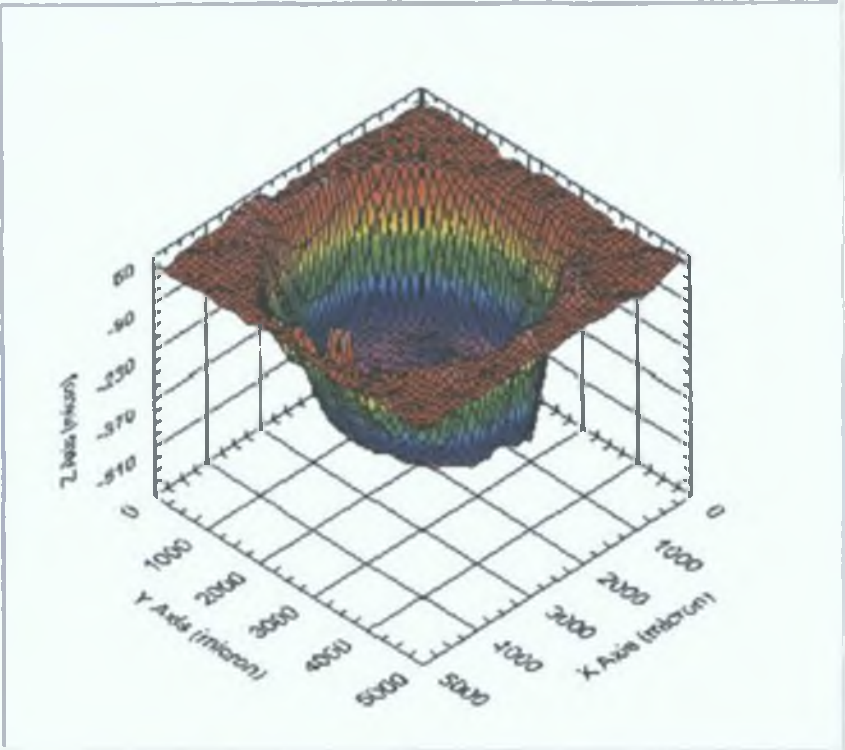


Figure 5.7: 3D surface map of the 3 mm blind hole.

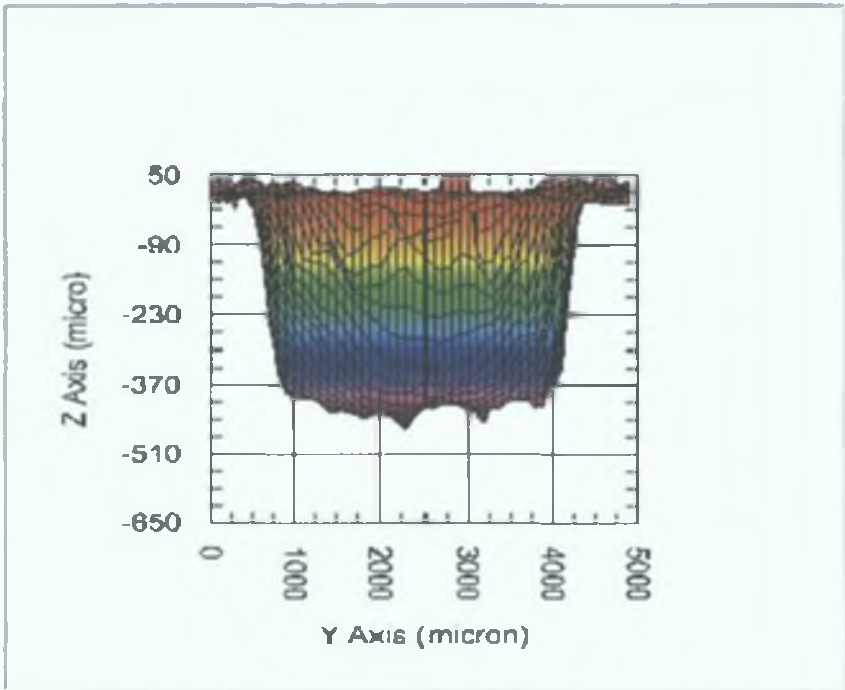


Figure 5.8: Perspective view from 3D surface map of the 3 mm hole in the YZ plane.

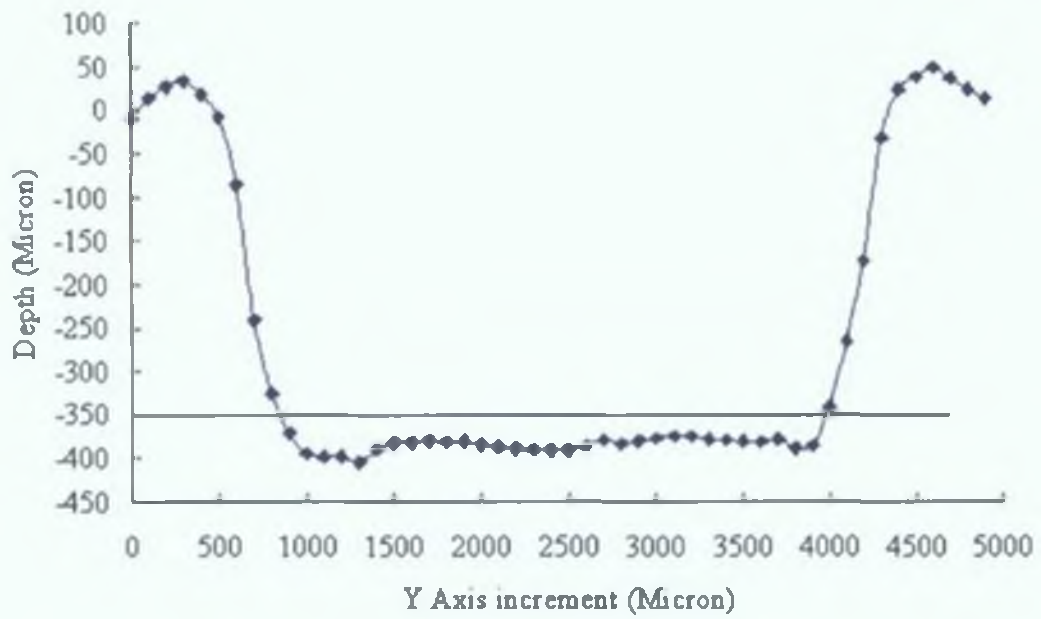


Figure 5.9: A 2D surface profile from 3D surface map of the 3 mm hole along the Y axis.

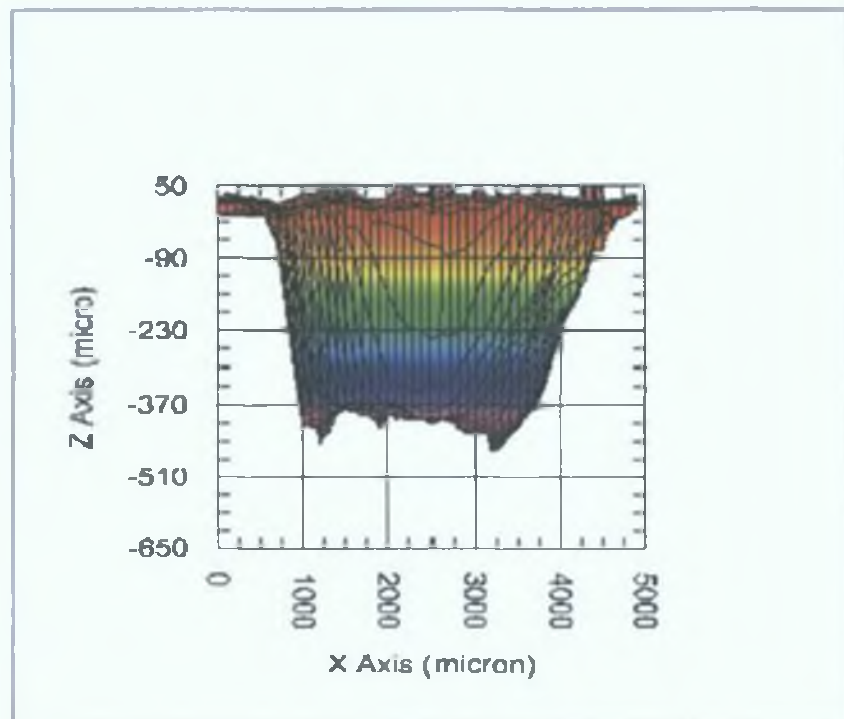


Figure 5.10: Perspective view from 3D surface map of the 3 mm hole in the XZ plane.

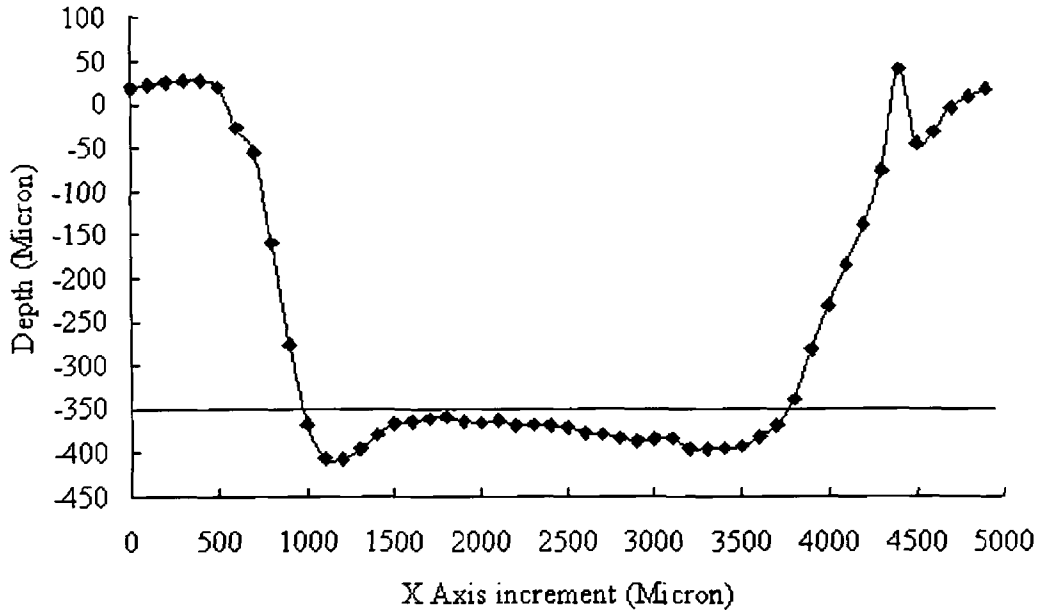


Figure 5.11: A 2D surface profile from 3D surface map of the 3 mm hole along the X axis.

### 5.3.2 Automated scan of a stainless steel sample

Binocular microscopic image of a blind hole from the stainless steel sample surface is shown in figure 5.12. Results from scanning this hole are also shown in a 3D surface map in figure 5.13 and figure 5.14 shows XY perspective view from this 3D surface map. A scan length of 9 mm was used for both X and Y-axis. All scan parameters are summarised in the Table 5.5. Figure 5.15 shows a 2D surface profile, which was generate from this 3D surface map along the 40<sup>th</sup> X-axis scan line. Figure 5.16 shows another 2D surface profile, which was also generate from this 3D surface map along the 42<sup>nd</sup> Y-axis scan line. These 2D profiles were chosen as at passed through the centre of the hole. Diameter and depth of this hole measured by the digital calliper 5.9 mm and 600  $\mu\text{m}$  respectively, and from the developed system diameter 6.3 mm in the X direction and 6.4 mm in the Y direction, and depth 500  $\mu\text{m}$  from figure 5.15 and figure 5.16. Diameter was measured along 350  $\mu\text{m}$  depth for both directions.

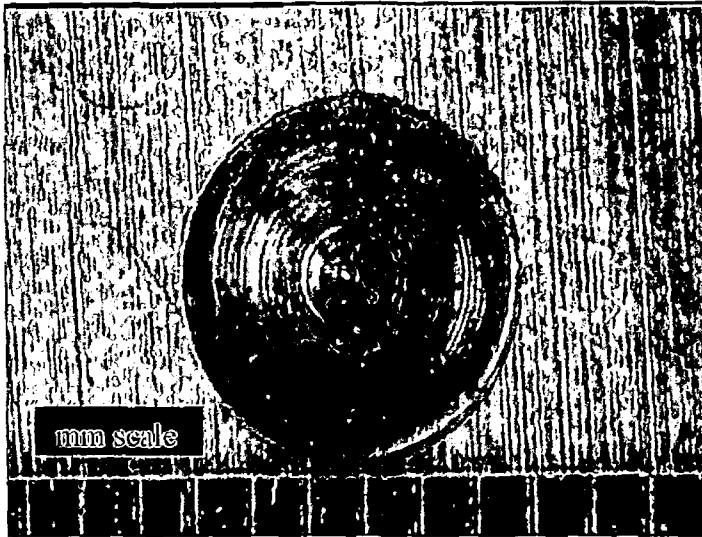


Table 5.5: Scan parameters

Parameters	Inputs and outputs
Scan area	9 mm by 9 mm
No of steps	90 by 90
Total points	8100
Step size	100 $\mu$ m
WOI	68 by 30
Total Time	261 minutes

Figure 5.12: Binocular microscopic image of a 5.9 mm blind hole from the stainless steel sample surface.

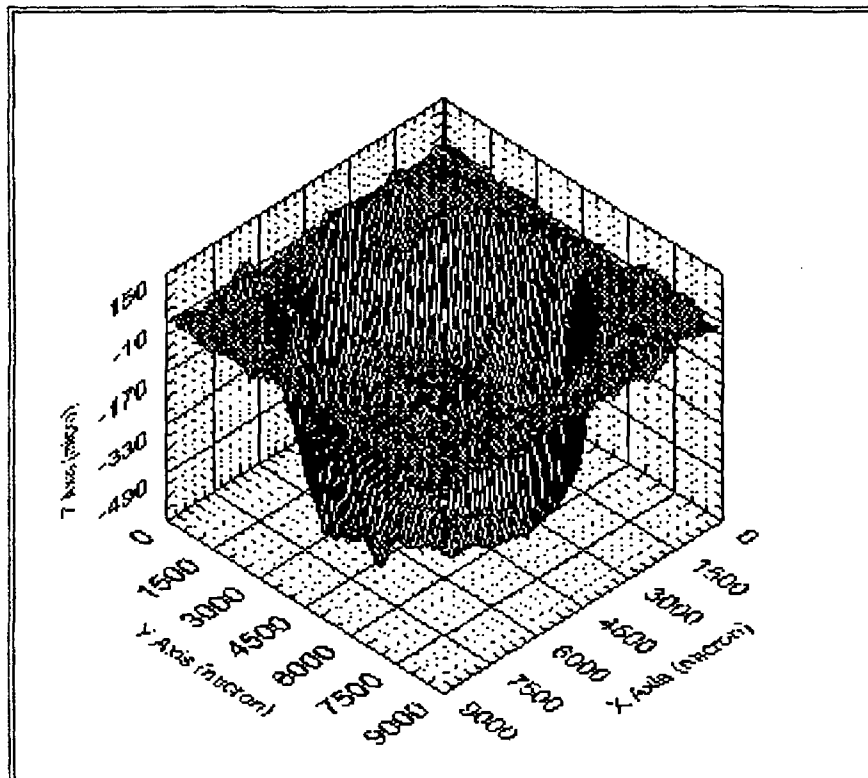


Figure 5.13: 3D surface map of the 5.9 mm blind hole.

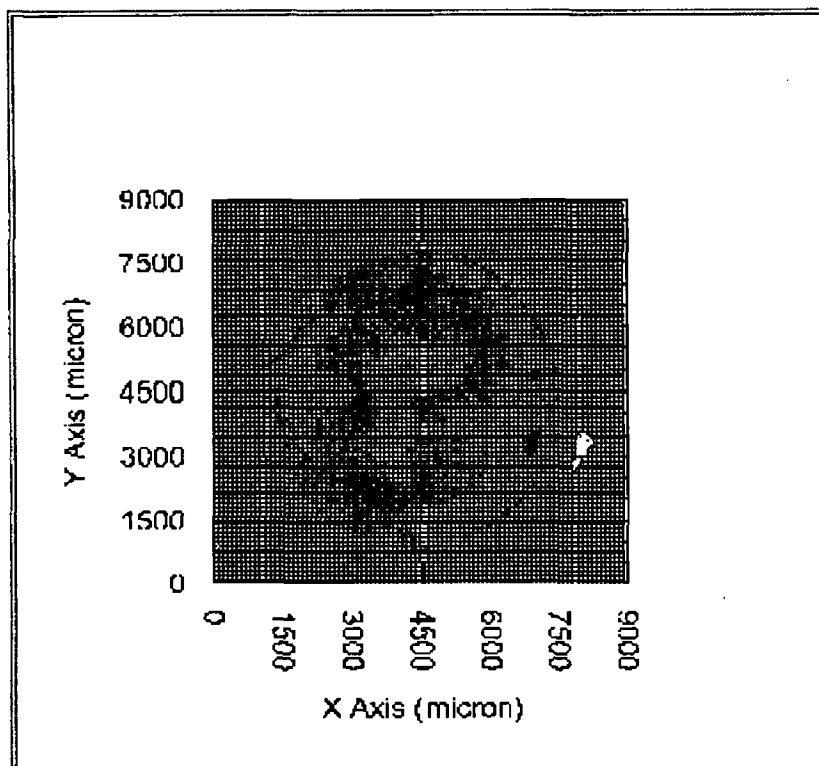


Figure 5.14: Perspective view from 3D surface map of the 5.9 mm stainless steel surface blind hole in the XY plane.

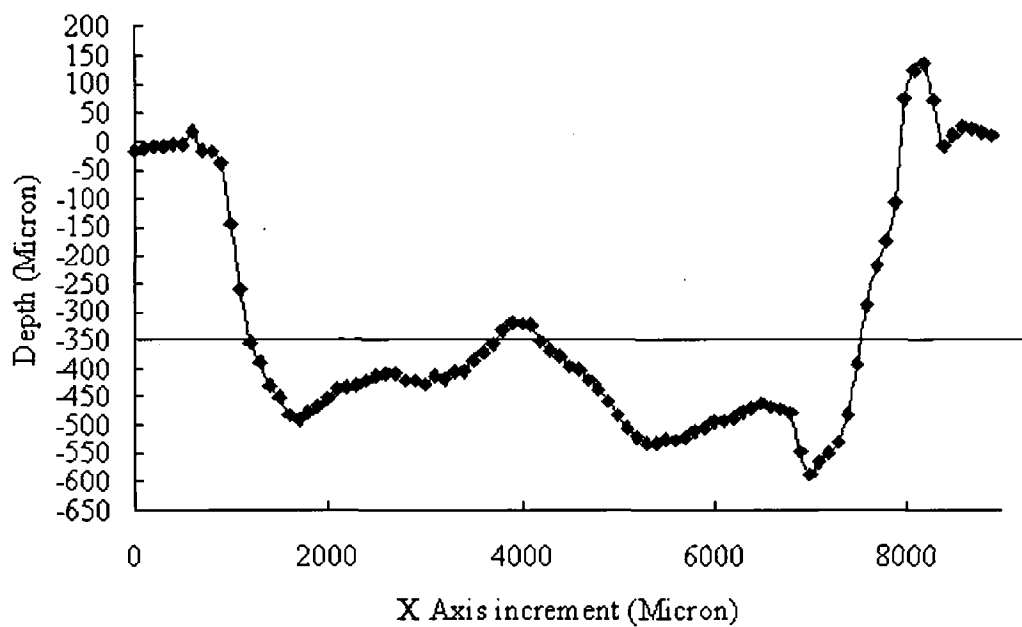


Figure 5.15: A 2D surface profile from 3D surface of the 5.9 mm stainless steel blind hole along the X axis.

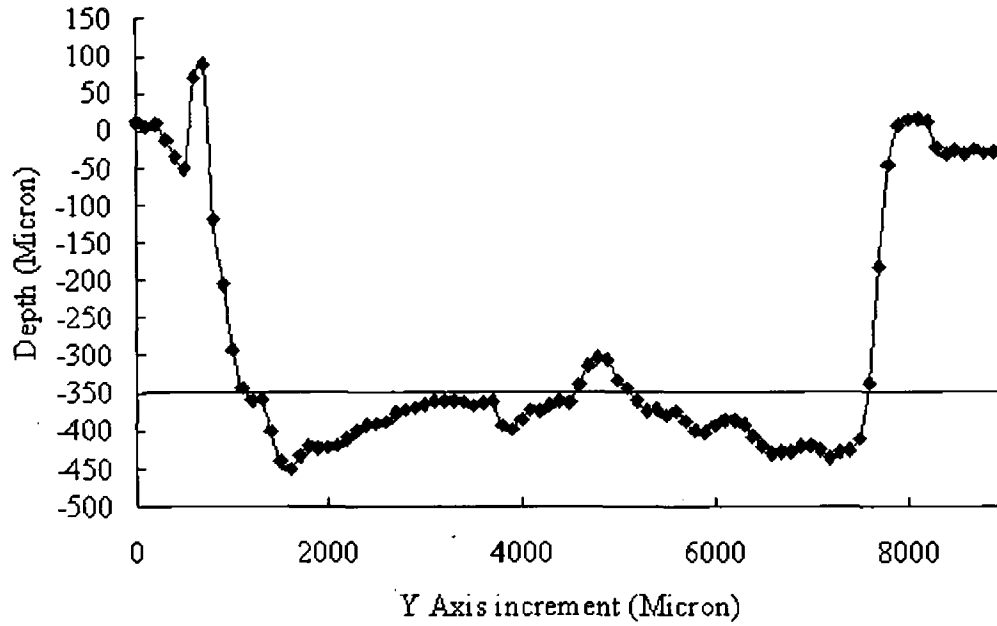


Figure 5.16: A 2D surface profile from 3D surface of the 5.9 mm stainless steel blind hole along the Y axis.

### 5.3.3 Automated scan of a plastic sample

Binocular microscopic image of the blind hole from the plastic sample surface is shown in figure 5.17 Results from LTS scanning of this hole are shown in a 3D surface map in figure 5.18 and figure 5.19 shows XY perspective view from the 3D surface map. A scan length of 6 mm was used for both X and Y-axis. All scan parameters are shown in Table 5.6. Figure 5.20 and figure 5.21 shows 2D profiles from this 3D surface map along the 32<sup>nd</sup> and the 28<sup>th</sup>, the X-axis and Y-axis scans line respectively. These 2D profiles were chosen as at passed through the centre of the hole. Diameter and depth of the hole measured by the digital caliper 4 mm and 600  $\mu\text{m}$  respectively, and from the developed system diameter 4.1 mm in the X direction and 4.3 mm in the Y direction, and depth 550  $\mu\text{m}$  from figure 5.20 and figure 5.21. Diameter was measured from along 350  $\mu\text{m}$  depth for both directions.



Table 5.6: Scan parameters

Parameters	Inputs and outputs
Scan area	6 mm by 6 mm
No of steps	60 by 60
Total points	3600
Step size	100 $\mu\text{m}$
WOI	68 by 30
Total Time	122 minutes

Figure 5.17: Binocular microscopic image of a blind hole from the plastic sample surface.

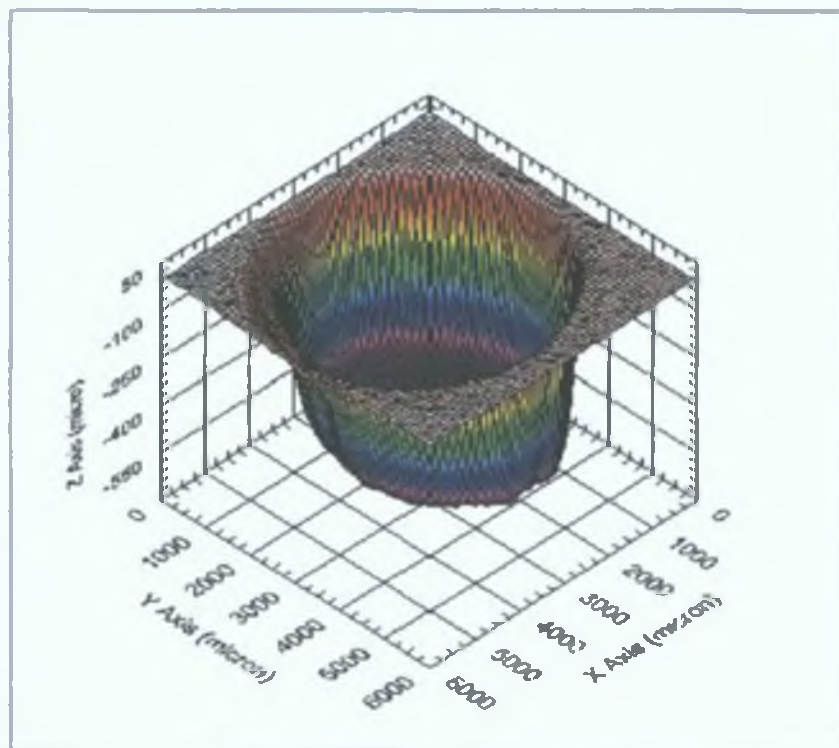


Figure 5.18: 3D surface of the plastic sample blind hole.

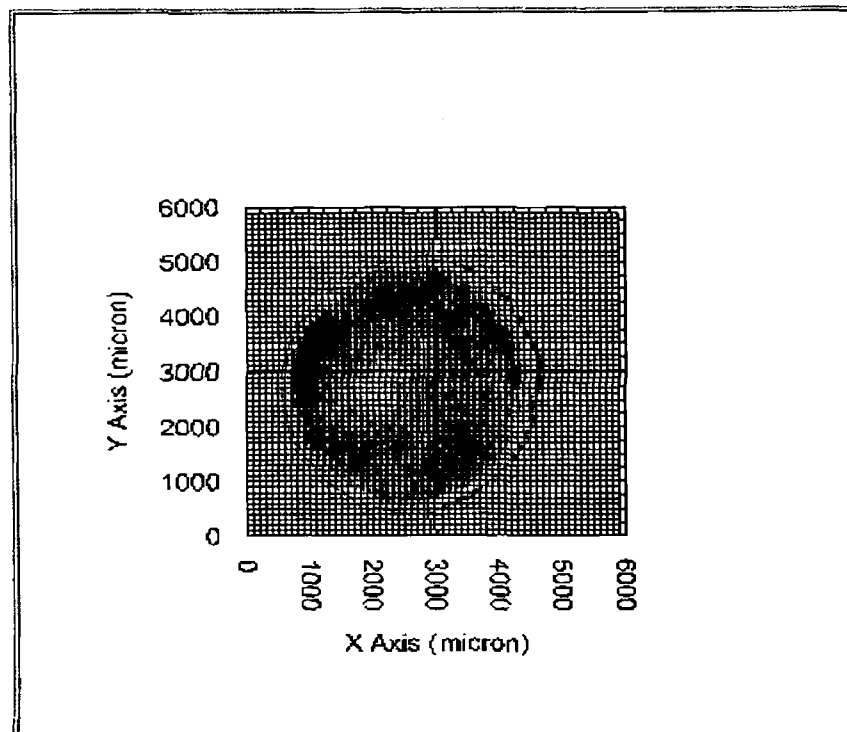


Figure 5.19: XY perspective for the 3D surface map of the plastic sample.

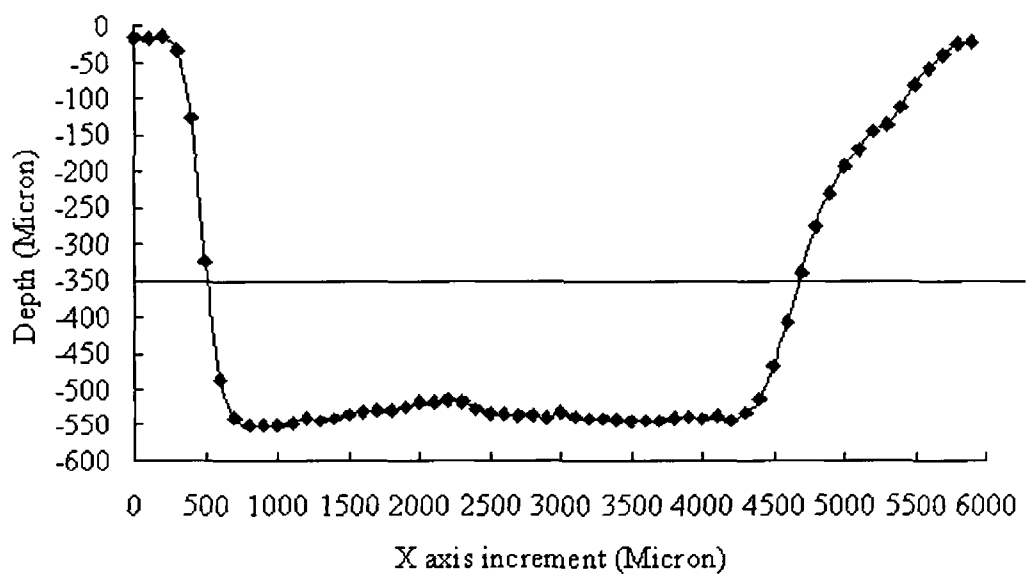


Figure 5.20: A 2D profile from the 3D surface map along the X-axis.

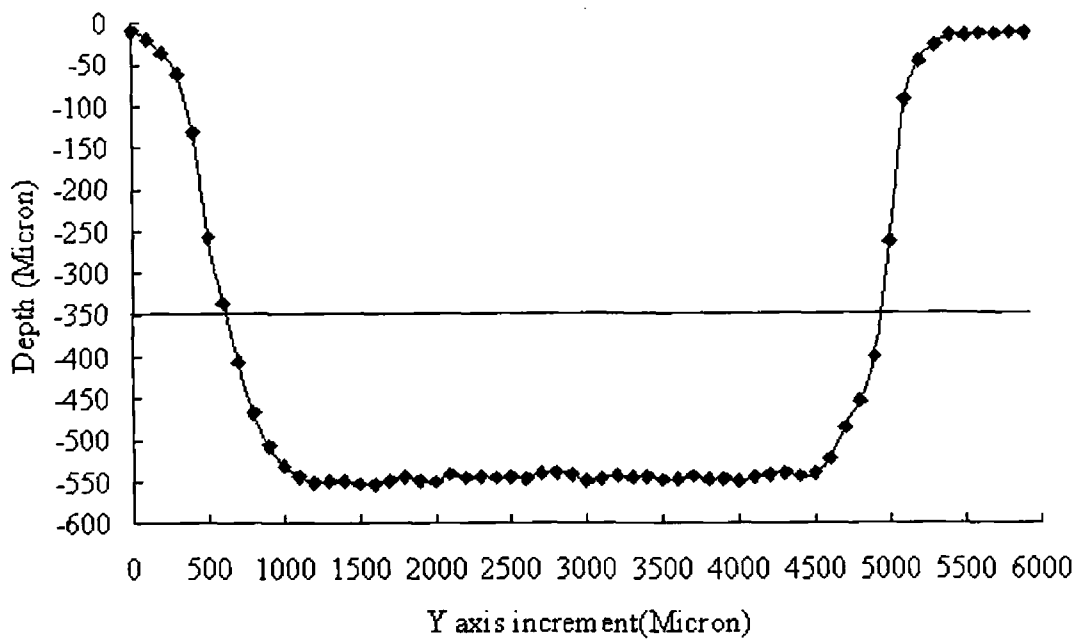


Figure 5.21: A 2D profile from the 3D surface map along the Y-axis.

### 5.3.5 Automated scan with different lens system

Surface topographic maps presented in this section are the surface scans by the LTS system with different lens system. A 150 mm focal length lens was use to focus the laser beam on to the sample surface and a 100 mm focal length lens was use with the camera. 2D image of an 8 mm blind hole from a stainless steel surface are shown in figure 5.22. Corresponding 3D surface profile of the stainless steel produced from the developed profiling system are shown in figure 5.23. Figure 5.24 and 5.25 shows respectively 2D image of a 4 mm hole from a copper surface and corresponding 3D surface map. 120 by 120 steps were used for the stainless steel and 60 by 60 steps were used for copper surface sample. Scanning was performed by a  $100\text{ }\mu\text{m}$  step size in X and Y-axis for both profiles and sample position was perpendicular to camera at an angle  $45^\circ$ .



Figure 5.22: Binocular microscopic image of an 8 mm blind hole from a stainless steel sample.

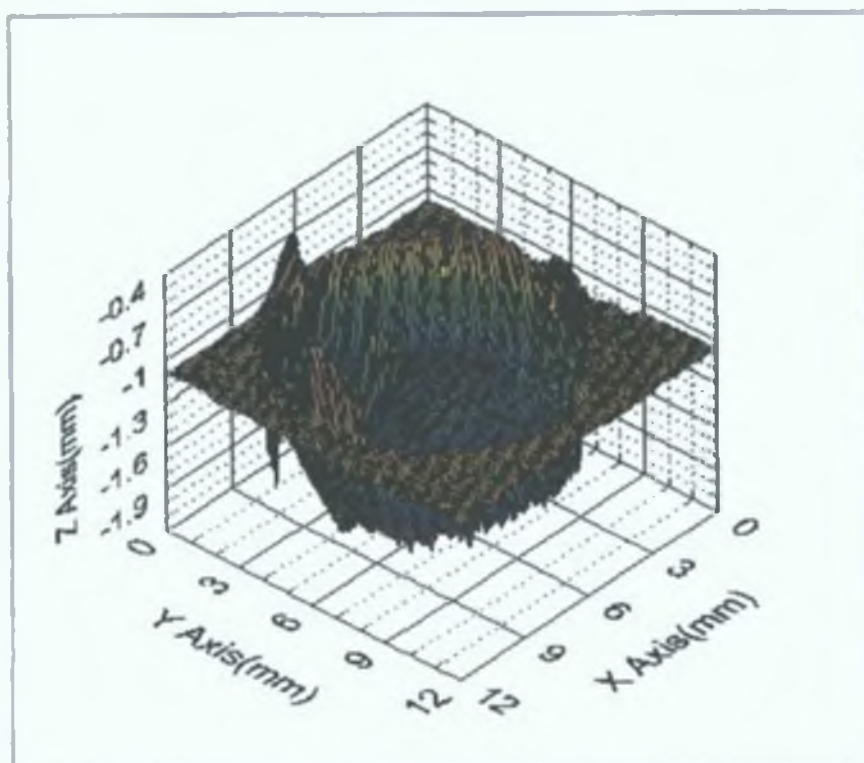


Figure 5.23: 3D surface map of the 8 mm blind hole.

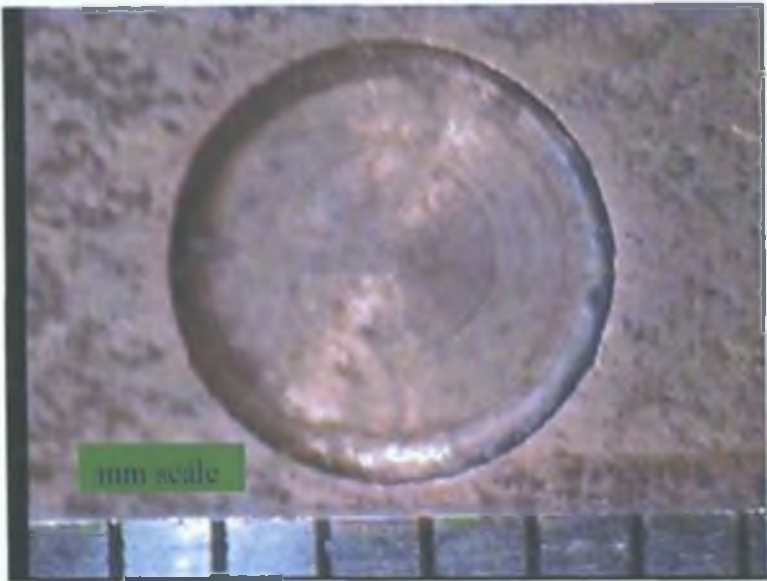


Figure 5.24: Binocular microscopic image of a 4 mm blind hole from a copper sample surface.

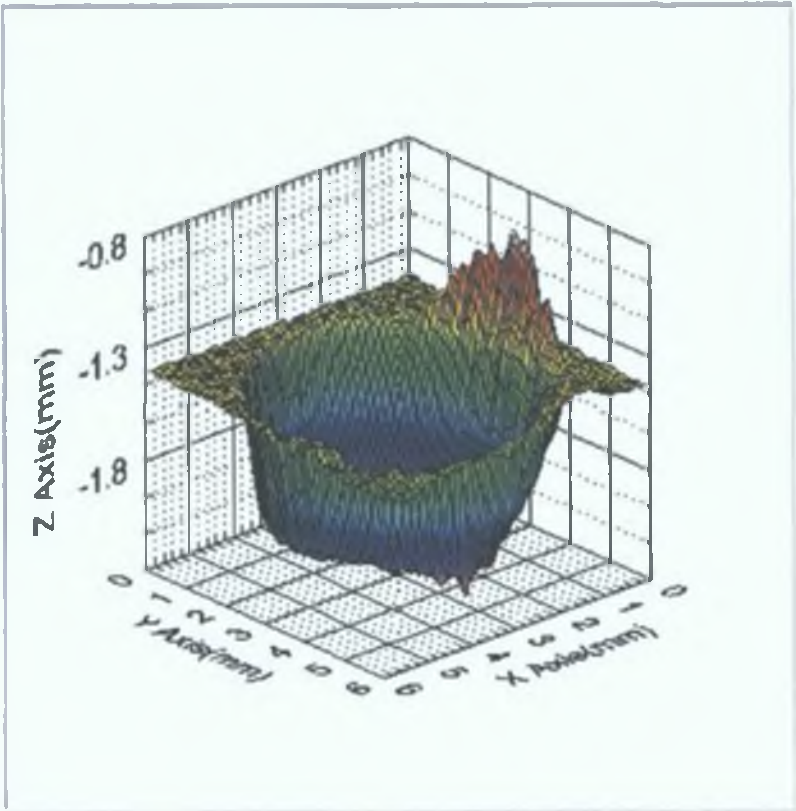


Figure 5.25: 3D surface map of the 4 mm blind hole.

#### 5.4 Compare with optical microscope

An elliptical shapes zero scan from a key surface by the system is presented in this section. Scan area was 3.35 mm by 2 mm with a step size 25  $\mu\text{m}$ . XY perspective view from 3D surface map of the zero shown in figure 5.26. Optical microscopic image of the zero is shown in figure 5.27. A 2D profile from this 3D surface map along the 70<sup>th</sup> X – axis scan line is shown in figure 5.28. Inner and outer dimension of the zero measured by the optical microscope are 668  $\mu\text{m}$  and 1324  $\mu\text{m}$  and from the developed system approximately 850  $\mu\text{m}$  and 1600  $\mu\text{m}$  respectively.

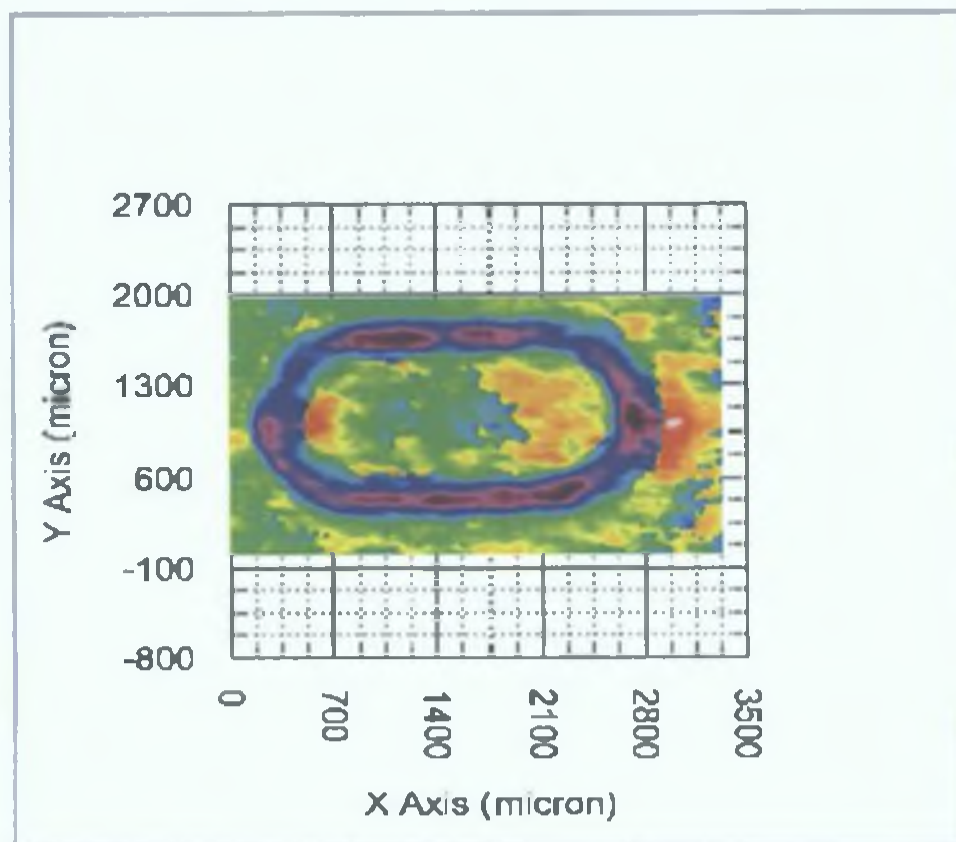


Figure 5.26: XY perspective view from 3D surface map of a key surface zero.

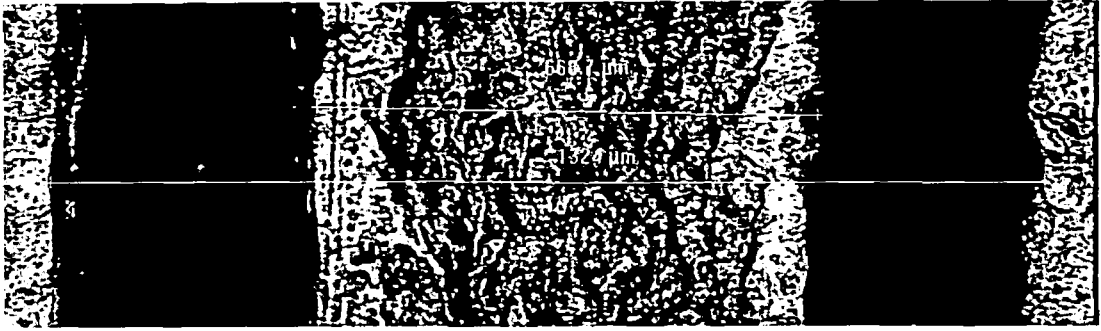


Figure 5.27: Optical microscopic image of a key surface zero.

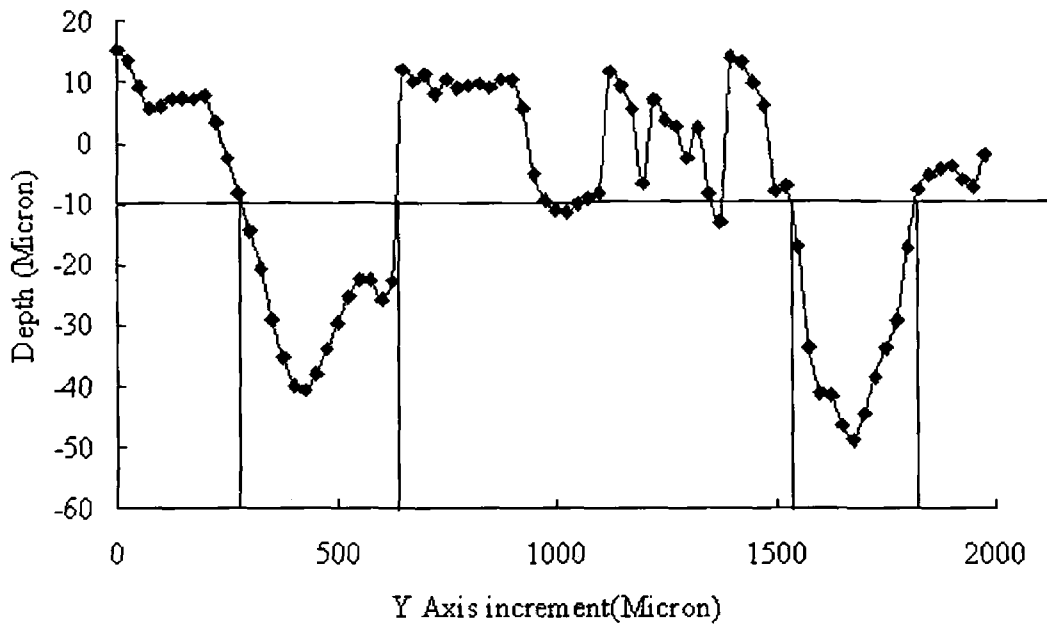


Figure 5.28: A 2D profile from the 3D surface map of the key surface zero.

### 5.5 System depth repeatability

A 5 mm diameter and 600  $\mu\text{m}$  depth blind hole from a plastic sample surface scan three times across the diameter and figure 5.29 to figure 5.30 shows respectively the 2D profiles of the first, second and third scan. Scans was performed over an 8 mm scan length with a step size 100  $\mu\text{m}$ .

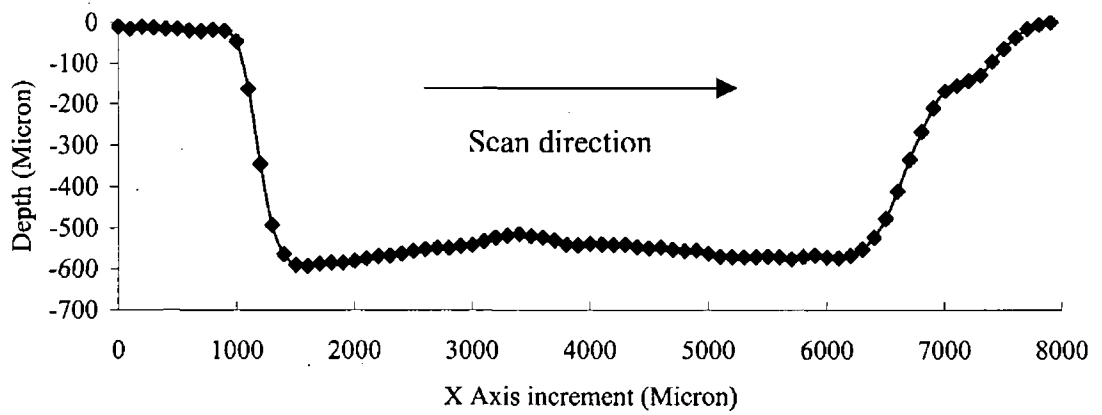


Figure 5.29: 2D surface profile of the 5mm blind hole from first scans.

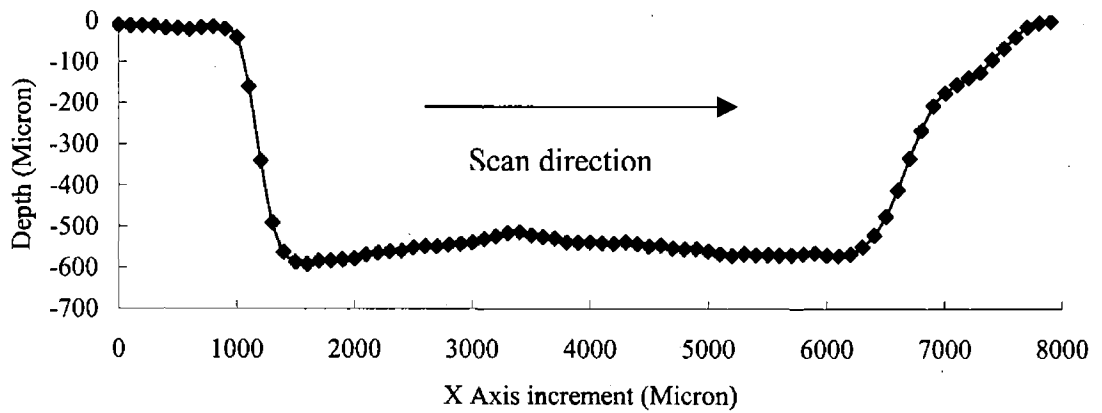


Figure 5.30: 2D surface profile of the 5mm blind hole from second scans.

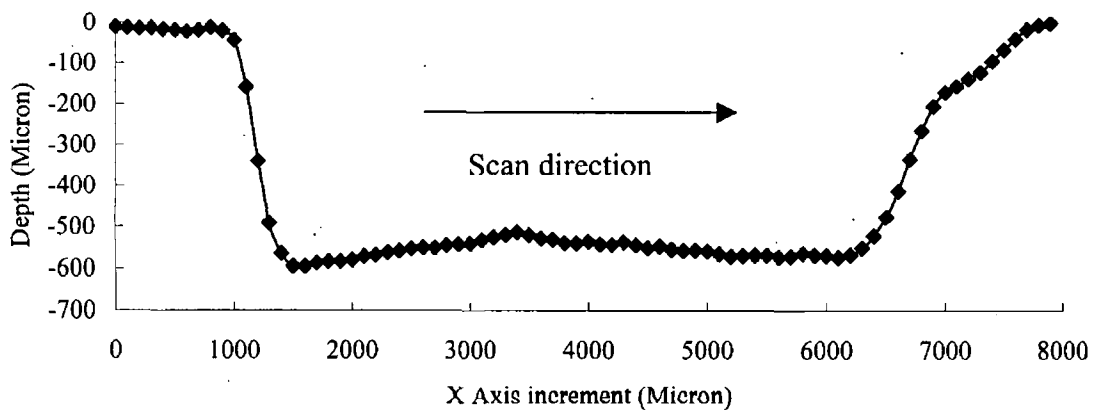


Figure 5.31: 2D surface profile of the 5mm blind hole from third scans.

Depth value for four different X-axis positions were taken from the above three scans data, shown in Table 5.7. Total depth of the hole also shown in the table was calculated between points 0  $\mu\text{m}$  and 1500  $\mu\text{m}$  in the X direction. Deviations were calculated according to the student t-distribution.

Table 5.7: Depth repeatability of the automated surface scanning system.

X axis position:	Depth value, $\mu\text{m}$				Total depth ( $\mu\text{m}$ )
	At 500 $\mu\text{m}$	At 3000 $\mu\text{m}$	At 5000 $\mu\text{m}$	At 7000 $\mu\text{m}$	
Scan 1	17.282	542.208	563.476	169.890	579.177
Scan 2	17.278	539.169	559.813	175.053	575.804
Scan 3	18.705	540.915	558.967	171.073	582.621
Average	17.755	540.764	560.752	172.005	579.201
Std. Dev.	0.823	1.525	2.397	2.705	3.409
Confidence interval (+/-)	1.388	2.574	4.045	4.565	5.753

### 5.6 Surface roughness parameters measurement results

Roughness parameters computed for by develop GUI includes average roughness,  $R_a$ , the root mean square,  $R_q$ , skewness,  $R_{sk}$ , and kurtosis,  $R_{ku}$ . This program takes as input a typical AFM profile data file. For comparison surface roughness parameters were measured with a Mitutoyo Surftest-402. Measurement was taken in cut-off value or cut length 0.8 mm and 10  $\mu\text{m}$  range and tip radius was 5  $\mu\text{m}$ . A Nano – R<sup>TM</sup> atomic force microscope (AFM) manufactured by Pacific Nanotechnology was also used to measured surface roughness parameters for comparison purposes. Sample length for the AFM measurements was 80 $\mu\text{m}$  and each measurement contained 256 data points. The two surfaces compared examined with these systems were a copper and stainless steel surface with milled blind holes. Roughness parameters measured by the above three methods on a stainless steel surface is shown in Table 5.8 and on a copper surface is shown in Table 5.9. Deviations were calculated according to the student t-distribution. Encouragingly the results of the three methods fall within the

same range and the deviations from the developed software are comparable to those of the commercial systems.

Table 5.8: Surface roughness parameters of a stainless steel surface.

Profile	AFM		AFM data analysis by the developed software				Surftest-402	
	R <sub>a</sub> ( $\mu\text{m}$ )	R <sub>q</sub> ( $\mu\text{m}$ )	R <sub>a</sub> ( $\mu\text{m}$ )	R <sub>q</sub> ( $\mu\text{m}$ )	R <sub>sk</sub> ( $\mu\text{m}$ )	R <sub>ku</sub> ( $\mu\text{m}$ )	R <sub>a</sub> ( $\mu\text{m}$ )	R <sub>q</sub> ( $\mu\text{m}$ )
A	0.70	0.77	0.32845	0.4351	-1.1896	4.2957	0.73	0.97
B	0.68	0.82	0.5872	0.7048	-0.6265	2.5803	0.50	0.67
C	0.92	1.10	0.6125	0.7616	-0.2380	2.5774	0.73	1.00
Average	0.77	0.90	0.51	0.63	-0.68	3.15	0.65	0.88
Confidence interval (+/-)	0.22	0.3	0.27	0.29	0.81	1.67	0.22	0.31

Table 5.9: Surface roughness parameters of a copper surface.

Profile	AFM		AFM data analysis by the developed software				Surftest-402	
	R <sub>a</sub> ( $\mu\text{m}$ )	R <sub>q</sub> ( $\mu\text{m}$ )	R <sub>a</sub> ( $\mu\text{m}$ )	R <sub>q</sub> ( $\mu\text{m}$ )	R <sub>sk</sub> ( $\mu\text{m}$ )	R <sub>ku</sub> ( $\mu\text{m}$ )	R <sub>a</sub> ( $\mu\text{m}$ )	R <sub>q</sub> ( $\mu\text{m}$ )
A	0.46	0.54	0.4515	0.5286	-0.3651	1.8239	0.90	1.45
B	0.68	0.79	0.6911	0.8021	-0.9047	2.4100	1.10	1.40
C	0.79	0.94	0.8468	0.9556	0.0387	1.6684	1.45	1.85
Average	0.64	0.76	0.66	0.76	-0.41	1.97	1.15	1.57
Confidence interval (+/-)	0.28	0.34	0.34	0.37	0.80	0.66	0.47	0.42

Surface roughness parameters were measured on a Mitutoyo precision sample. Tests were performed five times by both the Surftest – 402 and the LTS system, and results from these tests are shown in Table 5.10. For the Surftest – 402 measurement was taken in cut-off value or cut length 0.8 mm and 10  $\mu\text{m}$  range and for LTS tests was performed over a sample length of 800  $\mu\text{m}$  with a step size 20  $\mu\text{m}$ . Deviations were calculated according to the student t-distribution.

Table 5.10: Surface roughness parameters measurements results.

Test	Surftest-402		LTS system			
	$R_a$ ( $\mu\text{m}$ )	$R_q$ ( $\mu\text{m}$ )	$R_a$ ( $\mu\text{m}$ )	$R_q$ ( $\mu\text{m}$ )	$R_{ku}$ ( $\mu\text{m}$ )	$R_{sk}$ ( $\mu\text{m}$ )
1	3	3.3	3.23	4.07	3.82	-0.74
2	3	3.3	3.37	3.90	2.04	-0.44
3	3	3.3	2.96	4.42	3.30	0.75
4	3	3.3	2.93	3.77	3.27	-0.80
5	3	3.3	3.27	4.28	3.44	-0.95
Average	3	3.3	3.15	4.09	3.17	-0.44
Std. Dev	0	0	0.19	0.26	0.67	0.69
Confidence interval (+/-)	0	0	0.19	0.25	0.64	0.66

### 5.7 Surface scan by the automated line scan system

3D surface maps scan results presented in this section, a 8 mm blind hole form a copper sample surface and another 8 mm blind hole from a stainless steel sample surface. 3D surface profiles generated automatically by the developed LabView GUI from the sample surfaces. In order to scan a sample surface set the image size (WOI), X – axis scan length, X and Y - axis step size, filter value, X-Y magnification calibration factor, 23.44  $\mu\text{m}$  / pixel and system calibration factor, 17.35  $\mu\text{m}$  / pixel as inputs in the LabView GUI. Scanning parameters are summarising in Table 5.11. Figure 5.32 shows 3D surface map of the copper sample surface blind hole and figure 5.33 shows 3D surface of the stainless steel surface blind hole.

Table 5.11: Line scans scanning parameters.

Parameter	Copper sample	Steel sample
X step size	50 $\mu\text{m}$	50 $\mu\text{m}$
Y step size	2 pixels	2 pixels
Scan length	11 mm	11 mm
No. of lines	220	220
WOI	64 by 512	76 by 512
No. of data points/ line	256	256
Time	7.72 minutes	8 minutes
Total data points	53760	53760
Speed	121 points / sec	112 points / sec

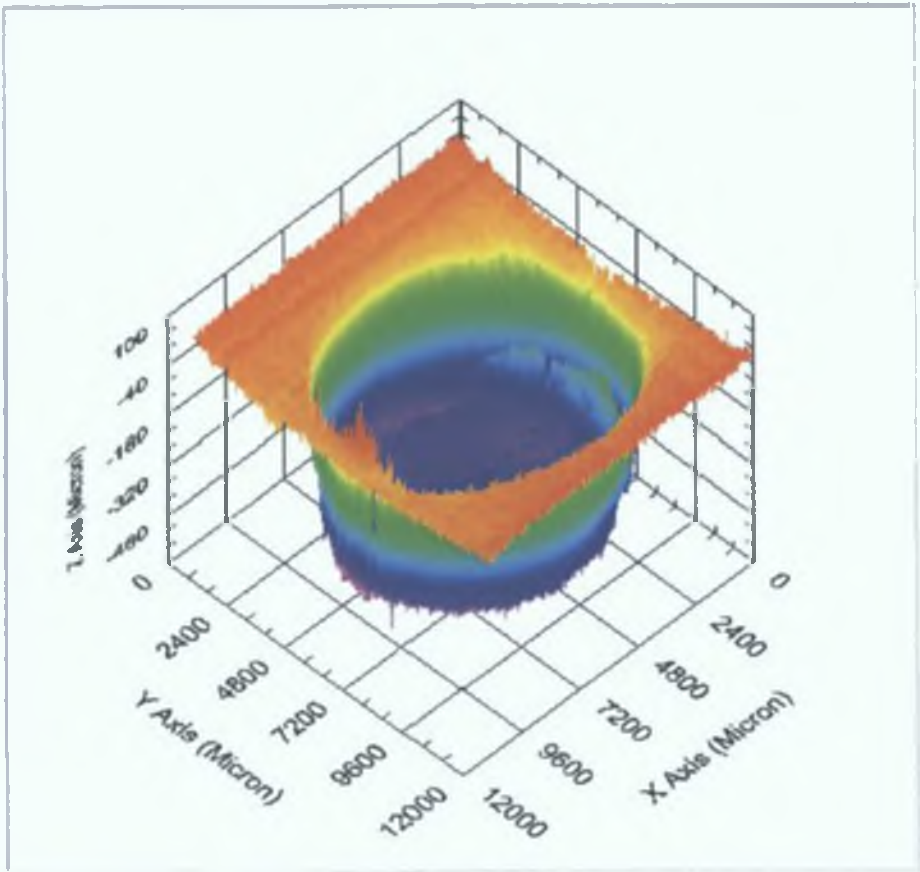


Figure 5.32: 3D surface map of the copper sample surface blind hole.

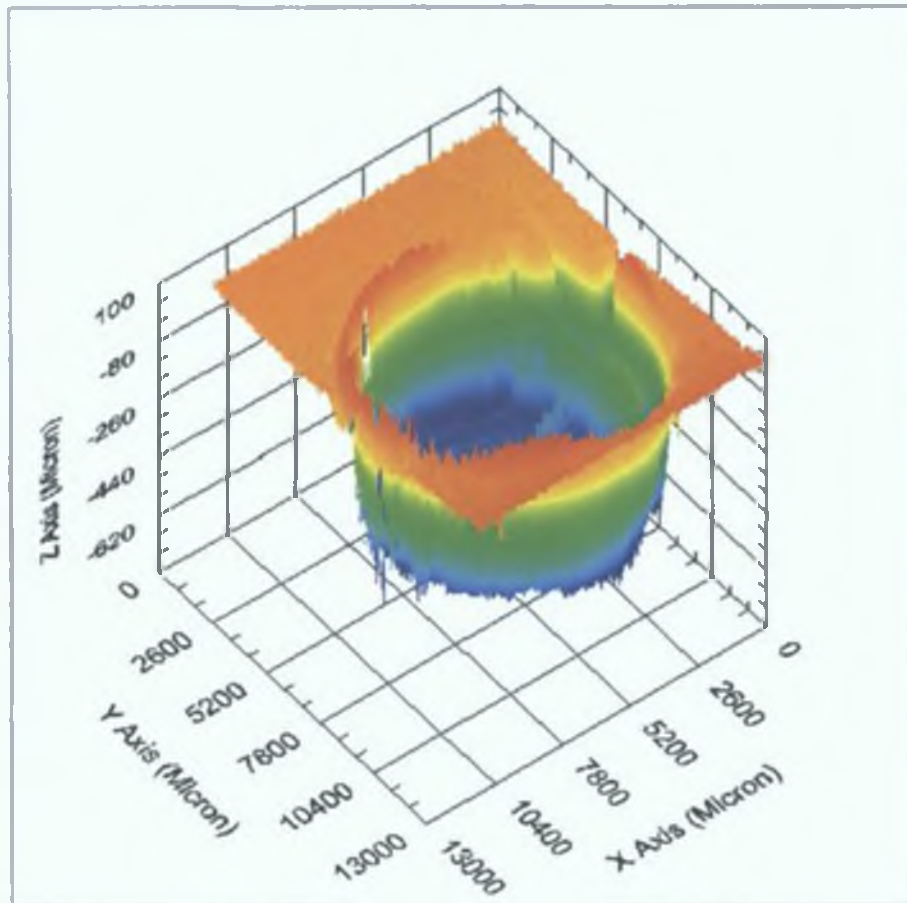


Figure 5.33: 3D surface map of the stainless steel sample surface blind hole.

# Chapter Six

## Discussion

### 6.1 Discussion

In modern manufacturing, quality control requirements are stringent and subjective. Although valuable, human visual inspection of the production process is giving way to faster, more reliable, more objective and less expensive electro-optical techniques. Among the quality control task, surface inspection is a major one. For long time, invasive stylus- based systems were widely accepted. Today the new standards and the huge variety of surfaces and materials to be inspected, often all in the same industry, require the use of versatile, non-contact system, and for this purpose optical or laser based system have clearly proved their merits [66].

There are three generally accepted application areas for inspection. These are input inspection, process inspection and output inspection. Input or receiving inspection is the examination of raw materials to determine if their quality is acceptable for use. It also involves determining if there is a sufficient amount of material for use in assembly. Process inspection is the examination of the output of an intermediate work stage; it is useful for determining if the operations at a stage were performed within specified tolerances and whether the assembly process is in control or if tools are wrong or broken. Output or product inspection is the final exhaustive inspection of a product at the end of assembly or manufacturing stages to determine the product's acceptability [67]. An automated laser based inspection system presented in this thesis could be used to inspect material surface in all of those inspection areas in any production line.

At first the system was calibrated in two different ways to obtain a depth calibration factor. In order to measure surface defect and defect size in both lateral and depth directions by the system surface scanning results were presented in the previous chapter. Surface roughness parameters measured by the LTS system were also presented in chapter five. Scans were performed on different material (copper,

stainless steel and plastic) sample surfaces with different sized (3mm, 5.9 mm and 6mm) blind hole, summary of the automated scans results are presented in Table 6.1

Table 6.1: Summary of the automated LTS scans results.

Data from	Depth ( $\mu\text{m}$ )	Diameter in the X- direction (mm)	Diameter in the Y-direction (mm)	Average diameter (mm)
Section 5.3.1	425	2.9	3.1	3.0
Section 5.3.2	500	6.3	6.4	6.35
Section 5.3.3	550	4.1	4.3	4.2

It was observed from the scanned results that the diameter of the all scanned holes are bigger at the top than at the bottom. Causes of this measurement error are discussed in the next section and a modification of the system for defect inspection with a good accuracy is proposed in future work section of this chapter.

System depth repeatability is presented in section 5.5 and results are summarized in Table 5.7 of chapter five. This Table shows that the resolution in depth direction decreases proportionally with increasing the displacement in the lateral direction.

Measured surface roughness parameter results are presented in section 5.6 of chapter five. Table 5.10 shows the results of surface roughness parameter measurement by the LTS system and by the Surftest – 402. In the present system the surface roughness parameter measurement range is restricted due to the bigger spot size. Table 5.8 and Table 5.9 show the AFM data analysis by the developed LabView GUI. It is evident that with a small spot size or a thin line it is possible to measure the Nano scale surface roughness parameters by the developed LTS system.

Automated line scan results are presented in section 5.7 of chapter five. The main intention of this section was to show that the developed LabView GUI for the line scans system working properly. Automated line scans system speed was found about 7200 points per minute whereas spot scanning speed only 30 points per minute.

### 6.2 Measurement error

Laser triangulation has been widely used in industrial measurement applications because they perform a non-contact measurement with sub-micron resolution. Moreover, it is fast and has a simple structure, good repeatability and a long operation range. However, it has various error sources such as speckle effect, variation of light intensity distribution from noise, detector noise etc. Laser based automated surface inspection system was developed on the basis of following assumptions:

- Laser beams can be collimated to provide small, diffraction limited parallel beams of light
- The intensity profile of laser beam approximately Gaussian in shape for laser spot scanning and uniform intensity distribution of laser beam for laser line scanning
- Laser line aligns properly
- Laser light produces a high contrast with the background
- Beams are highly directional and small beam divergence
- Servomotor moves its target position properly
- Image capture by the camera is done properly

An automated surface inspection system was developed, however, the accuracy of the system is not very good. System measurement errors for both depth and lateral directions are presented in Table 6.2.

Table 6.2: Error in the automated LTS scans results.

Actual diameter (mm)	Actual depth (μm)	Measured depth (μm)	Depth error (μm)	Diameter error in the X- direction (mm)	Diameter error in the Y-direction (mm)	Average diameter error (mm)
3.0	550	425	115	0.1	0.1	0.1
5.9	600	500	100	0.4	0.5	0.45
4.0	600	550	50	0.1	0.3	0.2

The accuracy of optical triangulation methods hinges on the ability to locate the centre of the laser spot. Therefore, the accuracy of sub pixel target image location is an important factor that contributes to the overall precision of the camera based inspection system. Laser spot centre position changes if the laser spot crosses a transition from high level to low-level surface or low level to high-level surface. Figure 6.1 (a) shows a laser beam transit from upper level surface to lower level surface, a part of the spot is blocked by upper level and as a result create a broken spot and other part strikes the lower level surface also create another broken spot. Figure 6.1 (b) shows a broken laser spot image due to height transition at point A and the intensity distribution of this image is shown in figure 6.2. Similar measurement error also occurs at points B and C when the laser beam transits from low level to high-level surface during scanning.

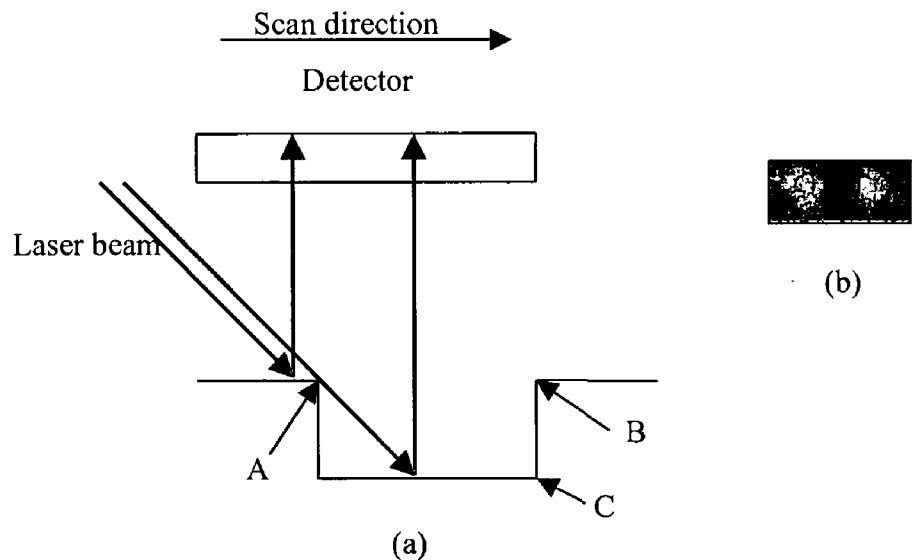


Figure 6.1: (a) Measurement error due to height transition;  
(b) Laser spot image at point A.

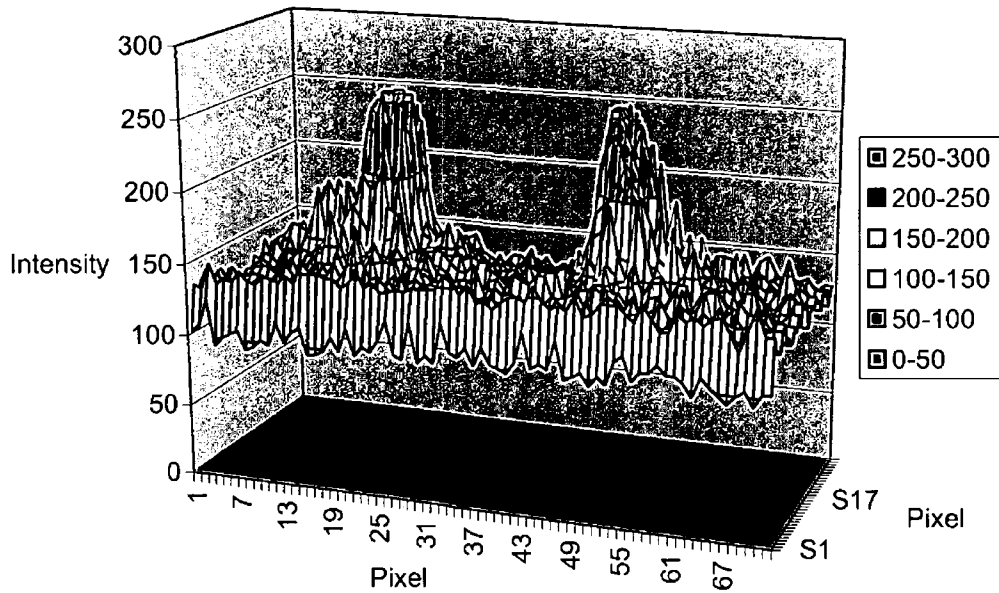


Figure 6.2: Intensity distribution of the image shown in the 6.1 figure (b).

A stainless steel sample surface was scanning from the upper to the lower level surface and scanning was repeated in same sample surface from the lower to the upper level surface. Figure 6.3 shows 3D surface map of the scan from the upper to the lower level surface of a 3.5 mm by 3 mm area with a scan step size of 25  $\mu\text{m}$ . Figure 6.4 shows 2D surface map by extracting data points from this 3D surface map along the 60<sup>th</sup> Y axis scan line, points A and B show two peaks due to the height transition measurement error.

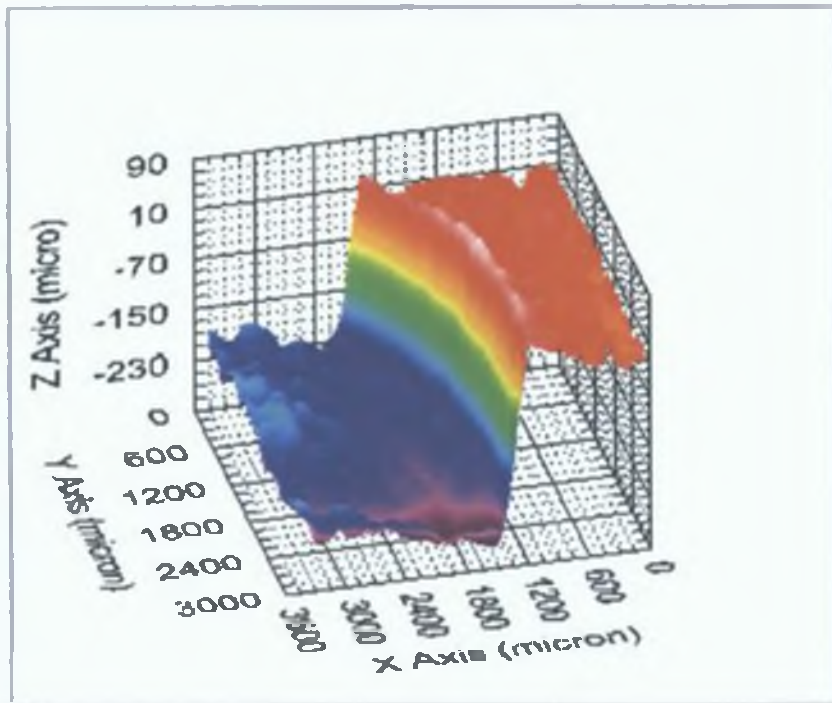


Figure 6.3: 3D surface map of a sample surface scan from the upper surface to the lower surface.

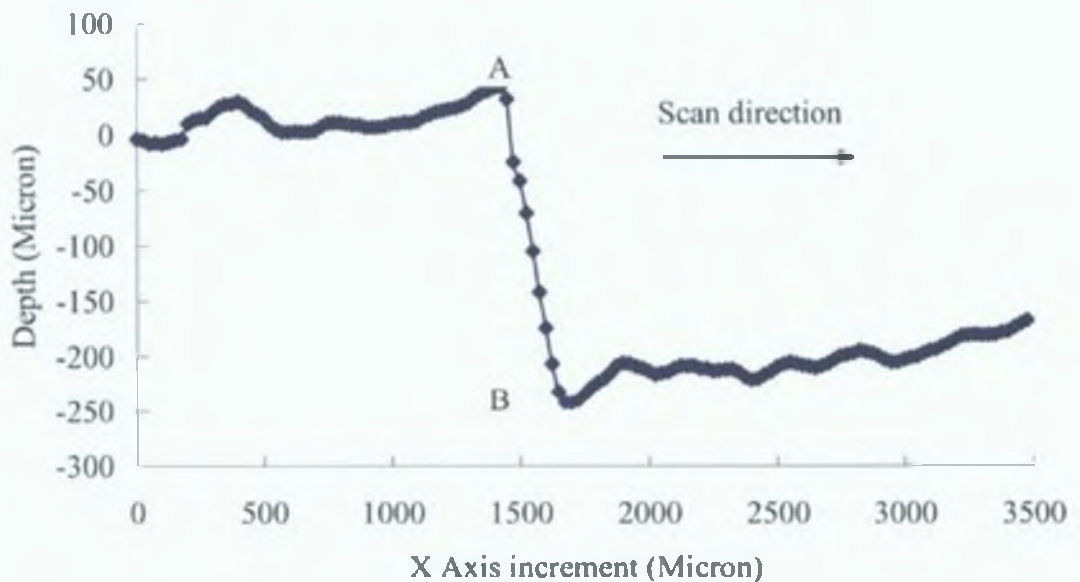


Figure 6.4: 2D profile of the surface scans from the upper surface to the lower surface.

Figure 6.5 shows 3D surface map of the stainless steel sample surface scan from the upper level to the lower level surface of a 3.5 mm by 2.5 mm area and a scan step

size of 25  $\mu\text{m}$ , and figure 6.6 shows 2D surface map by extracting data points from this 3D surface map along the 50<sup>th</sup> Y axis scan line, point A and B shows two peak due to the height transition measurement error.

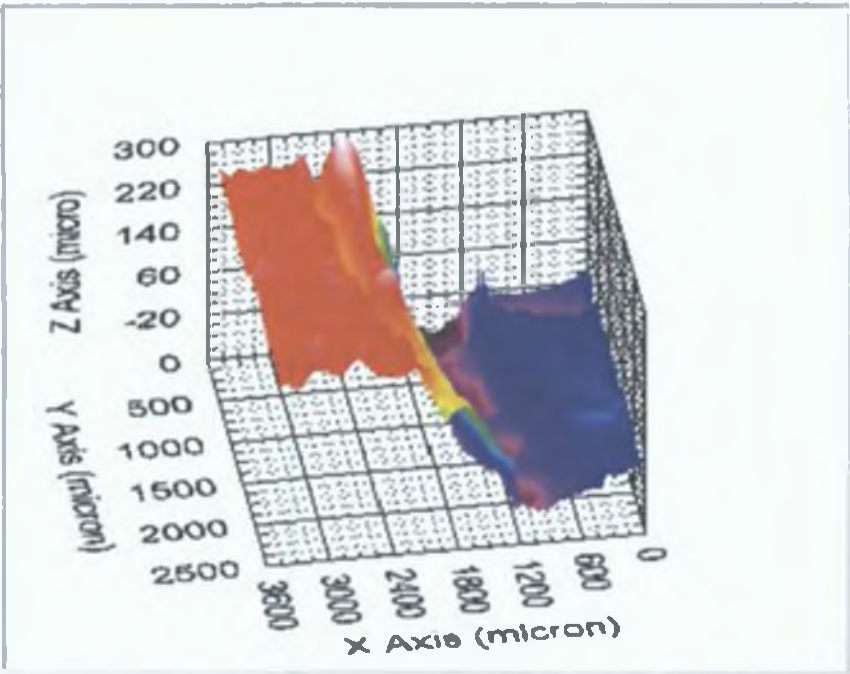


Figure 6.5: 3D surface map of the sample surface scan from the lower surface to the upper surface.

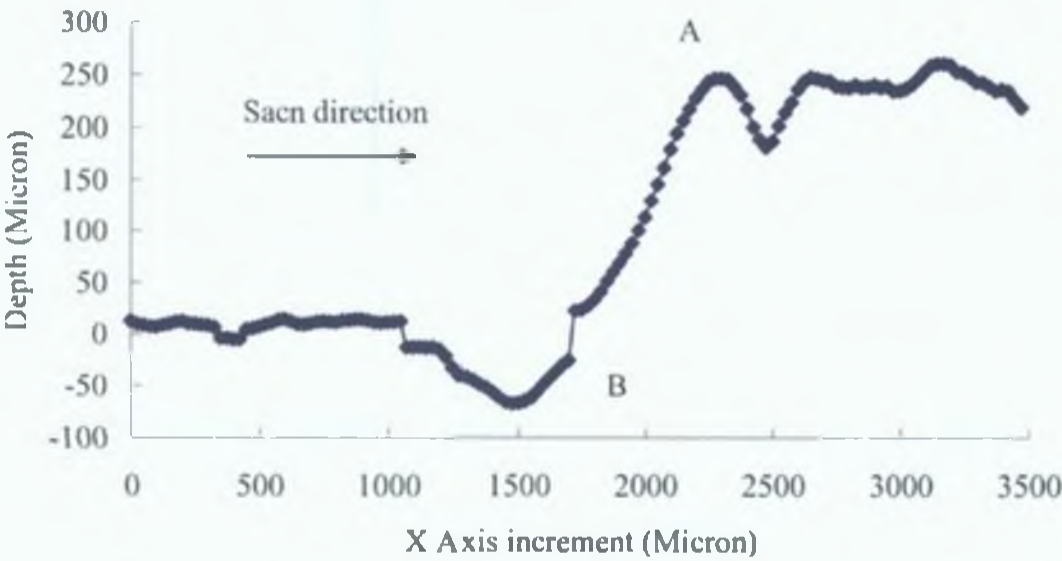


Figure 6.6: 2D profile of the surface scans from the lower surface to the upper surface.

Following two types of calibration has been done in the inspection system:

- Camera intrinsic calibration
- System calibration

Camera calibration is a process for determining the internal geometric and optical camera characteristics (intrinsic parameters). The image of the CCf15 camera may be noisy with mostly vertical noise structures due to improper camera calibration. This is Fixed Pattern Noise (FPN), typical for random addressable sensors. Therefore image quality depends of camera calibration. By the triangulation principle we measured surface height variation along Z-axis, which is directly related to this calibration factor, so accuracy of depth measurement depends on depth calibration factor. Calibration factor depends on triangulation angle, camera resolution, light source and sample position.

### **6.3 Effect of spot size on the surface profiling system**

The size of the spot is dictated by the optical design, and influences the overall system design by setting a target feature size detection limit. For instance, if the spot diameter is 50  $\mu\text{m}$  it will be difficult to resolve a lateral feature less than 50  $\mu\text{m}$ . The feature size limitation is the spatial lateral resolution, approximately equal to the spot diameter. Where the beam diameter is larger than or the same size as the feature, the sensor has sufficient resolution; where the feature is smaller than the beam diameter, the resolution is inadequate for feature detection and measurement. Spot diameter is usually specified in the center of the working range, but the limitations of physical optics dictate that it will not remain that size throughout the working range. The beam-shaping optics forms a beam. Spot size of the laser should be small because of, a) higher lateral resolution on the object; b) the image on the detector should not be too large, for better localization on the detector, i.e., for a better resolution of depth. To detect small objects the diameter of the laser beam should be as small as possible. In figure 6.7 numbers 1,2 and 3 indicate the beam diameter of the laser spot; a, b and c indicate three different objects size. In the first and second case the beam diameter is smaller than and equal to the object size, so sensor has sufficient resolution. But in

the third case the object size is smaller than the beam diameter, the resolution is inadequate for object detection and measurement.

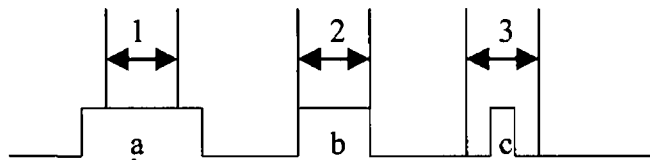


Figure 6.7: Effect of beam diameter to detect object size.

Alignment of laser beams also is a controlling factor for the spot size. As shown in figure 6.8 spot size becomes bigger if the beam is incident onto the surface at an angle  $\theta$ .  $X$  indicates a laser beam spot size when the beam is incident perpendicular to the surface and  $Y = X / \sin \theta$ , indicates the spot size when the laser beam is incident on to the surface with an angle  $\theta$ . The laser beam creates a small spot when it is incident perpendicular to the object surface.

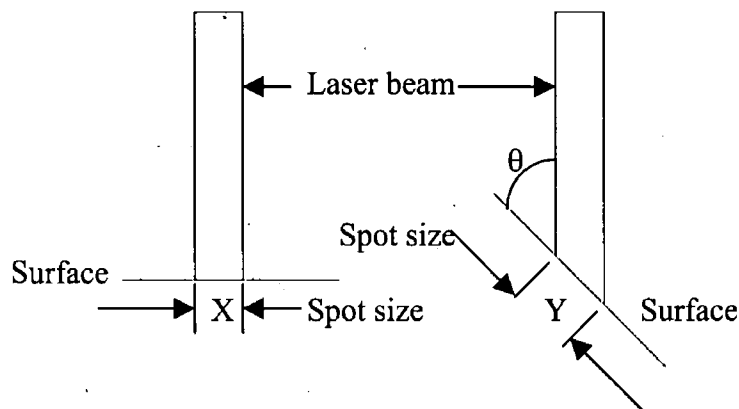


Figure 6.8: Effect of laser beam incident on spot size.

#### 6.4 System speed

The main controlling factors for the speed of the inspection system are:

- Camera image acquisition rate or frame rate
- Servomotor speed
- Data processing speed

Full frame speed of the CCf15 camera is 7 frames per second with full resolution. Camera speed depends on size of window of interest (WOI). For small WOI camera image acquisition rate become faster. Servomotor speed range is 50-425 $\mu$ m per second. System speed also depends on the PC configuration.

Table 6.3: LTS system speed.

Data from	Data points	Time (minutes)	Speed (points/min)
Section 5.3.1	2500	84	29.76
Section 5.3.2	8100	261	31.03
Section 5.3.3	3600	122	29.51
Average			30

The speed of the laser spot triangulation system is 30 points per minute that is including set WOI, image capture, motor movement, data processing and 3D reconstruction time. Automated line scanning gives excellent speed, about 7200 points per minute with a full WOI size in the Y-axis whereas spot triangulation speed 30 points per minute.

## 6.5 System resolution

System resolution depends on the system configuration such as laser spot size or line thickness, triangulation angle, depth of focus of the laser beam, camera resolution etc. Depth and lateral resolution also depends upon the incidence optics and observation optics. Developed automated surface inspection system is able to inspect a large variety of surfaces with high resolutions, down to the sub micron level. If camera viewing length, L mm by N number of pixels then depth resolution expressed by:

$$\delta z = \frac{L}{N * \tan \theta}$$

For the developed LTS system, L = 12 mm, N = 512 and  $\theta = 45^\circ$ , from the above equation system resolution:

$$\Rightarrow \delta z = \frac{12 * 1000 \mu m}{512 * \tan 45}$$

$$\Rightarrow \delta z = 23.44 \mu m$$

It is observe, the resolution of a discrete detector array can be much better than given by the pixel spacing [68]. From the table 5.1 it can be conclude that resolution much better with small focal length lens.

# Chapter Seven

## Conclusions and Recommendations

### 7.1 Conclusions

In this project a fully automated inspection system has been developed in this work. In the present system the scanning area capacity is 12 mm by 12 mm. Focal spot size of the spot generator laser is approximately 170  $\mu\text{m}$  and line thickness of the line generator laser is approximately 160  $\mu\text{m}$ . System speed using spot triangulation is 30 points per minute and for the line scan speed is 7200 points per minute. The developed automated LTS system has been successfully implemented for different material sample surface scan, and generates 2D, 3D surface profiles and surface roughness parameters measurements. Developed Graphical User Interfaces are user friendly and as such could be applicable in any production line or any inspection system without inspection experts. The resolution of the developed system for depth measurements was found to be approximately 23.44  $\mu\text{m}$  and accuracy of the system approximately  $\pm 5.753 \mu\text{m}$ , depending on the scanned area.

### 7.2 Recommendations for future work

For high speed scanning an automated line scan system has been developed, but the system has not been calibrated for the laser line. In the present system the detector is perpendicular to the camera, so camera does not lose its focal point due to the height change in the depth direction but accuracy is not very good. Improvement in accuracy would be possible

- (1) By using a small spot size laser or very thin laser line, and
- (2) By modifying the current experimental setup.

For improving the system accuracy the laser light could be perpendicular to the sample, so that the spot size will not increase due to the incident angle of laser light. If the laser light is projected perpendicular to the sample surface the detector might

lose the focal point due to the height variation in the depth direction as shown in figure 2.15. A possible way to improve the reproducibility of focusing is to use an automatic focus (auto-focus) system that maintains the detector at the focal point. The depth of focus also a problem for the laser scanning system, which could be improved by using an axicone [29, 68].

The present system is capable of creating 2D, 3D surface profiles and can measure surface roughness parameters from sample surface. For complete inspection decision-making is an essential task. For example, in the case of visual inspection during production the system decides if the produced parts meet some quality standards by matching a computed description with some known model of the image (region or object) to be recognized. The decision (e.g. model matching) may involve processing with thresholds, statistical or soft classification. The decision process for part specification acceptance could also be implemented usually with specifications being input through the GUI.

## References

- [1] Kennedy D.M., Xue Y. and E. Mihaylova, Current and future applications of surface engineering, *The Engineers Journal*, The Institution of Engineers of Ireland, Vol 59, June 2005
- [2] Curles B. L., New Methods for Surface Reconstruction from Range Images, PhD Thesis, Stanford University, USA, 1997
- [3] Yadong L and Peihua G, Free form surface inspection techniques state of the art review, *Computer-Aided Design*, Vol 36, pp 1395-1417, 2004
- [4] Abuazza A. and El Baradie M.A., Laser scanning inspection system, an overview, *AMPT 99 and IMC 16*, Volume 3, pp 1939-1945, 1999
- [5] Tognola G., Marta Parazzini, Cesare Svelto, Paolo Ravazzani and Ferdinando Grandori, A fast and reliable system for 3D surface acquisition and reconstruction, *Image and Vision Computing*, vol 21 pp 295-305, 2003
- [6] Kim C.K, Se Baek Oh, Kim S. H. and Kwak Y. K., Design of a signal-processing algorithm for error-minimized optical triangulation displacement sensors, *Measurement Science and Technology*. Vol 12 pp 1683–1688, 2001
- [7] Zhang G. and Whi H, A novel calibration approach to structured light 3D vision inspection, *Optics & Laser Technology*, Vol 34, pp 373-380, 2002
- [8] Zhou H. and Zhang G., Complete calibration of a structured light stripe vision sensor through planar target of unknown orientations, *Image and Vision Computing*, vol 23, pp 59-67, 2005
- [9] Zhao H., Liang R. Dacheng Li and Mang Cao, Practical common-path heterodyne surface profiling interferometer with automatic focusing, *Optics & Laser Technology*, Vol 33, pp 259 – 265, 2001
- [10] Kim H.Y., Y. F. Shen and J. H. Ahn, Development of a surface roughness measurement system using reflected laser beam, *Journal of Materials Processing Technology*, Vol 130–131, pp 662–667, 2003
- [11] Tay C.J., S. H. Wang, C. Quan and H. M. Shang, In situ surface roughness measurement using a laser scattering method, *Optics communications*, Vol 218 pp 1-10, 2003
- [12] Zahide Y. and Hasmi M.S.J, Surface roughness measurement using an optical system, *Journal of Materials Processing Technology*, Vol 88, pp 10 –22, 1999

- [12] Hamed A.M., El-Ghandoor H., El-Diasty F. and Saady M., Analysis of speckle images to assess surface roughness, Optics and laser technology, vol 36, pp 249-253, 2004
- [13] <http://www.predev.com/smg/intro.htm> (accessed 18 March 2005)
- [14] Zheng H., L. X. Kong and S. Nahavandi, Automatic inspection of metallic surface defects using genetic algorithms, Journal of Materials Processing Technology, Vol 125-126, pp 427-433, 2002
- [15] Tsai D.M., and Huang T.Y., Automated surface inspection for statistical textures, Image and Vision Computing, Vol 21, pp 307- 323, 2003
- [16] Abuazza A., Design And Development Of Novel Non-Contact Fibre Optic Laser Scanning System, PhD. Thesis, Dublin City University, Ireland, 2002
- [17] ASM Hand Book, Non-destructive Evaluation and Quality Control, Formerly 9<sup>th</sup> Edition, Metals Handbook, Volume 17, 1989
- [18] Luxon J.T., and Parker D.E., Industrial Lasers & Their Applications, Prentice-Hall, Englewood Cliffs, New Jersey, 1985
- [19] Wild P., Industrial Sensors and Applications for Condition Monitoring, Mechanical Engineering Publication Limited, London, 1994
- [20] <http://meltingpot.fortunecity.com/whitburn/914/inter1.htm> (accessed November 2003)
- [21] Surface Texture (Surface Roughness, Waviness, And Lay), The American Society of Mechanical Engineers, June 14,1996
- [22] Benett J.M., and Mattsson E., Introduction to Surface Roughness and Scattering, Optical society of America, Washington, DC, 1989 (Also Use in Roughness)
- [23] [http://www.allmeasure.com/Measuring\\_Devices/Form\\_\\_Size/Parameters\\_for\\_Surface\\_Roughne/parameters\\_for\\_surface\\_roughne.html](http://www.allmeasure.com/Measuring_Devices/Form__Size/Parameters_for_Surface_Roughne/parameters_for_surface_roughne.html) (accessed February 2004)
- [24] <http://www.zygo.com/library/papers/SurfText.pdf> (accessed June 2004)
- [25] [http://www.misumiamerica.com/technical/pdf/usa\\_pdf\\_tech\\_pl381.pdf](http://www.misumiamerica.com/technical/pdf/usa_pdf_tech_pl381.pdf) (accessed June 2004)
- [26] Dr. Mike S. Lou, Dr. Joseph C. Chen & Dr. Caleb M. Li, Surface Roughness Prediction Technique For CNC End-Milling, Journal of Industrial Technology, Volume 15, Number 1 – November 1998 to January 1999

- [27] <http://www.tu-dresden.de/fghgipf/forschung/material/publ2003/eI501314.pdf>  
(accessed May 2004)
- [28] Poon C.Y., and Bhushan B., 1995, Comparison of surface roughness measurements by stylus profiler, AFM and non-contact optical profiler, *Wear* Vol 190, pp 76-78, 1995
- [29] W. Dremel, G. Hausler, M. Maul, Triangulation with large dynamical range, *SPIE vol 665, Optical Techniques for industrial inspection*, pp182-187, 1986
- [30] T.A. Clarke, K.T.V. Grattan, N.E. Lindsey, Laser-based triangulation techniques in optical inspection of industrial structures, *Proc. SPIE*, 1332, pp 474 - 486, 1990
- [31] Sodhi M.S., and Tiliouine K., Surface Roughness Monitoring using computer vision, *Int. J. Mech. Tools Manufact.* Vol. 36 No. 7 pp 817-828, 1996
- [32] <http://www.geocities.com/bumbies/3d/types.htm> (accessed February 2005)
- [33] Bhuian B., Development of a Laser Based Inspection System for Surface Defect Detection, M. Engineering thesis, Dublin City University, Ireland, 2202
- [34] Rubahn H.G., *Laser applications in Surface Science & Technology*, Johan Wiley & sons, Chichester, New York. Weinheim. Brisbane. Singapore. Toronto.pp-8
- [35] Wilson J., and Hawkes J.F.B, *Optoelectronics An introduction*, second edition, Prentice Hall, New York
- [36] J.T. Luxon, D.E. Parker & P.D. Plotkowski, *Laser In Manufacturing*, IFS (Publications) Ltd., UK, 1987
- [37] Slveto O., and Hanna C.D, *Principles of Lasers*, second Edition, Plenum Press, and New York & London.
- [38] Shimoda K., *Introduction to Laser Physics*, Springer – Verlag, Berlin, Heidelberg, New York, Tokyo, 1984.
- [39] Uiga E., *Optoelectronics*, Prentice Hall, New Jersey, 1995
- [40] <http://www.columbia.edu/cu/mechanical/mrl/ntm/level2/ch02/html/l2c02s07.html>  
(accessed April 2005)
- [41] [http://tl.iam.sinica.edu.tw/support/OpticsGuide/chap02\\_Gaussian\\_Beam\\_Optics.pdf](http://tl.iam.sinica.edu.tw/support/OpticsGuide/chap02_Gaussian_Beam_Optics.pdf)  
(accessed April 2005)
- [42] <http://www.laser2000.co.uk/lasers/modules/lasdiom.htm> (accessed April 2005)

- [43] <http://www.laser2000.co.uk/lasers/modules/diagrams/diags2.htm> (accessed April 2005)
- [44] Laserex LDM-4 standard laser diode module manual
- [45] <http://www.worldstartech.com/ull5-0.4g-635.pdf> (June 2005)
- [46] [http://www.stockeryale.com/i/lasers/line\\_advantage.htm](http://www.stockeryale.com/i/lasers/line_advantage.htm) (June 2005)
- [47] William M. S., Laser material Processing, Third Edition, Springer
- [48] [http://www.a-m-c.com/what\\_is\\_a\\_servo.htm](http://www.a-m-c.com/what_is_a_servo.htm) (July 2005)
- [49] Feng H. Y., Yixin Liu and Fengfeng Xi, Analysis of digitizing errors of a laser scanning system, Precision Engineering, vol 25, pp 185-191, 2001
- [50] <http://www.scs.carleton.ca/~miles/research/threedmod/chapt2.html> (July 2005)
- [51] Chen H.H., Variation reduction in quality of an optical triangulation system employed for underwater range finding. Ocean Engineering, vol 29, pp 1871- 1893, 2002
- [52] Hariharan P., Basics of Interferometry, CSIRO Division of Applied Physics, Sydney, Australia, 1992
- [53] Hariharan P., Optical Interferometry, CSIRO Division of Applied Physics, Sydney, Australia, 1985
- [54] Steel W.H., Interferometry, CSIRO Division of Applied Physics, Sydney, Australia, 1985
- [55] Yang L.X., W. Steinchen, M. Schuth and G. Kupfer, Precision measurement and nondestructive testing by means of digital phase shifting speckle pattern and speckle pattern shearing interferometry, Measurement, vol 16, pp 149—160, 1995
- [56] Jones R., and Wyakes C., Holographic & Speckle Interferometry, A discussion of the theory, practice and application of the techniques
- [57] R.T Lopes, L.F de Oliveira, C. R Miranda, J.C. Leite, Application of X-ray scanning and tomography to evaluate the filter cake removal efficiency, Nuclear Instruments and Methods in Physics Research Section A: Accelerators, Spectrometers, Detectors and Associated Equipment.
- [58] Landis E. N., Edwin N. Nagy and Denis T. Keane, Microstructure and fracture in three dimensions, Engineering Fracture Mechanics, Vol 70, pp 911-925, 2003

- [59] Using external code in LabView (Version 7.0), National Instruments, April 2003
- [60] Costa M.F.M., and Almeida J.B., System of Optical Non-contact Microtopography, *Applied Optics*, 32, 25, pp. 4860-4863, 1993
- [61] Costa M.F.M., Surface Inspection by an Optical Triangulation Method, *Optical Engineering*, 35, 9, pp. 2743-2747, 1996
- [62] Clarke T.A., Cooper M.A.R. and Fryer J.G., An Estimator for the Random Error in Subpixel Target Location and its Use in the Bundle Adjustment, *Optical 3-D Measurements Techniques II*, Pub. Wichmann, Karlsruhe, pp. 161-168, 1993
- [63] <http://www.sensorsmag.com/articles/0598/tri0598/index.htm> (accessed May 2005)
- [64] CCAM CCf15 camera specifications manual
- [65] Thorlabs DCX - PCI 100 hardware user manual
- [66] Newman T.S. and Jain A.K., A survey of automated visual inspection, *Computer vision and image understanding*, Vol. 61, No. 2, pp 231 – 262, 1995
- [67] Malamas E.N., Euripides G. M. Petrakis, Michalis Zervakis, Laurent Petit and Jean-Didier Legat, A survey on industrial vision systems, application and tools, *Image and Vision Computing*, Vol 21, pp171 – 188, 2003
- [68] Hausler G. and Heckel W., Light section with large depth and high resolution, *Applied Optics*, Vol. 27, No. 24, pp 5165 – 5169, 1988

# Appendix A - Operation principle

Table of contents	Page
A.1 Details operation principle	106
A.2 Image spot location calculation	108
A.3 Noise thresholding	110

## List of Figures

Figure A.1	Basic principle	106
Figure A.2	Laser beam spot position in an array detector	109
Figure A.3	Setting a threshold eliminates noise and reduces distortions in the subsequent calculation of the centroid	110
Figure A.4	Thresholding is used to eliminate the secondary spot	111

# Appendix A

## A.1 Details operation principle

Intersection of the laser beam with the surface creates a bright spot at position  $X_n$ , which is the real sampled surface point.  $P_n$  corresponds to the position on the surface when the laser beam intersects with the reference level. The lateral shift of the bright spot with respect to the reference level is  $\delta_n$ . So the normal distance between the actual surface and the reference level is proportional to the lateral shift  $\delta_n$ . The intersection of a light beam with a surface creates a bright spot whose lateral position depends on the surface height [33,60,61].

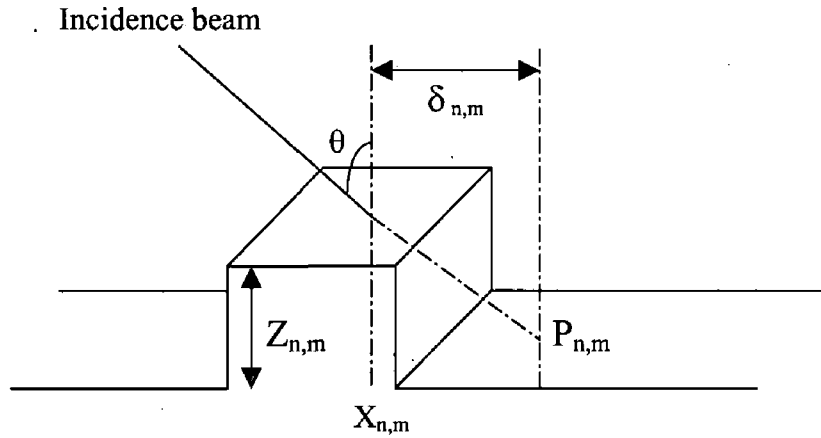


Figure A.1: Basic principle

The distance is described by the equation:

$$Z_n = \left( \frac{\delta_n}{M} \right) \cot \theta \quad \text{A.1}$$

Where,  $\theta$  is the angle of incidence of the laser.

Since in this system the laser beam was stationary, the surface was swept laterally by equal increments in the X-direction,  $\Delta$ . The lateral shift of the bright spot on the surface was observed by the sensor. Only the lateral shift of the bright spot,  $\delta_n$ , was measured and was processed later for the surface reconstruction. Figure A.1 shows

the lateral shift of the laser beam spot on the sensor. Lateral shift of the beam spot on the surface is thus determined by knowing the resolution of the sensor.

The resolution of the detector is the smallest resolvable increment of size or positional change in the object plane that can be fully detected from one pixel to the next. It is determined by dividing the field of view by the number of pixel elements in that direction. It is expressed as the amount of spacing in the object that corresponds to one pixel. For a 2-D sensor with  $N \times N$  numbers of pixels and with the field of view,  $\Delta x$ , lateral resolution of the sensor is:

$$\delta_x = \Delta x / N \quad \text{A.2}$$

and if  $q$  is the physical dimension of each pixel then magnification of the camera optical system is

$$M = q / \delta_x \quad \text{A.3}$$

from the figure 2.19 if  $p$  is the lateral shift of the beam on the detector in terms of number of pixels, then lateral shift of the beam spot on the surface is found as,

$$\delta_n = p \delta_x \quad \text{A.4}$$

Therefore,

$$\delta_n = p \left( \frac{q}{M} \right) \quad \text{A.5}$$

If  $P_o$  is the position at origin in the co-ordinate system of the surface and  $n$  the increment number in the  $X$ , then the following equations can be obtained:

$$P_o = n \Delta \quad \text{A.6}$$

Known as the sampling position.

$$X_n = n \Delta + \delta_n \quad \text{A.7}$$

Which is the  $X$  co-ordinate of the  $n^{\text{th}}$  real surface point.

Using equations A.1 and A.5, surface height at point  $X_n$  is found

$$Z_n = p \left( \frac{q}{M} \right) \cot \theta \quad \text{A.8}$$

In order to obtain a 3-D map of the surface, several profiles separated by a distance  $\Phi$  in the  $Y$ -direction were taken. Thus the co-ordinates of the inspected surface points are

$$X_{n,m} = n\Delta \pm \delta_{n,m} \quad \text{A.9}$$

Where m represents the number of increments in Y-direction.

$$Y_{n,m} = m\Phi \quad \text{A.10}$$

$$Z_{n,m} = p \left( \frac{q}{M} \right) \cot \theta \quad \text{A.11}$$

The whole system is calibrated by means of smooth reference surface, which has precise displacement along its normal. At each vertical position of the surface, the shift incurred by the bright spot is recorded, If the factor  $\left( \frac{q}{M} \right) \cot \theta$  is determined, it is possible to get the distance  $Z_n$  from equation A.8. This the conversion factor for the system. The Conversion factor is dependent on the incidence angle, on the magnification of the reception optical system and the sensor dimension.

## A.2 Image spot location calculation

In optical triangulation systems laser beam spot position on the target surface must be determined with great accuracy. The image on the array detectors provides the position of the spot on the surface to be scanned. Typically, a laser beam spot image has an approximately Gaussian shaped intensity distribution. The background influences this intensity distribution, the distance of the target from the array detector camera, and the angle of inclination of the target to the camera. Variations influence the accuracy with which the detected image can be located. A number of algorithms can be used to compute the locations of these target images to sub pixel precision, for example, centroid methods and least squares template matching. The least squares method, which is computationally expensive, is able to indicate the “goodness of fit” between the target and an ideal template. Centroid methods, which are simple to calculate, do not provide such information.

One of the most common, and intuitively acceptable definitions of the centre of the target image is the position of its centroid. The position can be defined by co-ordinates relative to an arbitrary origin and arbitrary axes, but for convenience with a corner and edges of the two dimensional array of pixels. To define the position of the centroid of a target image within the array, it is convenient to take a rectangular shaped subset of pixels (or window), which encloses the target image. Then a local

co-ordinate system with origin at a corner of the window and orthogonal axes parallel to its sides is convenient as a basis for calculating the position of the centroid of the target image. Figure A.2 illustrates the arrangement. The window has  $m$  pixels in the  $x$  direction and  $n$  in the  $y$  direction.

If, for pixel  $(i, j)$  in the window the intensity level is  $I_{ij}$ , then the co-ordinates of the centroid are, if the factor at each pixel is taken to be proportional to the intensity level  $I_{ij}$ :

$$X = \frac{\sum_{j=1}^n \sum_{i=1}^m j \cdot I_{ij}}{\sum_{j=1}^n \sum_{i=1}^m I_{ij}} \quad \text{and} \quad Y = \frac{\sum_{j=1}^n \sum_{i=1}^m i \cdot I_{ij}}{\sum_{j=1}^n \sum_{i=1}^m I_{ij}} \quad \text{A.12}$$

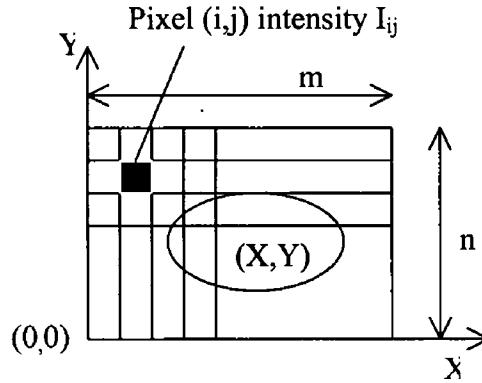


Figure A.2: Laser beam spot position in an array detector [33,62]

The co-ordinates  $(X, Y)$  in equation A.12 are relative to the array of pixels and defines the centroid in the image co-ordinate system. This equation yields the centroid of the spot position in pixels and allows the triangulation system to determine the location of the center of the spot to a fraction of pixel.

Another centroid definition investigated an algorithm to determine the centroid of the spot image where the intensity values are squared. This has the effect of giving more weight to the higher intensity levels which, are more precisely measured and, in a real image, less affected by background intensity variations. This centroid could not be expected to be correct when a small image covering a few pixels is used, because under these circumstances the calculated center will be incorrectly biased toward the highest intensity level, rather than to the center of a group of high intensity levels [33,62]. The centroid co-ordinates are given by:

$$X = \frac{\sum_{j=1}^n \sum_{i=1}^m j \cdot I^2_{ij}}{\sum_{j=1}^n \sum_{i=1}^m I^2_{ij}} \quad \text{and} \quad Y = \frac{\sum_{j=1}^n \sum_{i=1}^m i \cdot I^2_{ij}}{\sum_{j=1}^n \sum_{i=1}^m I^2_{ij}} \quad \text{A.13}$$

### A.3 Noise thresholding

Thresholding is a technique used to selectively discard unwanted information. In the simplest case, thresholding can be used to filter out spurious reflections and noise in the sensor system. Important sources of noises are the external illumination, laser speckle, laser focusing, laser power, object reflectivity, electromagnetic interference, signal quantization etc. Some of the sources of noise have a multiplicative effect on the signal others have additive effect. By thresholding some of the noise can be removed. In the figure A.3, the small intensity values in the pixels that are not part of the real spot will slightly shift the spot's calculated centroid. The horizontal line in the figure indicates where the threshold could be set to counteract the effect of noise.

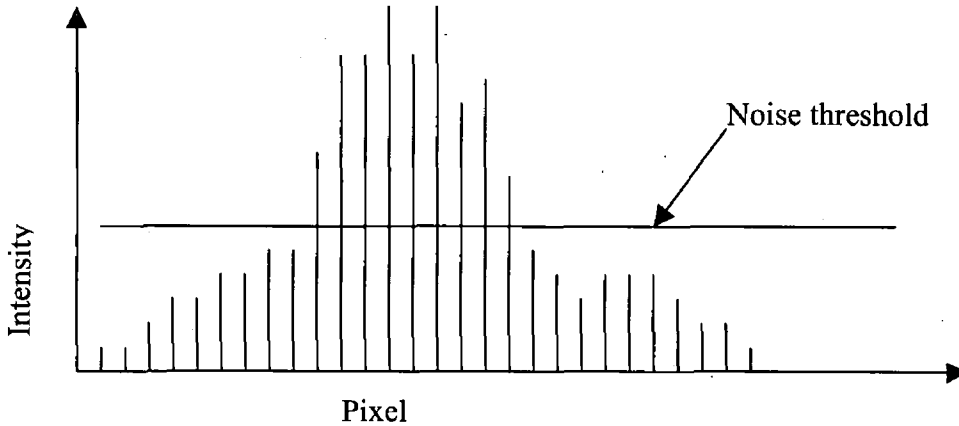


Figure A.3: Setting a threshold eliminates noise and reduces distortions in the subsequent calculation of the centroid

By setting the threshold above the noise, all pixel values equal to or less than the threshold value are set to zero before calculating the centroid. This removes most of the optical and electronic noise from the image, ensuing that the resulting centroid calculation will not be biased [33,63].

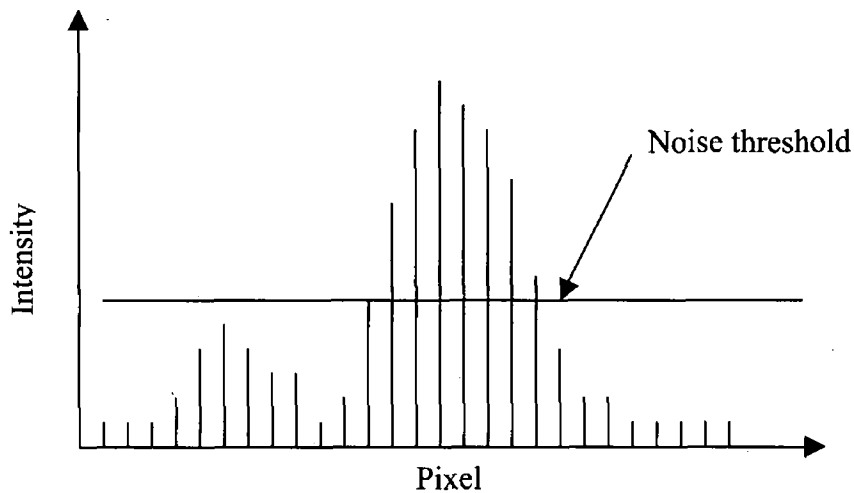


Figure A.4: Thresholding is used to eliminate the secondary spot

Another application of thresholding is the suppression of secondary images. Figure A.4 is typical of a transparent glass or plastic component where the laser reflects not only from the top (first surface), but also from the underside of the material (second surface). There are two distinctly different spots separated by the thickness of the material. One spot has an amplitude greater than the other's because the amount of reflected light is greater from the first surface than the second surface.

To determine the distance to the first surface, thresholding can be used to suppress the secondary spot; the result is that the centroid calculation is performed on the largest spot [63].

# Appendix B - Properties of laser light

Table of contents		Page
B.1	Unique properties of laser light	113
B.1.1	Monochromaticity	113
B.1.2	Coherence	113
B.1.3	Directionality	115
B.1.4	Brightness	115
B.2	Types of lasers	116
B.3	Laser mode	117

## List of Figures

Figure B.1	Temporal change of the electromagnetic field strength $E$ for thermal light source (a) and a laser (b)	114
Figure B.2	Operating modes of lasers	117
Figure B.4	Gaussian intensity distribution for TEM <sub>00</sub> mode	118
Figure B.3	Various mode patterns	118

# Appendix B

## B.1 Unique properties of laser light

In this section the properties of lasers light, which make lasers such useful tools in an incredible variety of application are discuss [36]. Laser radiation is characterize by extremely high degree of [37]:

1. Monochromaticity
2. Coherence
3. Directionality
4. Brightness

### B.1.1 Monochromaticity

The term monochromatic literally means single colour or single wavelength. However, no light source (or any electromagnetic source for that matter) is perfectly monochromatic. Lasers tend to be relatively monochromatic. However, this depends on the types of laser, and special techniques can be used to improve monochromaticity to one part in  $10^8$  for standard commercial systems for interferometric measurement applications or much better in science lasers for seismographic work or frequency standardisation. Monochromatic output, or high frequency stability, is of great importance for lasers being used on interferometric measurements since the wavelength is the measure of length or distance and must be known with extreme precision [36].

### B.1.2 Coherence

The concept of coherence is one of considerable interest in a wide variety of laser applications such as communications, holography, Doppler velocimetry and interferometric measurements. Lasers provide a high radiance source of light with a high degree of coherence. This combination is not available from any other source of light [36]. Lasers are source of Temporal and Spatial Coherent light. Compared with the light generated by a thermal lamp laser light is especially suited for applications

in surface and materials science due to its coherence, intensity and due to the possibility to generate short and ultrashort pulses.

Two partial waves of a light source are called coherent if their phase differences are constant, which leads, upon superposition, to interference phenomena. Temporal coherence is equivalent to the amplitudes of the emitted electromagnetic wave remaining constant over a considerably long time. This is demonstrated in figure B.1 by comparison of the temporal evolution of the electric field amplitude emitted from a laser source and that emitted from a thermal light source.

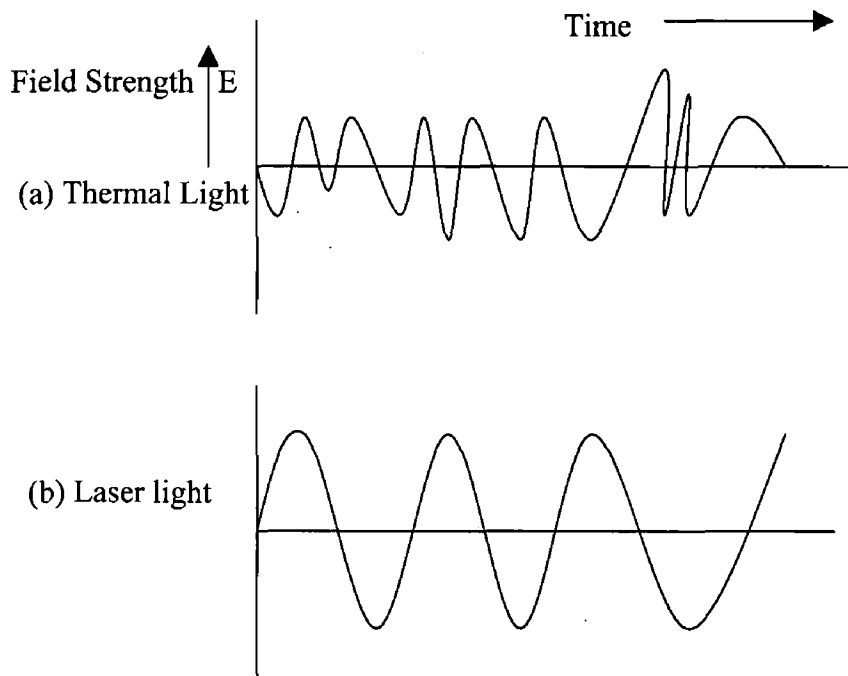


Figure B.1: Temporal change of the electromagnetic field strength  $E$  for thermal light source (a) and a laser (b) [34]

The 'coherence length'  $L_c$  is defined as the difference in optical length that results in a phase difference between two partial waves smaller than  $\pi$ , hence that difference that allows interferences to occur. The corresponding 'coherence time'  $\tau_c = L_c / c$  is related to the coherence length via the speed of light,  $c$ , in the investigate medium.

High temporal coherence results in light that is strongly monochromatic. However, strongly monochromatic light is not necessarily highly temporally coherent since the photon statistics of light from a lamp and that from a laser are fundamentally different

### **B.1.3 Directionality**

Perhaps the most arresting property of laser light is its directionality. Apart from semiconductor junction lasers, lasers emit radiation in a highly directional, collimated beam with a low angle of divergence. This is important because it means that the energy carried by the laser beam can be collected easily and focused onto a small area. For conventional sources, where the radiation spreads out into a solid angle of  $4\pi$  sr, efficient collection is almost impossible even at large distances from the laser [35]. The directionality of the beam is expressed by the angular broadening  $\delta\theta$ , which is related to the beam diameter,  $d$ , at the exit of the laser and its wavelength  $\lambda$  by the equation

$$\delta\theta \simeq \frac{\lambda}{d} \quad \text{B.1}$$

The distribution of field intensity within the cross-section of the laser beam and the angular distribution at large distances are related by a Fourier transform as is well known theory of diffraction. Equation B.1 is an approximate expression for the angle of directionality for a relatively smooth intensity distribution [38].

### **B.1.4 Brightness**

The primary characteristic of laser radiation is that lasers have a higher brightness than any other light source. We define brightness as the power emitted per unit area per unit solid angle. The relevant solid angle is that defined by the cone into which the beam spreads. Hence, as lasers can produce high levels of power in well-collimated beams, they represent sources of great brightness. High brightness is essential for the delivery of high power per unit area to a target; this in turn depends on the size of the spot to which the beam can be focused [35].

Other properties of laser light are:

- Its speed is the highest speed possible.
- In a vacuum travels in a straight line
- It can carry information.
- It can be readily manipulated by mirrors and can be switched on and off quickly.
- It can apply energy to very small areas.
- When pulsed it offers the possibility of power multiplication by releasing energy in very brief pulses.

Directionality may be seen as the most important of the above laser properties to obtain an accurate scanning system [15]

## **B.2 Types of lasers**

In the thirty years since Maiman reported the first observation of successful laser action in ruby, there has been an extremely rapid increase in the types of lasers and in the range of materials in which lasing has been shown to occur [35]. Lasers can be classified according to the lasing medium and pumping methods.

The first determines the laser wavelength, and the later, output power and operating mode. Lasers can be operated in three modes as shown in figure. Figure B.2 (a) shows CW or continuous wave operation.

Pulsed mode output is achieved by pulsed pumping schemes. Depending on the pumping methods, repetition rates from hertz to kilohertz may be achieved with relatively high bursts of output power.

Q-switched output produces pulses with very short duration, in picosecond or nanosecond range, with peak power in the kilowatt or megawatt range. Q-switching is accomplished by introducing into the resonance cavity a device that lowers its Q and thus damps oscillation and prevents stimulated emission. As a result, an excess of electron overpopulation in lasing band is produced. When the oscillating inhibiting mechanism suddenly is removed, a very strong, short duration burst of radiation is generated [39].

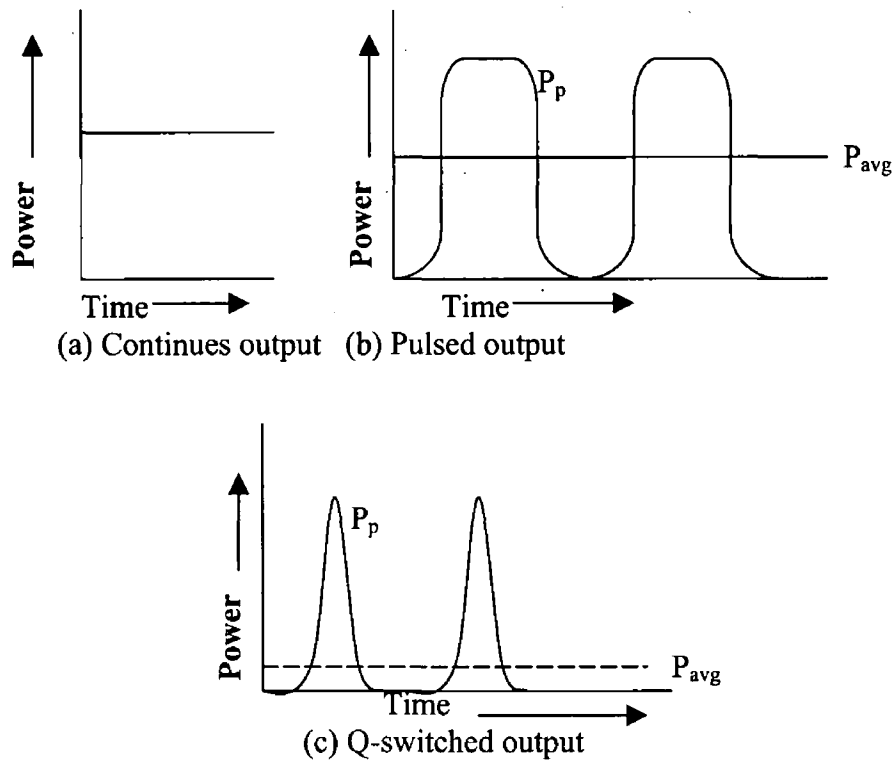


Figure B.2: Operating modes of lasers

Lasers also have the following classification according to their lasing medium.

1. Solid state lasers
2. Gas lasers
  - a. Atomic gas lasers
  - b. Molecular gas lasers
3. Dye lasers
4. Semiconductor lasers

### B.3 Laser mode

Modes are the standing oscillating electromagnetic waves, which are defined by the cavity geometry. Laser works in the longitudinal and transverse mode. When longitudinal modes oscillate, they interfere with each other, forming the transverse standing wave pattern on any transverse intersection plane. This mechanism decides the Transverse Electromagnetic Modes (TEM) of the laser beam, which is the wave

pattern on the output aperture plane.  $TEM_{pq}$  to specify a TEM mode, where  $p$  is the number of radial zero fields,  $q$  is the number of angular zero fields,  $q$  is the number of longitudinal fields, and usually use  $TEM_{pq}$  to specify a TEM mode, without the third index. Various TEM mode patterns is shown figure B.3. Clearly, the mode pattern affects the distribution of the output beam energy, which will thus affect the machining process [40]. Intensity distribution of TEM00 mode laser is shown in figure B.4.

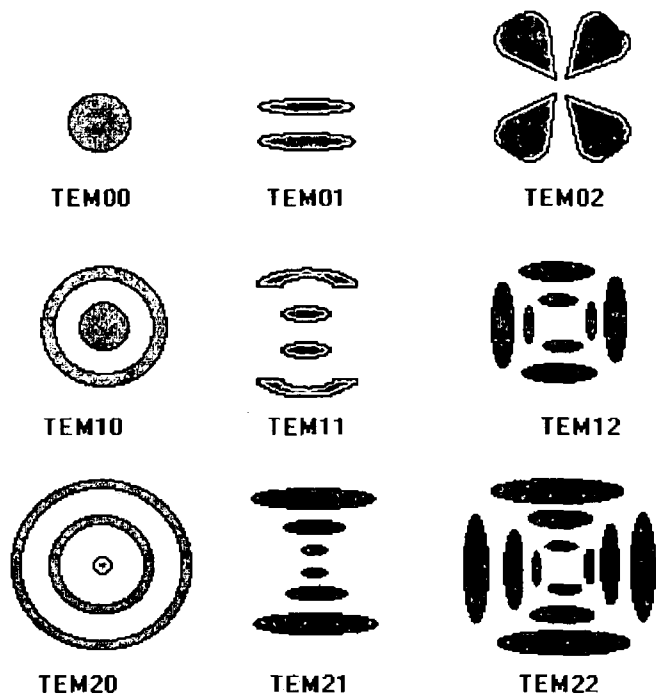


Figure B.3: Various mode patterns [40]

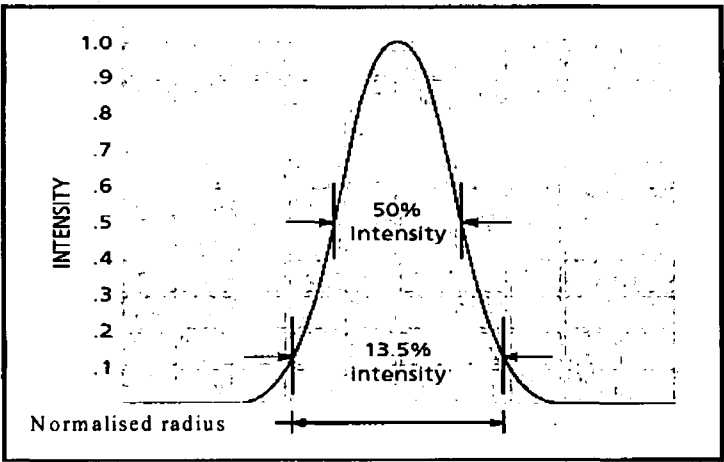


Figure B.4: Gaussian intensity distribution for TEM00 mode [41]

# Appendix C – Laser diodes modules specifications

Table of Contents	Page
C.1 Thorlabs CPS186 specifications	120
C.2 Laserex laser line specifications	121

# Appendix C

## Laser diode module

### C.1 Thorlabs CPS186 specifications

#### Collimator Pen

CPS186

##### Description

Type number: CPS186  
Date of first issue: Aug-28-98  
Date of change: Sep-01-98

##### Properties

Housing: Aluminum  
Lens: Glass  
Type of laser: N-type

##### Features

Operating temperature: -10 to 60 °C  
Storage temperature: -40 to 85 °C  
Application: Test & Measurement  
Alignment

##### Operational Hazard: Semiconductor Laser Diode

This laser pen emits radiation that is visible to the human eye. When use, do not look directly into the device. Direct viewing of laser diode emission at close range may cause eye damage, especially in conjunction with collimating lenses. Extreme care must be taken to prevent the laser from being viewed directly or through external optics or mirrors.



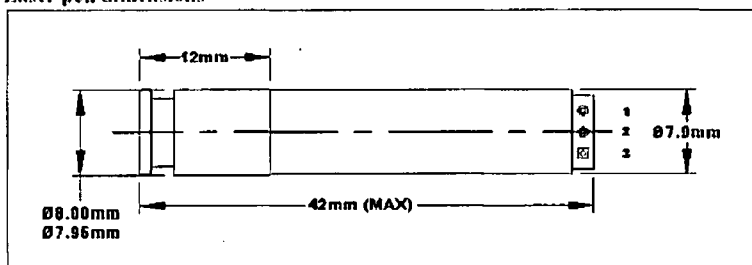
This product conforms to all applicable standards of FDA regulation (DHHS, 21 CFR subchapter J). In combination with a power supply laser module falls within Safety Class 3B. Due to the small size of the devices, the required warning is affixed to the box containing the laser modules.

##### Quick reference data

Tcase=(25 ± 2) °C Po=4.0 mW, unless otherwise specified

Symbol	Parameter	Conditions	Min	Typ	Max	unit
$\lambda$	Wavelength			670	680	nm
Po	Optical output power	100mm from pen	4.0		4.5	mW
DLx	Beam diameter perpendicular x	FWHM at pen		4.4		mm
d//	parallel to the laser stripe	exit		1.2		mm
$\theta_{Lx}$	Beam divergence	Including natural			0.6	mrad
$\theta_{//}$		divergence			1.8	mrad
$\sigma_{om}$	Optical-mechanical axis deviation			7	15	mrad
dca	Clear aperture			4.4		mm
Iop	Operating current laser pen			55		mA
Vop	Operating voltage	With reference to ground	-4.5	-5	-5.5	V

##### Laser pen dimensions




Dimensions in mm (unless otherwise stated)

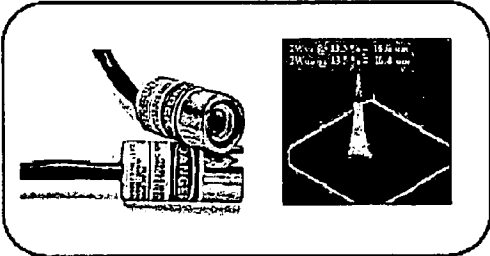
##### Pinning

- 1 = -5V
- 2 = Not connected
- 3 = Ground

C.2 Laserex laser line specifications

LDM-4 Standard Module





Features

- Compact size (11mm dia. x 25mm long)
- Slow start, reverse polarity and over voltage protection
- Small focal spots down to 10 microns
- Available with range of line generators both Gaussian and Uniform Intensity
- Cost effective

Available Wavelengths & Powers	Wavelength (nm)	Power (mW)
	635nm	0.5 - 25mW
	650nm	0.5 - 40mW
	670nm	0.5 - 8mW
	780nm	1 - 50mW
	808nm	1 - 400mW (requires external driver)
	830nm	5 - 40mW
	840nm	0.5 - 8mW
	850nm	0.5 - 8mW
	905nm	10 - 25mW
Beam Size at output	Apertured	3mm x 2mm
	Non-aperture - Glass	6mm x 2mm
	Non-apertured - Plastic	5mm x 2mm
Typical Achievable focal spot sizes (1/e <sup>2</sup> ) (spot circularity of measurements (0.95 typical))	Focus Distance (mm)	Spot Size (um)
		Apertured / Non-apertured
	25	15 / 18
	50	27 / 34
	75	42 / 58
	150	85 / 115
Typical Achievable Line Thicknesses (1/e <sup>2</sup> ) (when used with one of our line generators)	Focus Distance (mm)	Line Thickness (um)
	25	12
	50	25
	75	40
	150	80
	200	110
Beam Divergence	0.75 mrad	
Mechanical / Optical Alignment	Standard Fixed Focus	< +/- 10mm @ 3m
	Special Fixed Focus	< +/- 5mm @ 3m

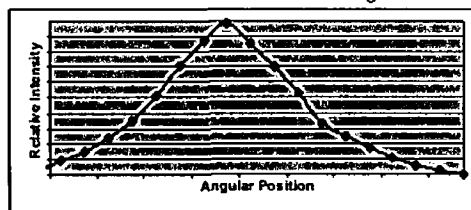
This product is registered with the FDA in accordance with 21 CFR 1040.10(a)(3)(II) and is compliant with European, and Australia/New Zealand laser safety standards 73/23/EEC - 98/37/EG, 89/336/EEC, EN 50081-1, EN-31252, EN-31252, EN 55022, EN 60825-1 and AS/NZS 2211:1997. The complete laser product manufacturer must supply adequate instructions for installation and servicing of this product. This is not a removable laser system. This product is designed solely as a component in an electronic product and therefore does not comply with the requirements of 21 CFR 1040.10 and 1040.11 for complete laser products. Avoid direct eye exposure to the beam.

# LDM-4 Standard Module

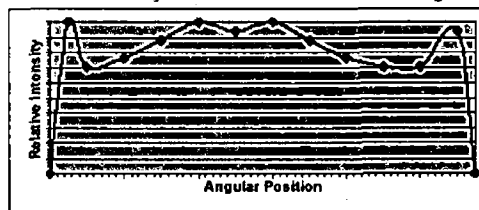
# Laserex

Physical Dimensions	11mm diameter x 25.4mm	
Operating Voltage	3 - 6 VDC	
Typical Operating Current	Laser Power (mW)	Current (mA)
	1-4	<45
	5-8	<80
	15-50	<120mA
Power Stability (25deg.C)	2hr. <1%	
Beam Pointing Stability	<50urad	
Spectral Linewidth	<0.5nm typical	
External TTL Modulation	Standard LDM-4	With Pulsing Option
	1kHz	500kHz

Gaussian Line Generator Profile 60 degrees



Uniform Intensity Line Generator Profile 60 degrees



Standard Gaussian Line Generator Options

Part Number	Line Generator Fan Angle
L5	5 degrees
L8	8 degrees
L15	15 degrees
L40	40 degrees
L45	45 degrees
L60	60 degrees
L70	70 degrees
L90	90 degrees

Standard Uniform Intensity Line Generators

Part Number	Line Generator Fan Angle
UL60	60 degrees
UL90	90 degrees

Determining Laser Specifications from part number

LDM - [ ] - [ ] - [ ] - [ ] - [ ]					
MODULE	WAVELENGTH	POWER	LENS	FOCUS	OPTIC
1 = Micro	635 = 635nm	1 = 1mW	P = Plastic	F100 = 100mm	L5 = Line 5°
2 = X-Y Adjustable	650 = 650nm	3 = 3mW	G = Glass	F350 = 350mm	L10 = Line 10°
3 = Sealed	..	..	..	..	..
4 = Standard	950 = 950nm	50 = 50mW	GA = Glass Apertured	none = Collimated	CH = Cross Hair
5 = Low Divergence	..	..	..	..	..

This product is registered with the FDA in accordance with 21 CFR 1040.10(a)(3)(i) and is compliant with European, and Australia/New Zealand laser safety standards 73/23/EEC - 98/37/EG, 89/336/EEC, EN 50081-1, EN-31252, EN-31252, EN 55022, EN 60825-1 and AS/NZS 2211:1997. The complete laser product manufacturer must supply adequate instructions for installation and servicing of this product. This is not a removable laser system. This product is designed solely as a component in an electronic product and therefore does not comply with the requirements of 21 CFR 1040.10 and 1040.11 for complete laser products. Avoid direct eye exposure to the beam.

# Appendix D – Camera specifications

Table of Contents	Page
D.1 CMOS camera specifications	124
D.2 Camera frame speed	126
List of Table	
Table D.1 Camera frame speed in different WOI	126

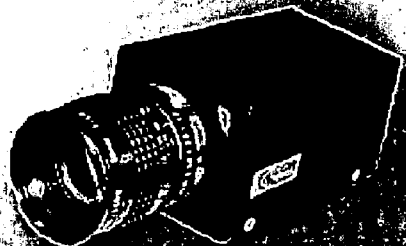
# Appendix D

## D.1 CMOS camera specifications



### CCf<sub>15</sub> CMOS Camera

CCf<sub>15</sub> CMOS Camera



- IMEC designed Fuga 15d CMOS sensor
- 512 x 512 pixels
- Monochrome
- 8-bit digital output
- Dynamic Range of 120 dB
- LVDS communication
- Works with PCI-LVDS interface or third-party frame grabbers

The CCf<sub>15</sub> camera is one of a series of highly integrated CMOS sensor-based cameras. The camera is equipped with the Fuga15d CMOS image sensor designed by FillFactory 512 x 512 pixels (12.5  $\mu$ m square).

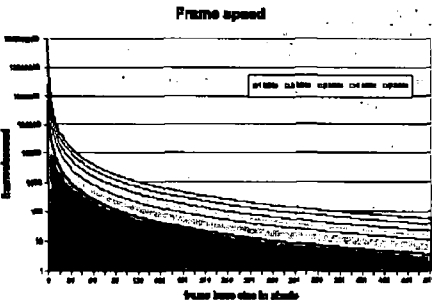
Random access to pixels makes it possible to achieve very high frame rates if the Window Of Interest (WOI) is limited. This makes it an ideal camera for spot tracking applications. The logarithmic response of the sensor results in an extended dynamic range of 120 dB (6 decades

of light). This sensor is specially designed for very high light levels.

C-Cam Technologies supply the standard PCI-LVDS card as interface. Alternatively, any compatible digital frame grabber equipped with bi-directional LVDS interface technology can be used, but then an external power supply is required. The camera supports cables up to 10 meters long.

The software in the CCf<sub>15</sub> camera provides flexibility and can be altered to the customer's specific requirements, e.g. special trigger timing for use with lasers. Additional memory can be used for storing the image and/or performing DSP-like operations.

The CCf<sub>15</sub> camera provides a complete solution for system designers who require a rapid solution with little or no involvement at the chip level.



# CCf<sub>15</sub> CMOS Camera

CCf<sub>15</sub> CMOS Camera

<b>Sensor Specifications</b>		<b>Mechanical Specifications</b>	
Imager Type	CMOS integrating active pixel sensor (APS) Fuga15d designed by IMEC - FillFactory	Dimensions	Approx. 115 x 60 x 50 mm (not including lens)
Sensor Types	Fuga15d Monochrome	Weight	Approx. 450 grams (not including lens)
Total Pixels	262,144 (512H x 512V)	Housing	Aluminum
Total Light-Sensitive Pixels	262,144 (512H x 512V)	Lens Adapter	C-mount standard black anodised
Window of Interest (WOI)	Any rectangle or line Image format and even single pixels can be specified by the user	Microscope Adapter	1.25 Inch Push-Fit adapter black anodised (optional)
Active Image Area	6.4 mm (H) x 6.4 mm (V)	Tripod mount	1/4 inch mount (1 off)
Pixel Pitch	12.5 x 12.5 µm	Machine mount	M6 x 1 (2 off)
Fill Factor	15 %	<b>Environmental Requirements</b>	
Spectral Response	More than 30 %	Operating temperature	0°C to +50°C
Blooming	Non-existent	Storage temperature	-30°C to +80°C in non-condensing conditions
Smear	from 8 mW/cm <sup>2</sup>	<b>Power Requirements</b>	
Standard Dynamic Range	120 dB	Power supply voltage	from PC through SCSI cable when used with standard I/O PCI/LVDS Interface
Grey Level Resolution	8 bits or 256 grey levels		8 - 12 Volts DC only if used with third-party digital frame grabbers
MTF	0.35 @ Nyquist with 500 nm light	<b>Ordering Information</b>	
Response Time	4 ms @ 0.04 W/cm <sup>2</sup> and 400 µs @ 0.4 W/cm <sup>2</sup> (650 nm)	Monochrome	CCF15-30-M
<b>Image Specifications</b>		Memory expansion (option)	Contact C-Cam
Pixel Rate	Approx. 3.7 MHz (typical)	<b>Interface Specifications</b>	
Frame Speed Full Resolution	Approx. 14 frames/second (raw speed)	Interface Type	Digital LVDS (Texas Instruments) bi-directional (LVDM)
Frame Speed WOI	Depending on frame size and selected readout speed (extreme high)	Remote Control	Via Digital LVDS interface
Exposure time	Not applicable for this kind of sensor	Interface connector	SCSI 50 pins connector
Shutter	Not applicable for this kind of sensor	Cable Lengths	1, 3, 5 or 10 meters from camera to PC Interface

C-Cam Technologies  
division of **vector**  
Interleuvenlaan 46,  
B-3001 Leuven, Belgium

Tel. : +32 (0)16 40 20 16  
Fax : +32 (0)16 40 03 23  
[www.vector-international.be](http://www.vector-international.be)  
[info@vector-international.be](mailto:info@vector-international.be)

## D.2 Camera frame speed

Table D.1: Camera frame speed in different WOI

WOI	Time (Sec)	No. of image	Frame speed / sec
512 by 512	92.608	352	7
300 by 300	69.213	725	11
100 by 100	27.205	1054	39
52 by 50	24.657	2401	97
68 by 30	22.804	2271	99

# Appendix E – Motion Control Hardware's

Table of Contents	Page
E.1 DCX-PCI100 motion control motherboard specifications	128
E.2 MC110 motion control modules specifications	128
E.3 Actuator Specifications	129

## List of Figures

Figure E.1	DCX-PCI100 Motion Control Motherboard	128
Figure E.2	DCX – MC110 Motion Control Modules	129
Figure E.3	Motorized Actuator	130
Figure E.4	Mechanical drawing of Thorlabs Z612B 12mm Motorized Actuator	130

# Appendix E

## E.1 DCX-PCI100 motion control motherboard specifications

1. 1 to 8 axes of DC servo controller with no external amplifiers
2. Independent point-to-point position or velocity control of all 8 axes
3. Full support for Windows XP/2000/NT/ME/98
4. On-board multi-tasking of up to 10 independent user programs frees host PC for other tasks
5. Fully programmable in C/C++/Visual Basic/Delphi & LabView

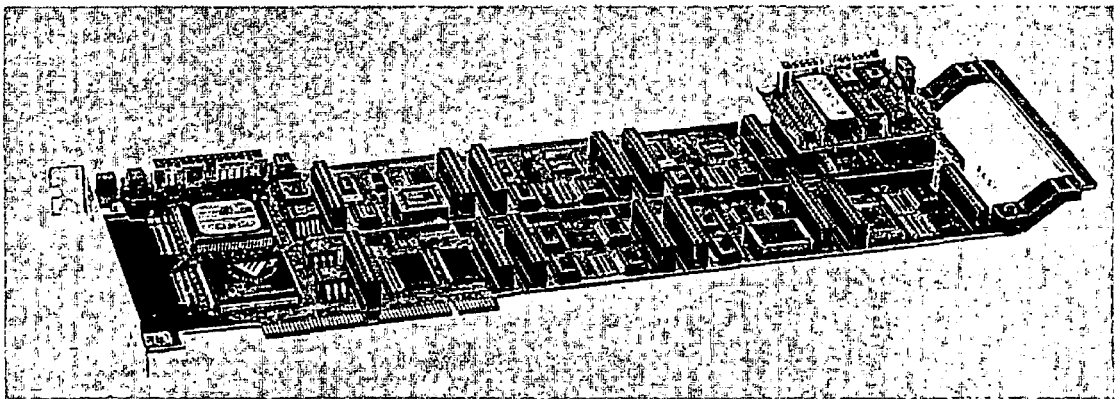


Figure E.1: DCX-PCI100 Motion Control Motherboard

## E.2 MC110 motion control modules specifications

1. Operating Modes: Position; Velocity
2. Control Filter: 3.3KHz PID; 32 bit precision
3. Velocity Profiles: Trapezoidal
4. Output: Analog Signal; 12 bit  $\pm 10$  VDC
5. Position Feedback: 750.000 counts/sec incremental encoder (single ended or differential)
6. Encoder Supply: +5 or +12VDC
7. Jumper selectable
8. Encoder Inputs: Differential (-7 to +7 VCD) or TTL
9. Jog Input: 2 dedicated inputs (low true)

10. Inputs (TTL): Limit+; Limit-; Coarse Home; Index; Amplified Fault
11. Outputs (TTL): Amplifier Enable

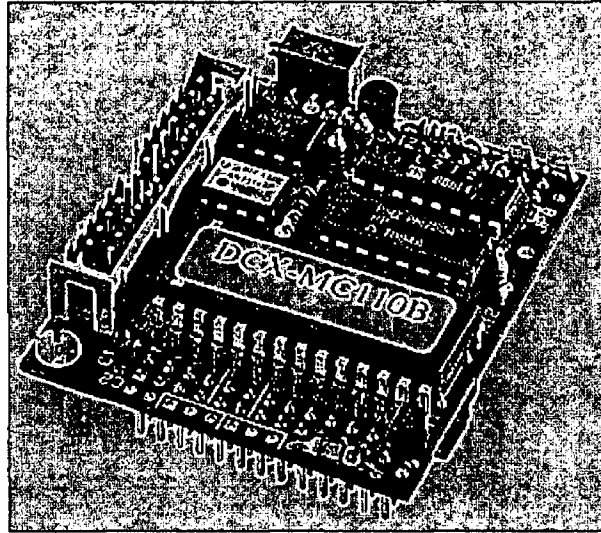


Figure E.2: DCX – MC110 Motion Control Modules

### E.3 Actuator Specifications

1. Motorized Actuator: 12V DC Servo Motor
2. Mirror Mount Drop-in Replacement for ¼-80 Actuators
3. Actuator Travel: 12mm
4. 0.05  $\mu\text{m}$  Minimum Incremental Move
5. Compatible with Many Standard Controllers/Drivers
6. Limit Switches Prevents Accidental Actuator Damage
7. High Precision Rotary Encoder (48 counts per revolution)
8. Speed Range 50-425  $\mu\text{m/s}$



Figure E.3: Motorized Actuator.

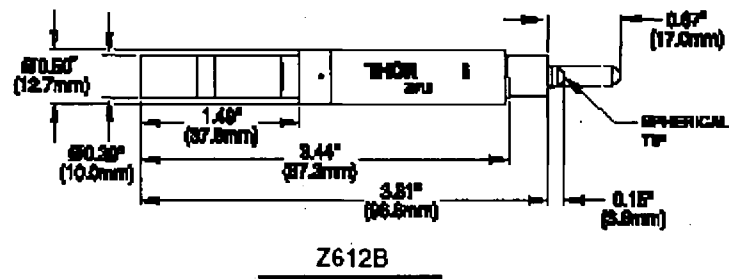


Figure E.4: Mechanical drawing of Thorlabs Z612B 12mm Motorized Actuator.

# Appendix F – Servo tuning procedure

Table of Contents	Page
Tuning Step #1	132
Tuning Step #2	132
Tuning Step #3	133
Tuning Step #4	134
Tuning Step #5	135

## List of Figures

Figure F.1	Servo tuning step 1 (Test setup)	132
Figure F.2	Servo tuning step 2 (Motion and PID setup)	133
Figure F.3	Servo tuning step 3	134
Figure F.4	Servo tuning step 4	135

## Appendix F

**Tuning Step #1** Open the Servo Tuning Utility (Start\Programs\Motion Control\Motion Integrator\Servo Tuning). From the menu bar select **Setup** and then **Test Setup**. Configure the Test Setup dialog as shown figure F.1, 100 counts and 500 ms are used as typical test setup.

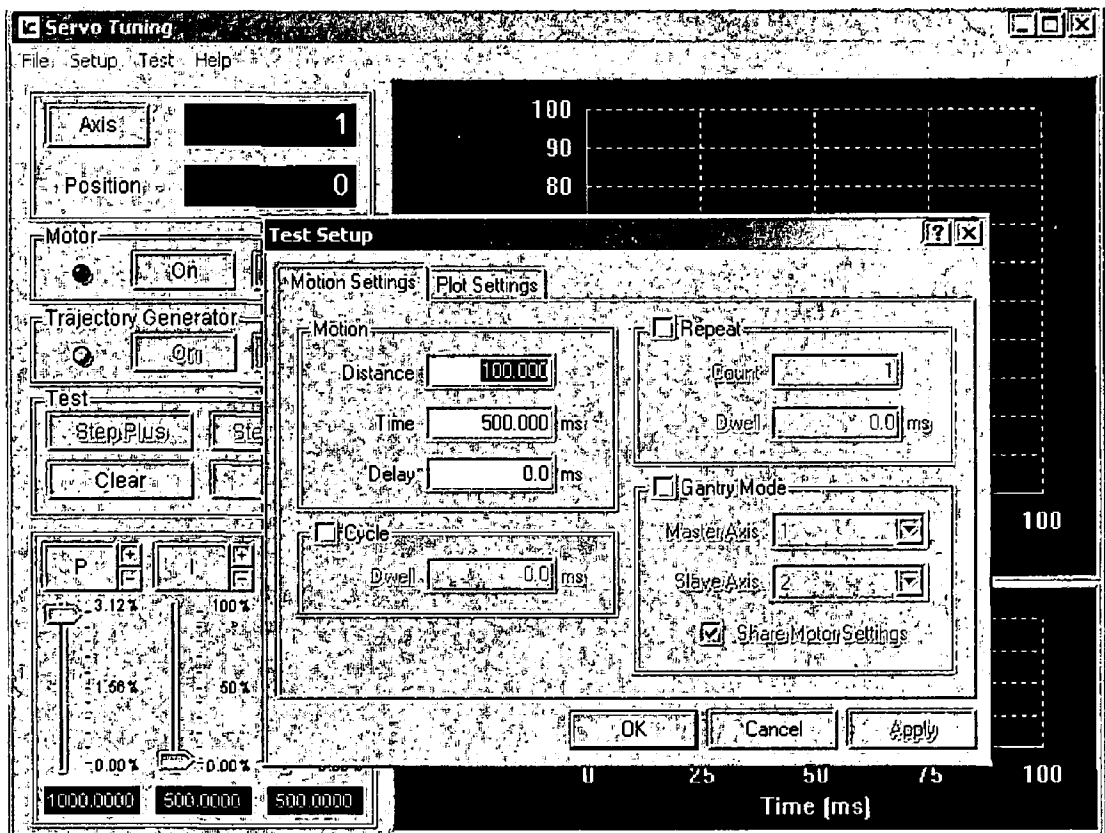


Figure F.1: Servo tuning step 1 (Test setup).

**Tuning Step# 2** Set following motion and PID filter values. Servo tuning utility for setting Motion and PID is shown in figure F.2.

Motion and PID setup was used for develop inspection system:

Acceleration = 10000

Max. Velocity = 9000

Proportional Gain = 1000

Integral Gain = 500

Integration Limit = 50

Derivative Gain = 500

Derivative Sampling = 0.005115

Following Error = 32000

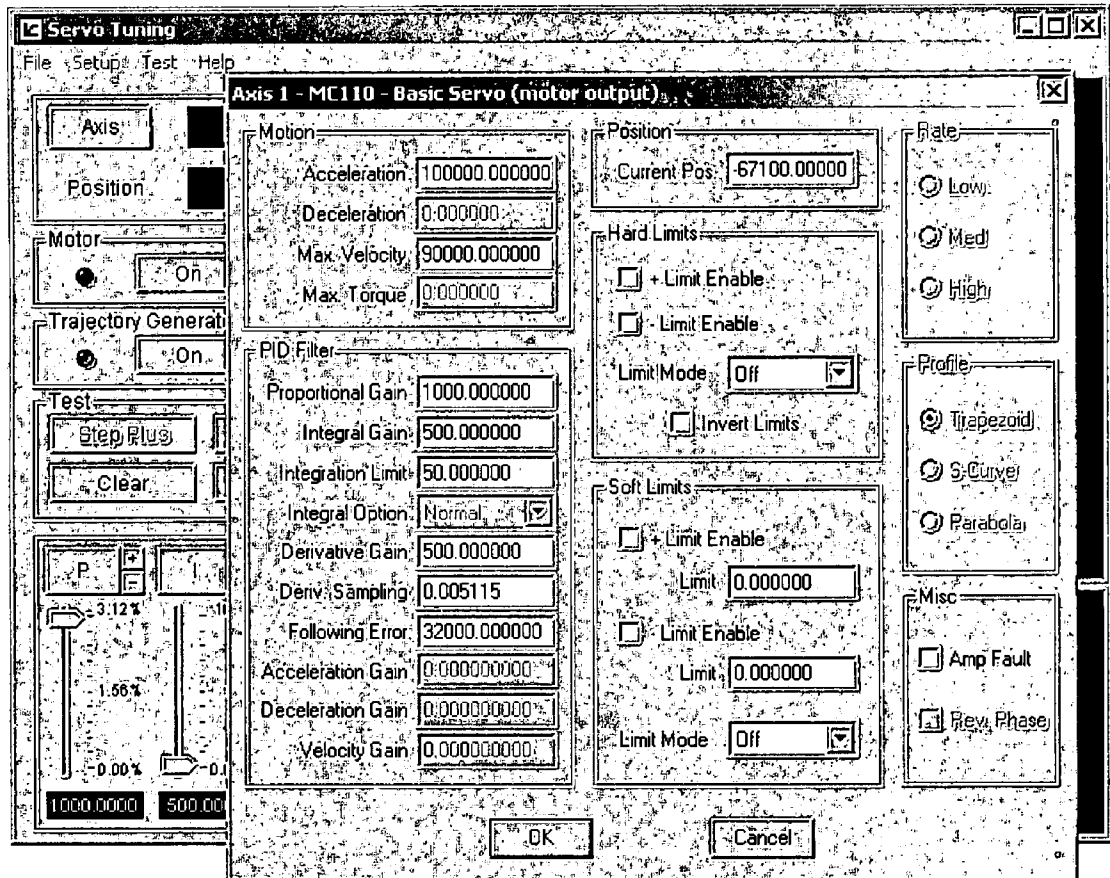


Figure F.2: Servo tuning step 2 (Motion and PID setup).

**Tuning Step #3** Turn on the axis and turn off the Trajectory Generator. While setting proportional and derivative gain, the step response should occur with the Trajectory Generator disabled. This will result in the magnitude of the output signal being determined only by a PD filter, the controller will not apply a maximum velocity or ramping (acceleration/deceleration), shown in figure F.3.

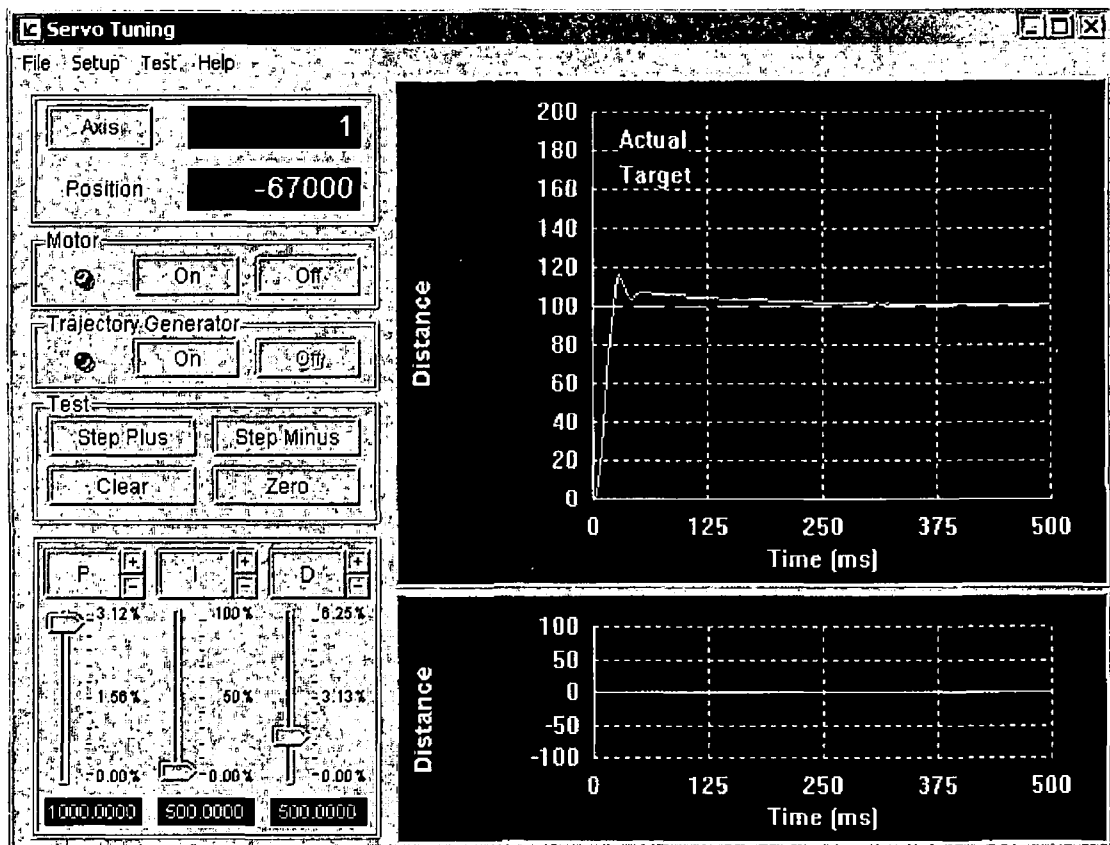


Figure F.3: Servo tuning step 3.

**Tuning Step #4** Turn on the axis and the Trajectory Generator. With the Trajectory generator turned on, the user can execute 'real world' moves displaying the calculated position, actual position, and following error plots as shown in figure F.4.

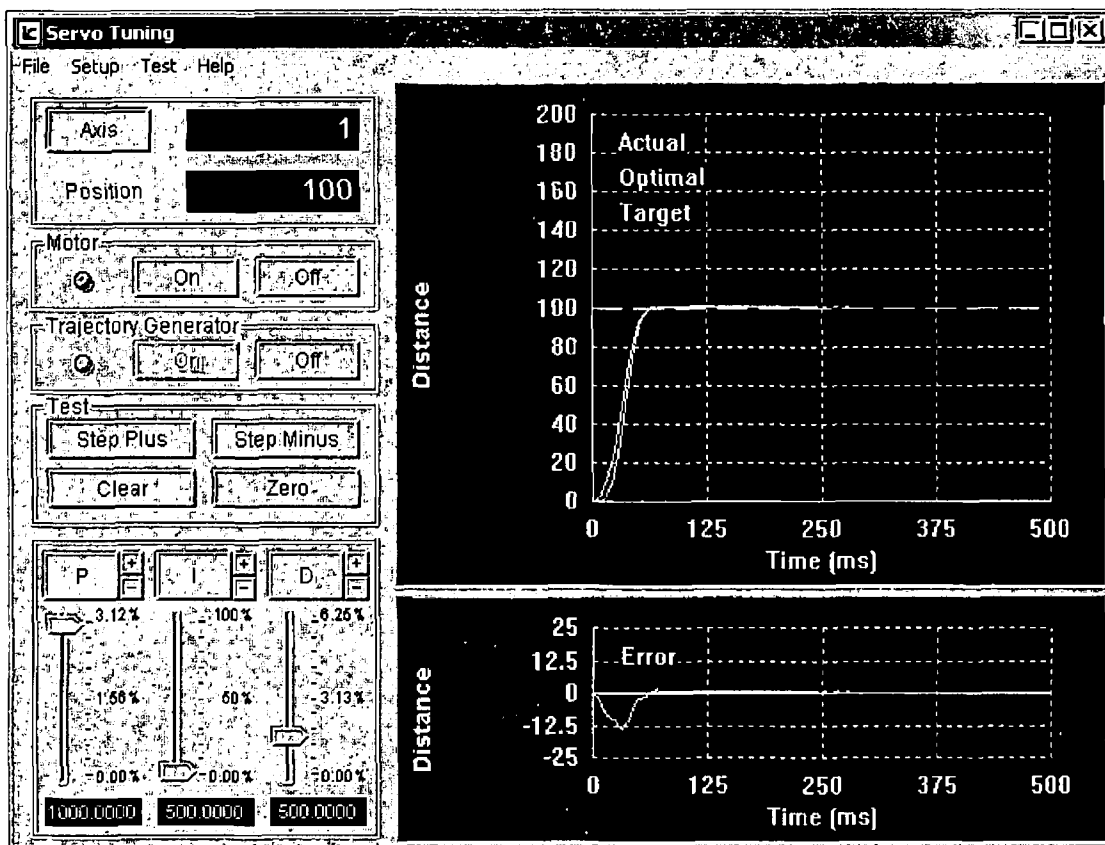


Figure F.4: Servo tuning step 4.

**Tuning Step #5 Saving the Tuning Parameters.** When servo tuning is complete, closing the tuning utility will prompt this message about saving the Auto Initialize settings, selecting **Yes** will store all settings for all installed axes in the MCAPI.INI file (in the Widows folder). Selecting **No** will cause all settings to be discarded.

# Appendix G – Call Library Function general configuration

Table of Contents	Page
G.1 General configuration of LabView call library function	137
G.2 Calling Conventions (Windows)	140

## List of Figures

Figure G.1	Call Library Function location in Function Palette	138
Figure G.2	Call Library Function Dialog Box and updated node	138
Figure G.3	Functions download from DLL by Call Library Function node	139

# Appendix G

## G.1 General configuration of LabView call library function

This section focuses on LabView software that was used for system automation. LabView is specifically designed to quickly implement a computer-controlled data gathering, analysis and display. It can be extensively customized to suit user requirements. A GUI panel explains any program and subprogram that the user can see and interact with object icons representing program functions. The graphical program is called a block diagram. Camera interfacing with LabView was a very important part of this work because the CCAM camera interface was not previously available through LabView program. LabView Call Library Function was use for interfacing camera with LabView.

The LabView Call Library Function Node is a block diagram objects that links source code written in a conventional programming language to Lab View. This appears on the block diagram as an icon with input and output terminals. Linking external code to LabView includes the following actions:

1. Compile the source code and link it to form executable code. If a compiled DLL available, this step is not necessary.
2. LabView calls the executable code when the Call Library Function Node executes.
3. LabView passes input data from the block diagram to the executable code.
4. LabView returns data from the executable code to the block diagram.

Figure G.1 shows the Call Library Function object on the block diagram. Location of this function as on the **Functions»Advanced** palette.

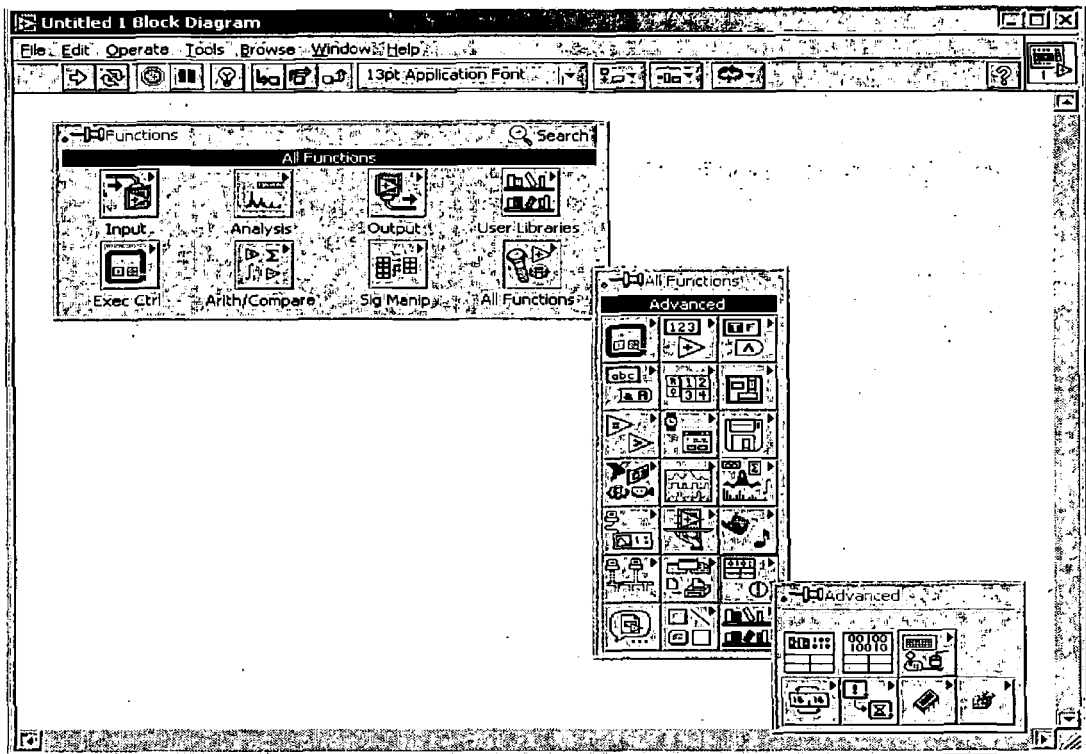


Figure G.1: Call Library Function location in Function Palette.

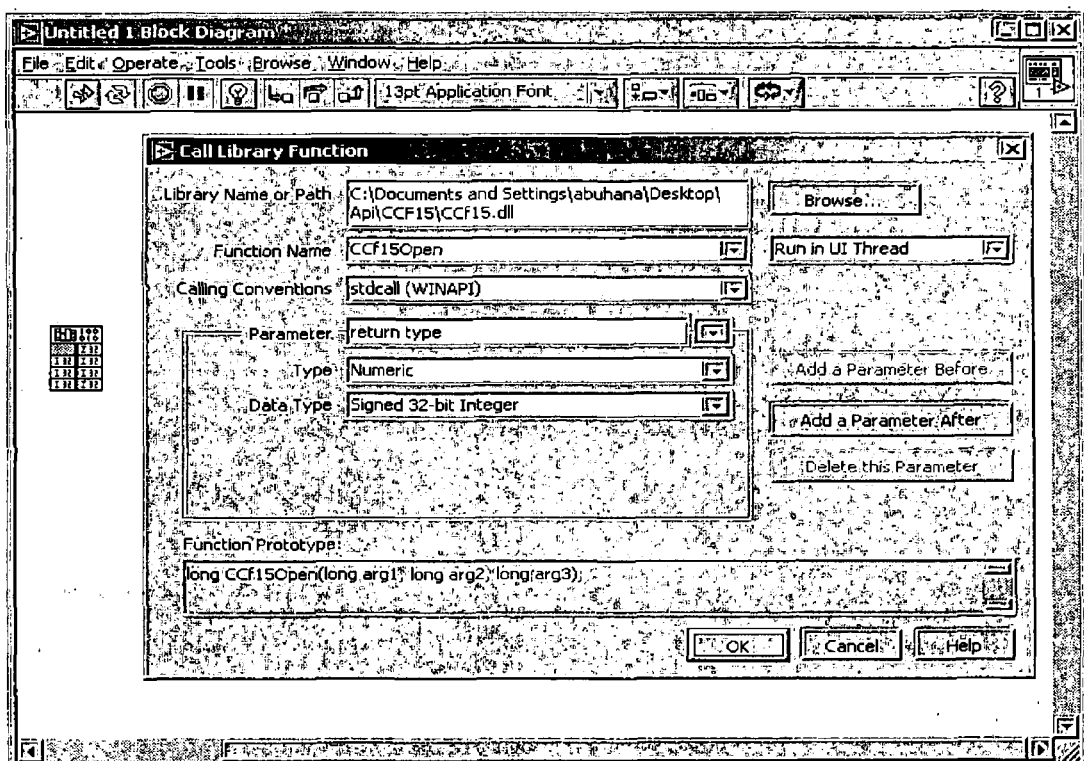


Figure G.2: Call Library Function Dialog Box and updated node.

Right-click the icon and select **Configure** in the shortcut menu to access the **Call Library Function** dialog box where specify the library, function, parameters, return value for the object, and calling conventions in Windows. When click **OK** in the dialog box, LabView updates the icon according to settings, displaying the correct number of terminals and setting the terminals to the correct data types. Figure G.2 shows the downloaded functions name in Call Library function dialog box after defining library or DLL location in Library Name or Path. Also download all functions from specific library. Figure G.3 shows the **Call Library Function** dialog box in block diagram with updated input and output terminals [59].

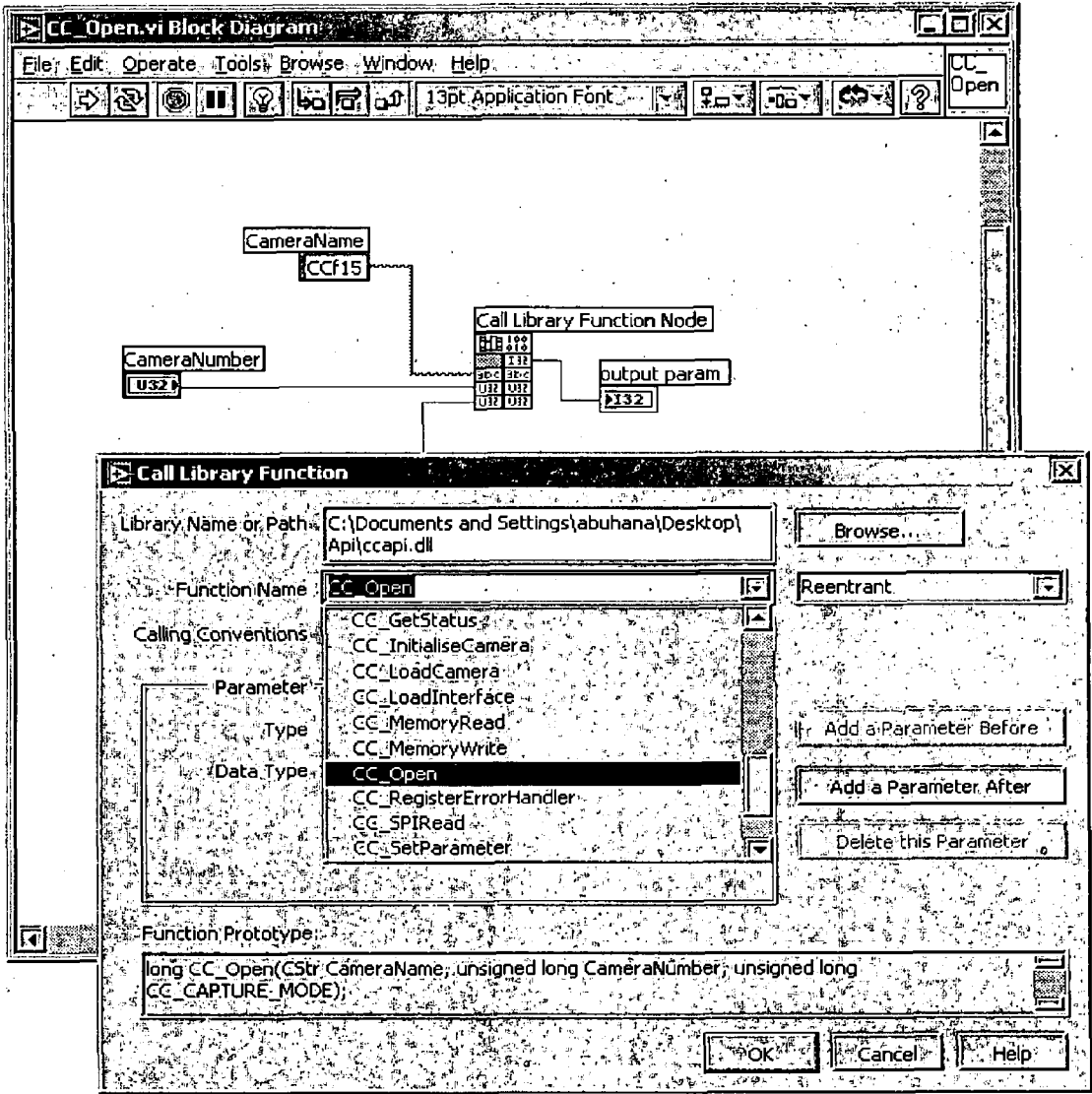


Figure G.3: Functions download from DLL by Call Library Function node.

According to configure parameters, the **Function Prototype** area displays the C prototype for the building function. The return value for the function returns to the right terminal of the top pair of terminals of the object. If there is no return value, this pair of terminals is unused. Each additional pair of terminals corresponds to a parameter in the functions parameter list. To pass a value to the function, wire to the left terminal of a terminal pair. To read the value of a parameter after the function call, wire from the right terminal of a terminal pair.

## G.2 Calling Conventions (Windows)

Use the **Calling Conventions** pull-down menu in the **Call Library Function** dialog box to select the calling conventions for the function. The default calling convention is C. We can also use the standard Windows calling convention, `__stdcall`. Refer to the documentation for the DLL we want to call for the appropriate calling conventions. **Parameters** Initially, Call Library Function has no parameters and has a return value of **Void**. To add parameters to the function, click the **Add a Parameter Before** or **After** buttons. To remove a parameter, click the **Delete this Parameter** button. Use the **Parameter** pull-down menu to select different parameters or the return value. The parameter name does not affect the call, but it is propagated to output wires.

Use the **Type** pull-down menu to indicate the type of each parameter. For return type, you can set **Type** to **Void**, **Numeric**, or **String**. **Void** is only available for return type and is not available for parameters. Use **Void** for the return type if the function does not return any values. Even if the function we call returns a value, we can use **Void** for the return type. When the function returns a value and we select **Void** as the return type, the value returned by the function is ignored [57].

## Appendix H – CCAPI.H Header file

```
/* CCapi.h */

#include "windows.h" -- must be included by application
#ifndef DLLIMPORT
#ifndef DLLEXPORT
// should not happen
#define DLLINOUT
#else
#define DLLINOUT __declspec( dllexport )
#endif
#else
#define DLLINOUT __declspec( dllimport )
#endif

#ifdef __cplusplus
extern "C" { /* Assume C declarations for C++ */
#endif /* __cplusplus */

typedef enum {
    CC_NO_TRIGGER = 0x0,
    CC_INTERFACE_TRIGGER_SINGLE,
    // if interface card supports trigger input - I/F sends start command
    CC_INTERFACE_TRIGGER_CONTINUOUS,
    // if interface card supports trigger input - I/F sends start command
    CC_CAMERA_TRIGGER_SINGLE,
    // if camera supports trigger input
    CC_CAMERA_TRIGGER_CONTINUOUS,
    // if camera supports trigger input
    CC_CAMERA_CONTINUOUS,
    // successive singleshots - as fast as it goes
    // only supported with Arm/Data
    CC_CAMERA_CONTINUOUS_TIMED,
    // successive singleshots - timed, but may be slower due to large integration time
    CC_CAMERA_CONTINUOUS_ROLLING
    // continuous rolling shutter operation for BCi4 / BCi5 only supported with
    Arm/Data
} CC_TRIGGER_MODE ;

typedef enum {
    CC_CAPTURE_WAIT = 0x0,
    CC_CAPTURE_NOWAIT,
} CC_CAPTURE_MODE ;

typedef enum {
    CC_PAR_INTEGRATION_TIME = 0x0,
```

```

CC_PAR_GAIN,
CC_PAR_OFFSET,
CC_PAR_DATA_MODE,
CC_PAR_PIXEL_PRECHARGE,
CC_PAR_CAMERA_MODE,
CC_PAR_YSTART,
CC_PAR_YINC,
CC_PAR_YEND,
CC_PAR_XSTART,
CC_PAR_XINC,
CC_PAR_XEND,
CC_PAR_PWM,
CC_PAR_ADC_DELAY,
CC_PAR_Y_DELAY,
CC_PAR_X_DELAY1,
CC_PAR_X_DELAY2,
CC_PAR_SENSOR_RESET,
CC_PAR_SENSOR_CALIBRATE,
CC_PAR_CORRECTION_MODE,
CC_PAR_ANAVAL0,
CC_PAR_ANAVAL1,
CC_PAR_ANAVAL2,
CC_PAR_ANAVAL3,
CC_PAR_ANAVAL01P,
CC_PAR_ANAVAL23P,
CC_PAR_CTRLBIT,
CC_PAR_YPARK,
CC_PAR_XPARK,
CC_PAR_LINE_CNT,
CC_PAR_LINE_TIME,
CC_PAR_ANASEL,
CC_PAR_GAIN_RED,
CC_PAR_GAIN_GREEN,
CC_PAR_GAIN_BLUE,
CC_PAR_NLIST_OPS,
CC_PAR_RESET_SM,
CC_PAR_INTERFACE_FLASH_DELAY,
CC_PAR_INTERFACE_FLASH_WIDTH,
CC_PAR_INTERFACE_FLASH_SETTINGS,
CC_PAR_SKIP_XNCS_WAIT,
CC_PAR_OFFSET_B_FINE,
CC_PAR_INTSEL,
CC_PAR_CAMERA_FLASH_DELAY,
CC_PAR_CAMERA_FLASH_WIDTH,
// CC_PAR_CAMERA_FLASH_SETTINGS,
CC_PAR_CAMERA_TRIGGER_SETTINGS,
CC_PAR_OFFSET_RED,
CC_PAR_OFFSET_GREEN,
CC_PAR_OFFSET_BLUE,
CC_PAR_REPEAT_TIME

```

```
    } CC_PARAMETER ;
```

```
enum CC_SELDAC {  
    DAC0 = 0x0 ,  
    DAC1 = 0x1000 ,  
    DAC2 = 0x2000 ,  
    DAC3 = 0x3000 ,  
    DAC4 = 0x4000 ,  
    DAC5 = 0x5000 ,  
    DAC6 = 0x6000 ,  
    DAC7 = 0x7000 ,  
    DAC8 = 0x8000 ,  
    DAC9 = 0x9000 ,  
    DAC10= 0xa000 ,  
    DAC11= 0xb000 ,  
    DAC12= 0xc000 ,  
    DAC13= 0xd000 ,  
    DAC14= 0xe000 ,  
    DAC15= 0xf000 ,  
};
```

```
typedef enum {  
    CC_CAMERA_NORMAL = 0x0,  
    CC_CAMERA_DIAG_X,  
    CC_CAMERA_DIAG_Y,  
    CC_CAMERA_DIAG_X_XOR_Y  
} CC_CAMERA_MODE ;
```

```
typedef enum {  
    CC_WOI_LEFTTOP_RIGHTBOTTOM = 0x0,  
    CC_WOI_LEFTTOP_WIDTHHEIGHT,  
    CC_WOI_CENTER_WIDTHHEIGHT,  
    CC_WOI_RIGHTBOTTOM_WIDTHHEIGHT,  
} CC_WOI_MODE ;
```

```
typedef enum {  
    CC_CORRECTION_OFF = 0x0,  
    CC_CORRECTION_FPN,  
    CC_CORRECTION_PRNU,  
    CC_CORRECTION_BAD_PIX,  
    CC_CORRECTION_CORR_DATA,  
} CC_CORRECTION_MODE ;
```

```
typedef enum {  
    CC_DATA_8BIT_7_DOWNT0_0 = 0x0,  
    CC_DATA_8BIT_8_DOWNT0_1,  
    CC_DATA_8BIT_9_DOWNT0_2,  
    CC_DATA_8BIT_11_DOWNT0_4,  
    CC_DATA_16BIT_9_DOWNT0_0,
```

```

CC_DATA_16BIT_11_DOWNT0_2,
CC_DATA_16BIT_11_DOWNT0_0,
CC_DATA_8BIT_10_DOWNT0_3,
} CC_DATA_MODE;

```

```

typedef enum {
    CC_ERROR_NOTIFICATION_HANDLED_BY_APPLICATION = 0,
    CC_ERROR_NOTIFICATION_HANDLED_BY_CALLBACK,
    CC_ERROR_NOTIFICATION_HANDLED_BY_API_MESSAGEBOX
} CC_ERROR_NOTIFICATION;

```

```

typedef enum {
    CC_CAMERA_STATUS_CC = 0,
    CC_CAMERA_STATUS_ASTAT
} CC_CAMERA_STATUS;

```

```

typedef enum {
    // this enum will not be used as such, because all values can be ored
    // but we preferred to group it this way
    CC_FLASH_SETTINGS_DAI5Y = 0x80,
    CC_FLASH_SETTINGS_INVERT_ARMIN = 0x01,
    CC_FLASH_SETTINGS_INVERT_TRIGGERIN = 0x02,
    CC_FLASH_SETTINGS_INVERT_ARMEDOUT = 0x04,
    CC_FLASH_SETTINGS_INVERT_FLASHOUT = 0x08
} CC_FLASH_SETTINGS;

```

```

typedef enum {
    CC_CAMERA_TRIGGER_INVERT_TRIGGER_IN = 0x01,
    CC_CAMERA_TRIGGER_INVERT_TRIGGER_OUT = 0x02,
    CC_CAMERA_TRIGGER_ARM = 0x04,
    CC_CAMERA_TRIGGER_ARMED_OUTPUT = 0x08
} CC_CAMERA_TRIGGER_SETTINGS;

```

```

DLLINOUT BOOL WINAPI CC_GetDriverVersion( HANDLE Cam,
    DWORD * pVersionNumber );

```

```

DLLINOUT BOOL WINAPI CC_GetDLLVersion( DWORD *
    pVersionNumber );

```

```

DLLINOUT BOOL WINAPI CC_RegisterErrorHandler( HANDLE Cam,
    CC_ERROR_NOTIFICATION operation, void (*
    CallbackFunction)( int ));

```

```

DLLINOUT HANDLE WINAPI CC_Open( LPCSTR CameraName,
    ULONG CameraNumber, CC_CAPTURE_MODE CaptureMode );

```

```

DLLINOUT BOOL WINAPI CC_Close( HANDLE Cam );

```

```

DLLINOUT  BOOL WINAPI      CC_LoadInterface( HANDLE Cam , char *
FileSpec ) ;

DLLINOUT  BOOL WINAPI      CC_LoadCamera( HANDLE Cam , char *
FileSpec ) ;

DLLINOUT  BOOL WINAPI      CC_GetPCIBoardInfo( ULONG
CameraNumber, char * pBoardType, char * pBoardRev ) ;

DLLINOUT  BOOL WINAPI      CC_CaptureSingle( HANDLE Cam , PVOID
Buffer , ULONG TransferSize , CC_TRIGGER_MODE TriggerMode
, USHORT TimeOut ,OVERLAPPED * pUserOverlapped ) ;

DLLINOUT  BOOL WINAPI      CC_CaptureContinuous( HANDLE Cam ,
PVOID Buffer , ULONG BufferSize , ULONG NotificationInterval ,
ULONG FrameSize , void (* CallbackFunction)( void ) , HANDLE
UserEven CC_TRIGGER_MODE TriggerMode , USHORT TimeOut
) ;

DLLINOUT  BOOL WINAPI      CC_CaptureSequence( HANDLE Cam ,
PVOID Buffer , ULONG BufferSize , ULONG NumberOfFrames ,
ULONG NotificationInterval ,      ULONG FrameSize , void (*
CallbackFunction)( void ) , CC_TRIGGER_MODE TriggerMode ,
USHORT TimeOut ) ;

DLLINOUT  BOOL WINAPI      CC_CaptureWait( HANDLE Cam ) ;
DLLINOUT  BOOL WINAPI      CC_CaptureStatus( HANDLE Cam ) ;
DLLINOUT  BOOL WINAPI      CC_CaptureAbort( HANDLE Cam ) ;

DLLINOUT  BOOL WINAPI      CC_SetWOI( HANDLE Cam , USHORT
XPar1 , USHORT YPar1 , USHORT XPar2 , USHORT YPar2 ,
USHORT XInc , USHORT YInc , CC_WOI_MODE WOIMode ,
ULONG *FrameSize ) ;

DLLINOUT  BOOL WINAPI      CC_SetParameter( HANDLE Cam ,
CC_PARAMETER Par , ULONG Value ) ;

DLLINOUT  BOOL WINAPI      CC_GetStatus( HANDLE Cam , ULONG *
Status ) ;

DLLINOUT  BOOL WINAPI      CC_GetCameraStatus( HANDLE Cam ,
CC_CAMERA_STATUS idx , ULONG * Status ) ;

/* not yet documented in CCAPI.pdf */
/* only supported by BCi4/BCi5 USB versions */
DLLINOUT  BOOL WINAPI      CC_CaptureArm( HANDLE Cam ,
CC_TRIGGER_MODE TriggerMode ) ;

```

```

DLLINOUT  BOOL WINAPI      CC_CaptureData( HANDLE Cam , PVOID
        Buffer , ULONG TransferSize , USHORT TimeOut , OVERLAPPED
        * pUserOverlapped ) ;
/* not yet documented in CCAPI.pdf */

```

```

DLLINOUT  BOOL WINAPI      CC_MemoryRead( HANDLE Cam, PVOID
        Buffer, ULONG Address, ULONG Size ) ;

```

```

DLLINOUT  BOOL WINAPI      CC_MemoryWrite( HANDLE Cam, PVOID
        Buffer, ULONG Address, ULONG Size ) ;

```

```

DLLINOUT  BOOL WINAPI      CC_CameraMemoryWrite( HANDLE Cam,
        PVOID Buffer, ULONG Address, ULONG Size ) ;

```

```

DLLINOUT  BOOL WINAPI      CC_SetRegister( HANDLE Cam , USHORT
        Register , ULONG Value ) ;

```

```

DLLINOUT  BOOL WINAPI      CC_GetRegister( HANDLE Cam , USHORT
        Register , ULONG * Value ) ;

```

```

DLLINOUT  BOOL WINAPI      CC_GetHistogramData(      HANDLE Cam
        ,USHORT *usMin ,USHORT *usGravity ,USHORT
        *usMax,ULONG *ulValue );

```

```

DLLINOUT  BOOL WINAPI      CC_GetCameraNumber( HANDLE Cam ,
        DWORD * dwCameraNumber );

```

```

#ifdef __cplusplus
}          /* End of extern "C" { */
#endif    /* __cplusplus */

```

```

/* end of CCapi.h */

```

# Appendix I – Camera program

List of Figures	Page
Figure I.1 Front panel of CAMERA.VI	148
Figure I.2 Front panel of CC_Open.vi	149
Figure I.3 Block diagram of CC_Open.vi	149
Figure I.4 Front panel of CC_LoadInterface.vi	150
Figure I.5 Block diagram of CC_LoadInterface.vi	150
Figure I.6 Front panel of Set camera parameter.vi	151
Figure I.7 Block diagram of Set camera parameter.vi	151
Figure I.8 Front panel of CC_SetWOI.vi	152
Figure I.9 Block diagram of CC_SetWOI.vi	152
Figure I.10 Front panel of CC_CaptureSingle.vi	153
Figure I.11 Block diagram of CC_Capturesingle.vi	153
Figure I.12 Front panel of WriteBMP.vi	154
Figure I.13 Block diagram of WriteBMP.vi	154
Figure I.14 Front panel of CC_Close.vi	155
Figure I.15 Block diagram of CC_Close.vi	155

# Appendix I

## LabView camera programming front panel and block diagrams of subVI's

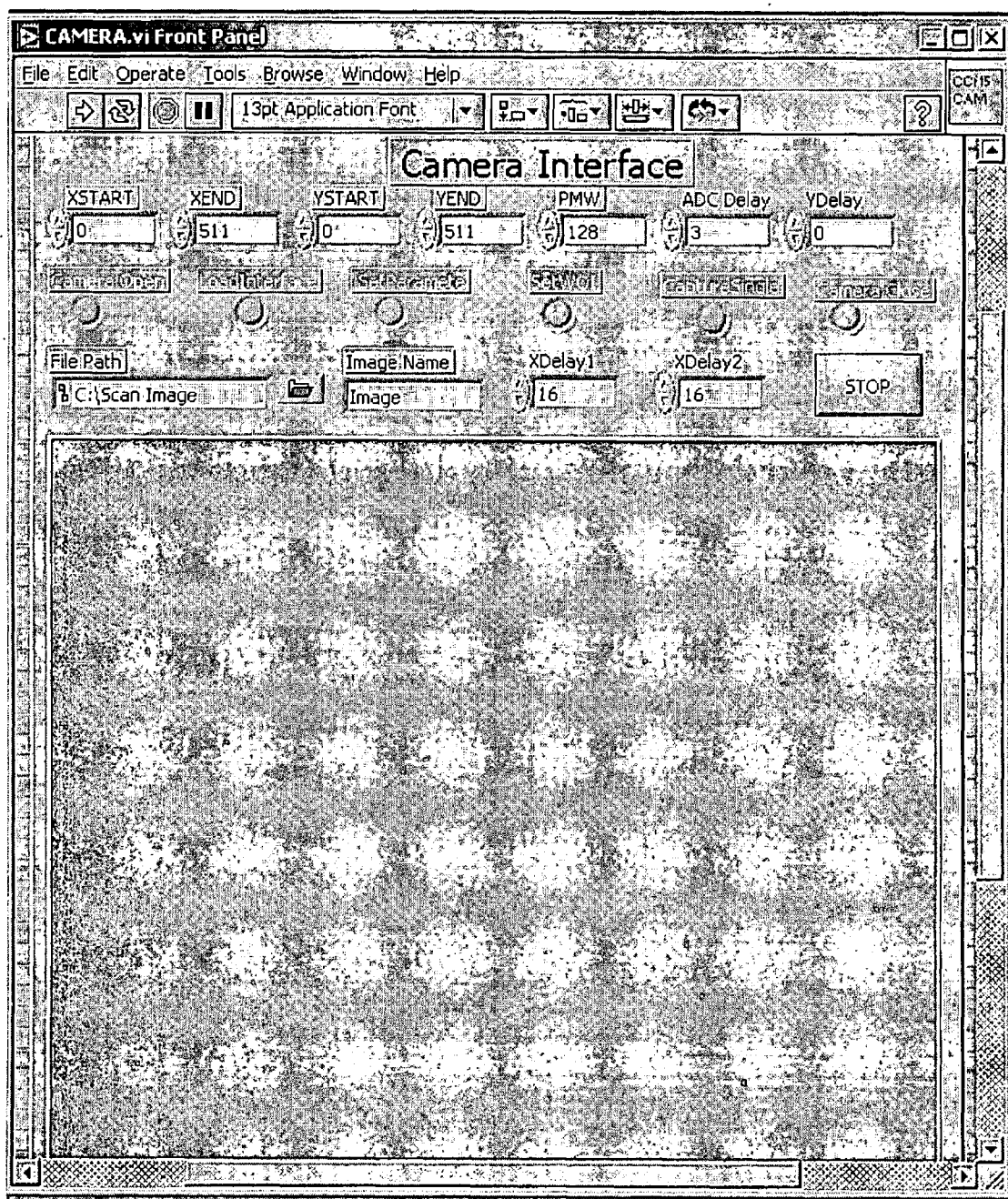


Figure I.1: Front panel of CAMERA.VI.

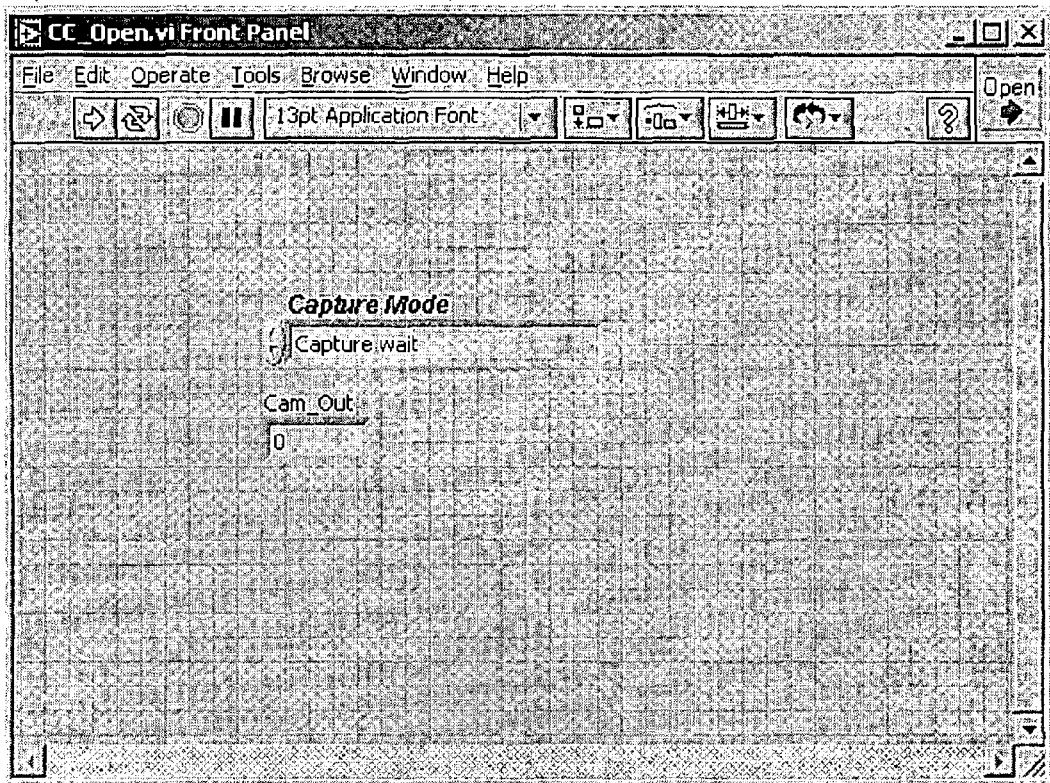


Figure I.2: Front panel of CC\_Open.vi.

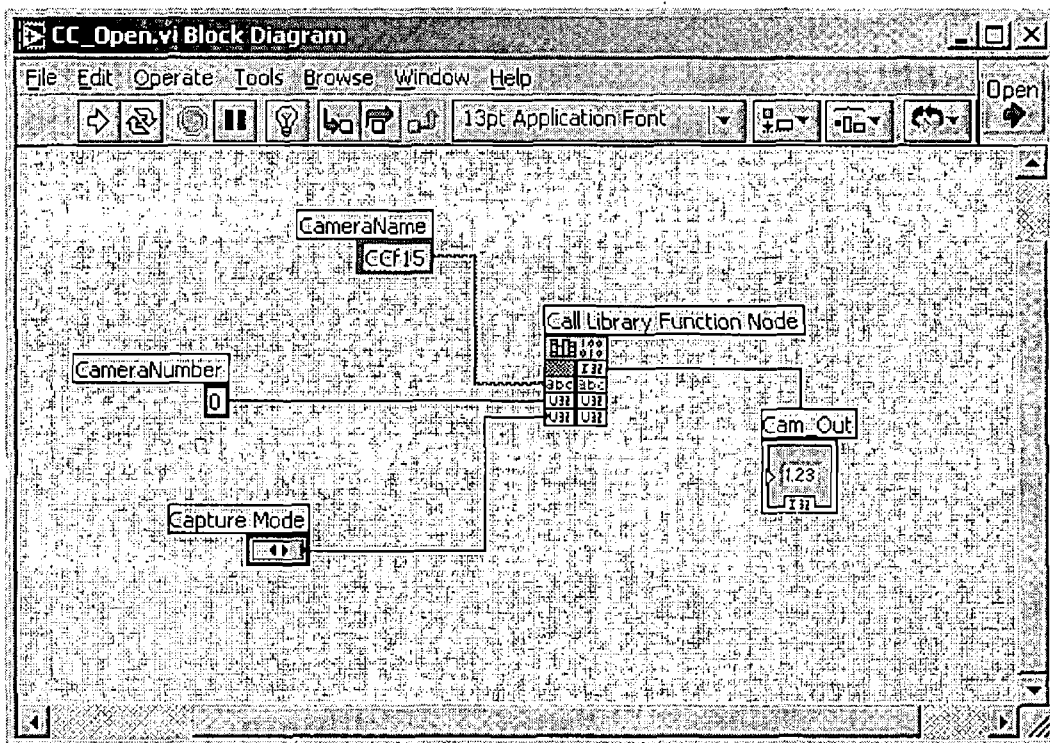


Figure I.3: Block diagram of CC\_Open.vi.

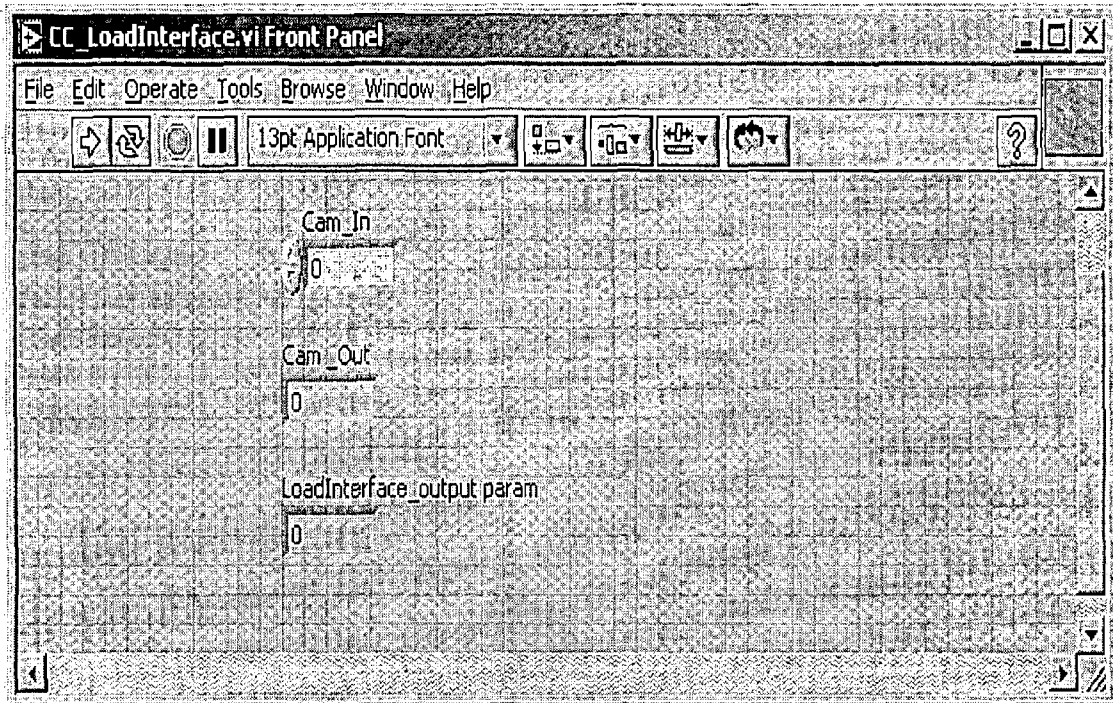


Figure I.4: Front panel of CC\_LoadInterface.vi.

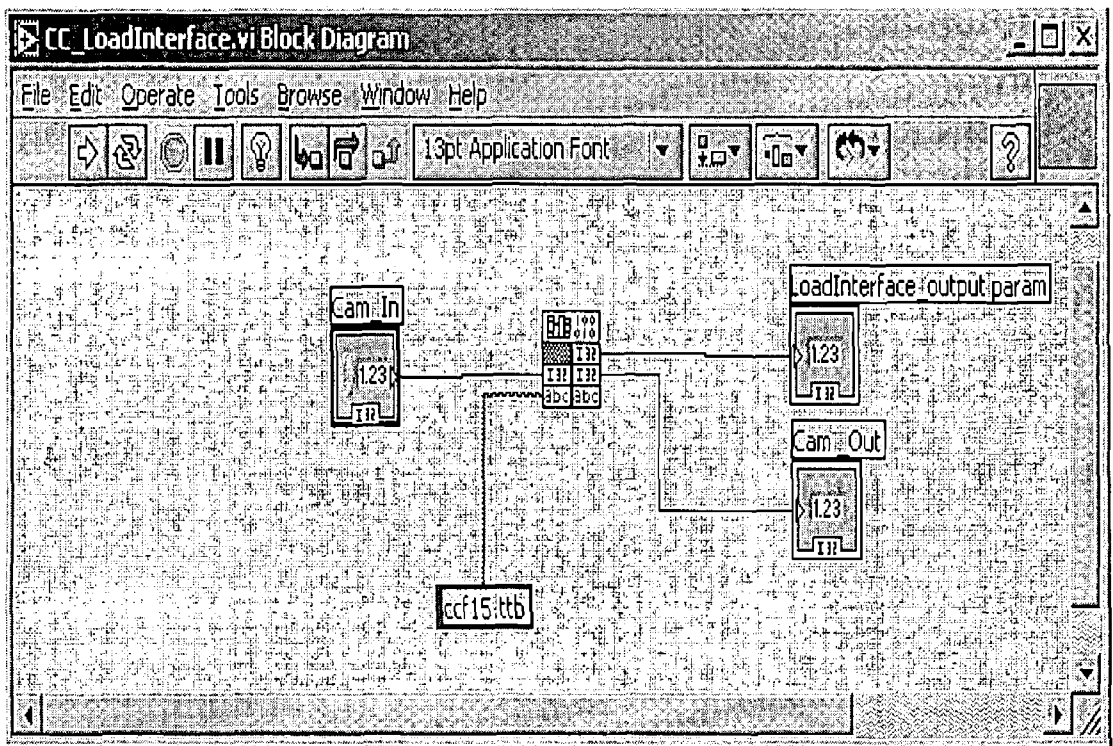


Figure I.5: Block diagram of CC\_LoadInterface.vi.

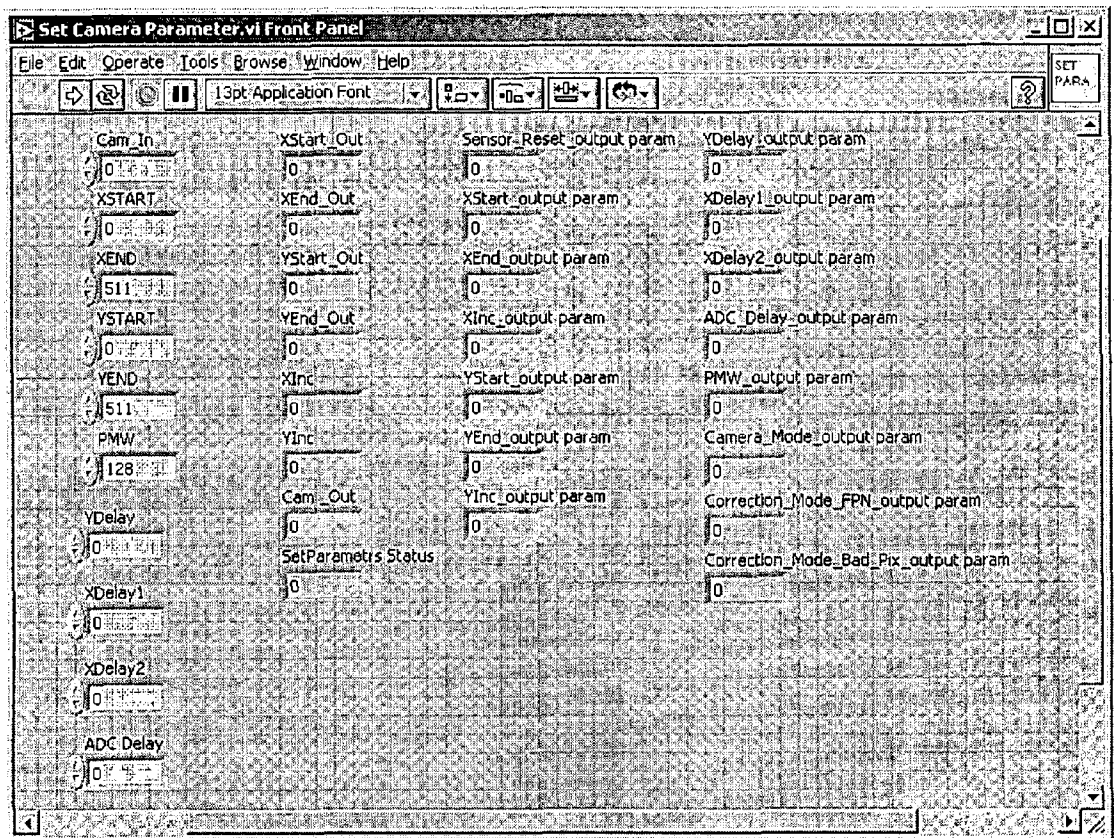


Figure I.6: Front panel of Set camera parameter.vi.

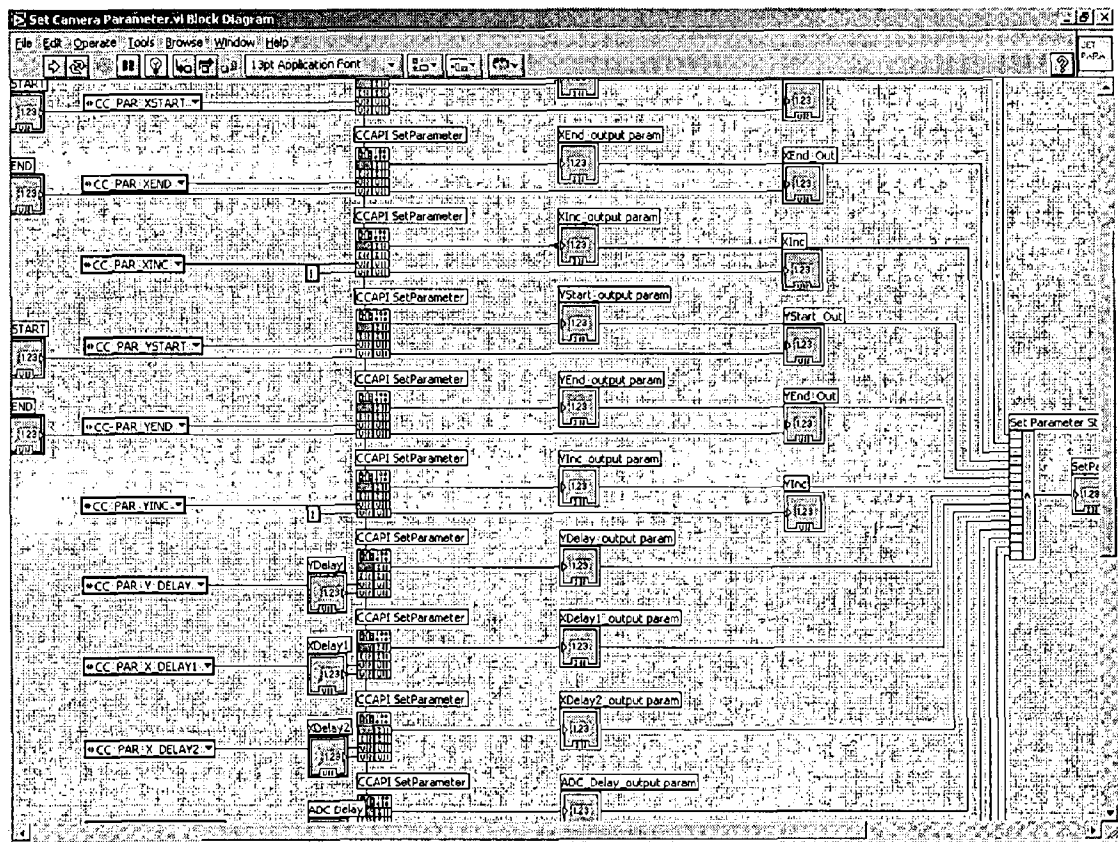


Figure I.7: Block diagram of Set camera parameter.vi.

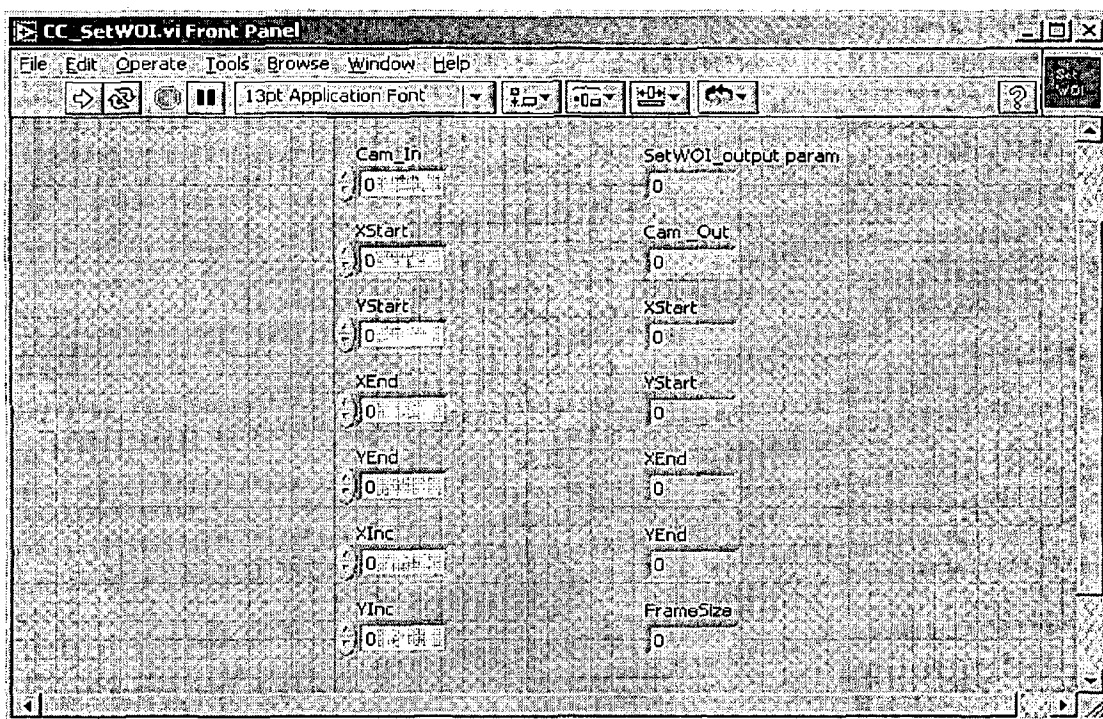


Figure I.8: Front panel of CC\_SetWOI.vi.

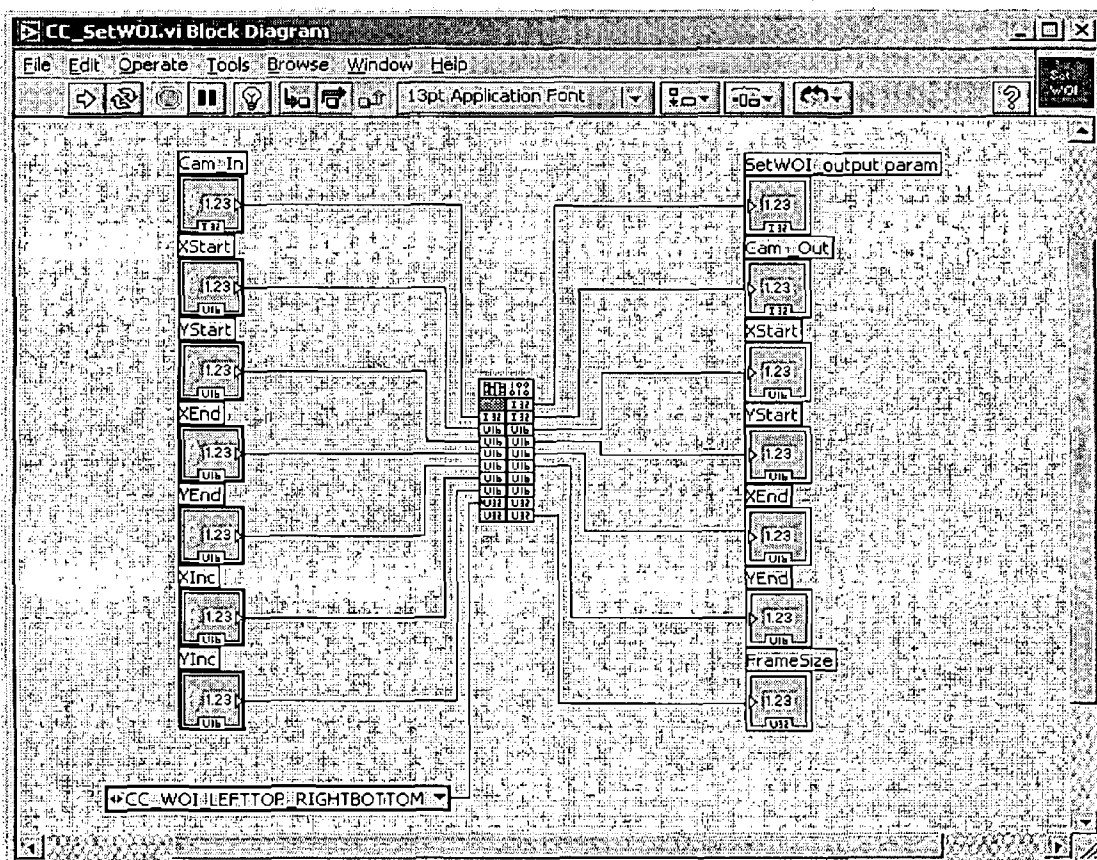


Figure I.9: Block diagram of CC\_SetWOI.vi.

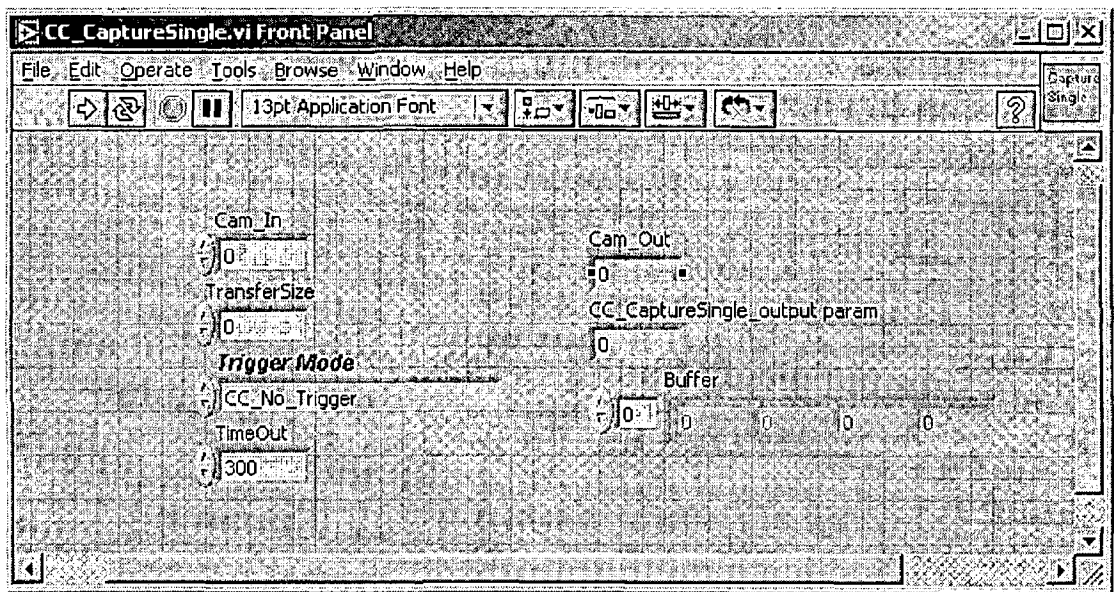


Figure I.10: Front panel of CC\_CaptureSingle.vi.

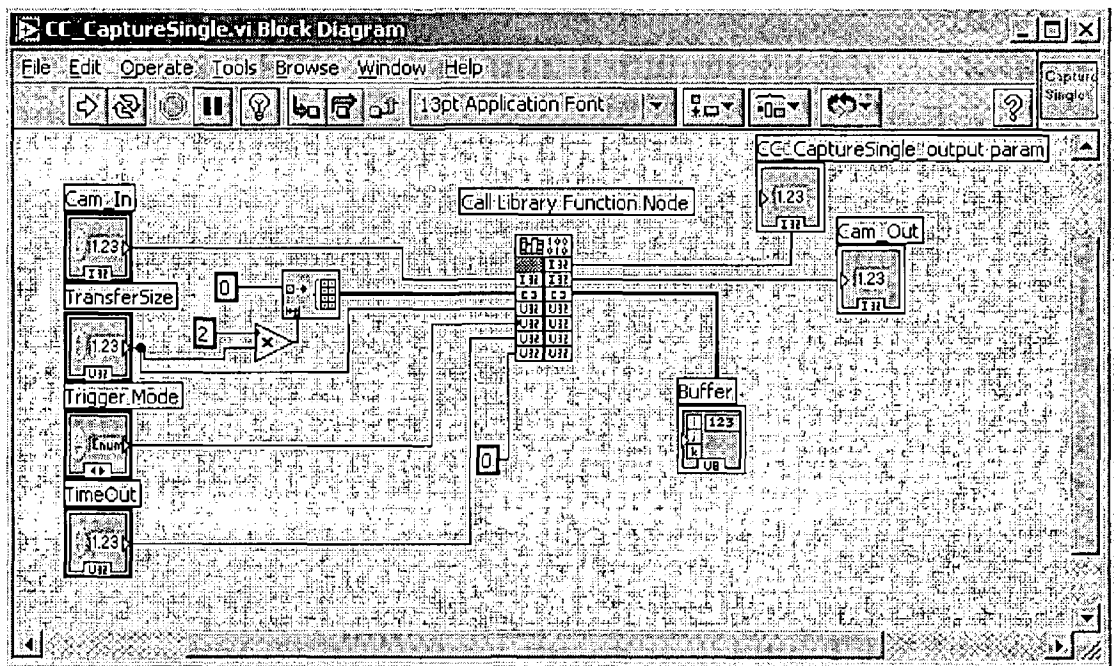


Figure I.11: Block diagram of CC\_Capturesingle.vi.

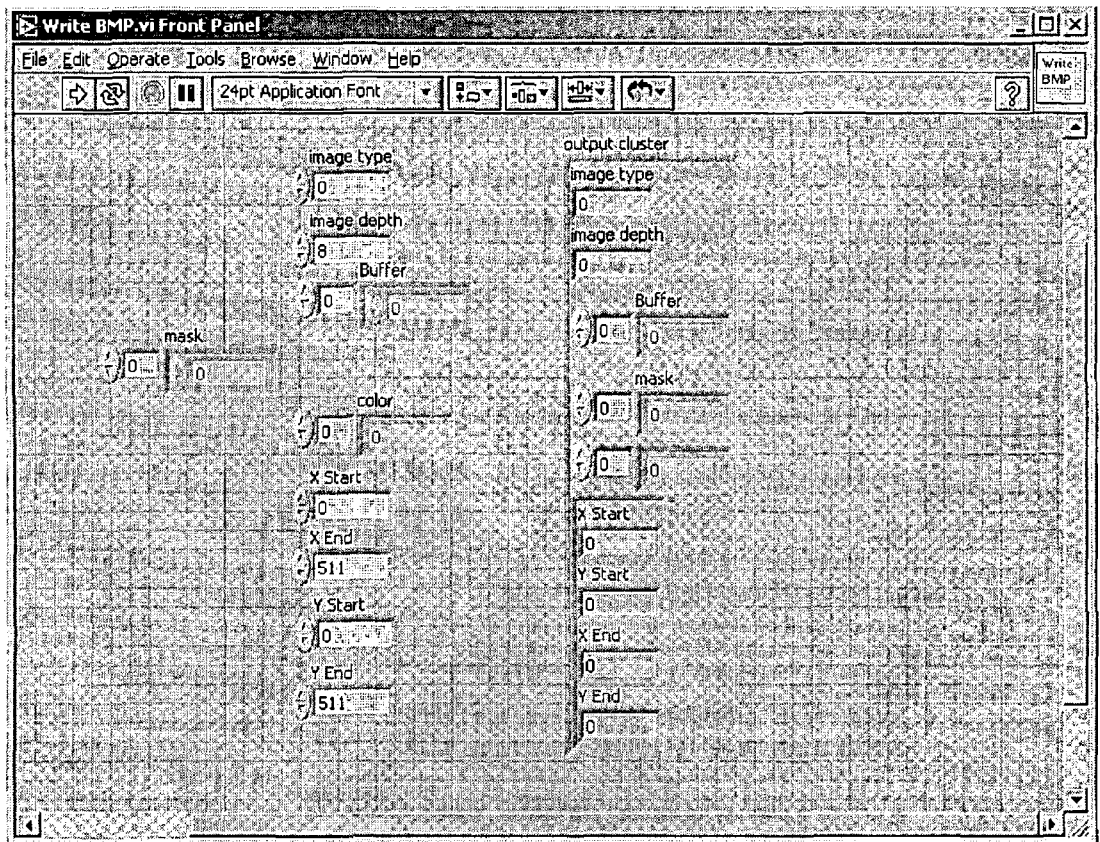


Figure I.12: Front panel of WriteBMP.vi.

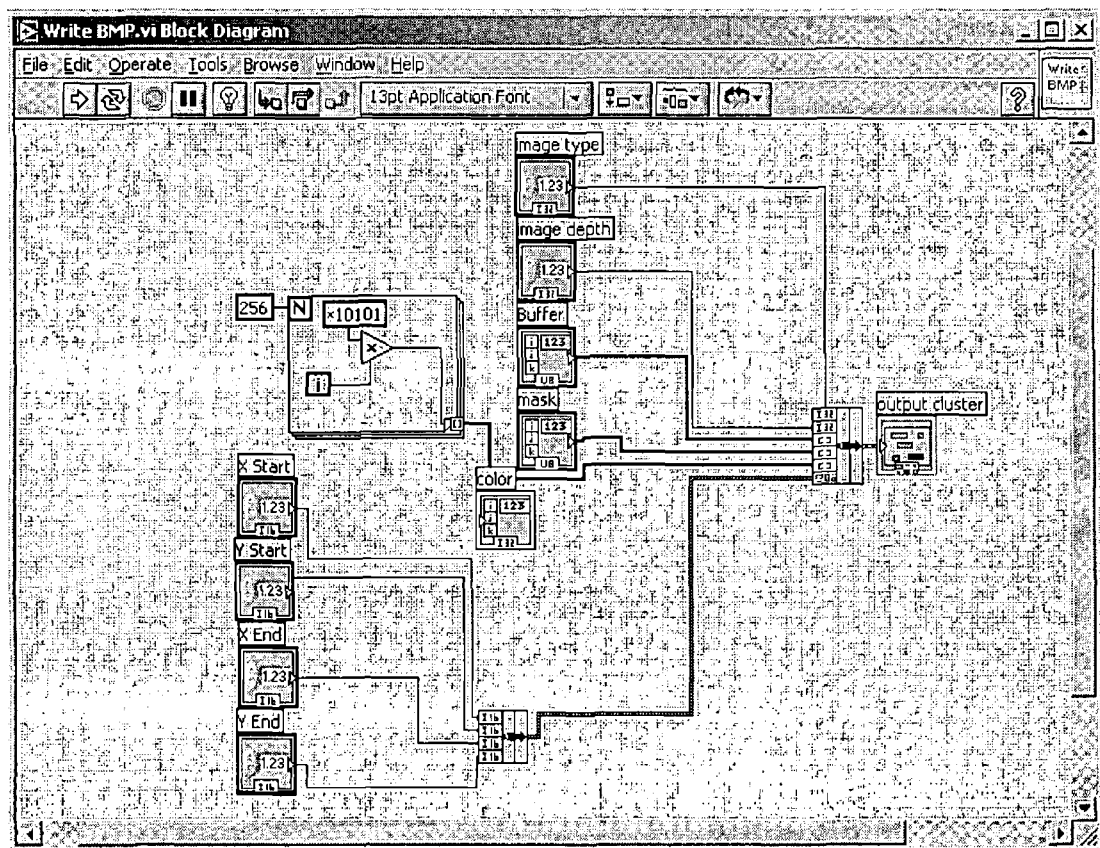


Figure I.13: Block diagram of WriteBMP.vi.

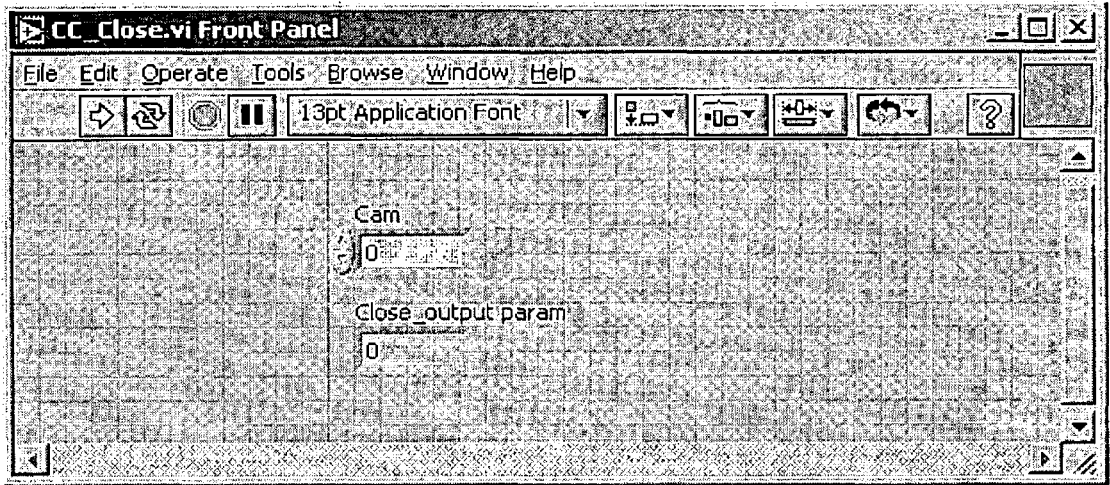


Figure I.14: Front panel of CC\_Close.vi.

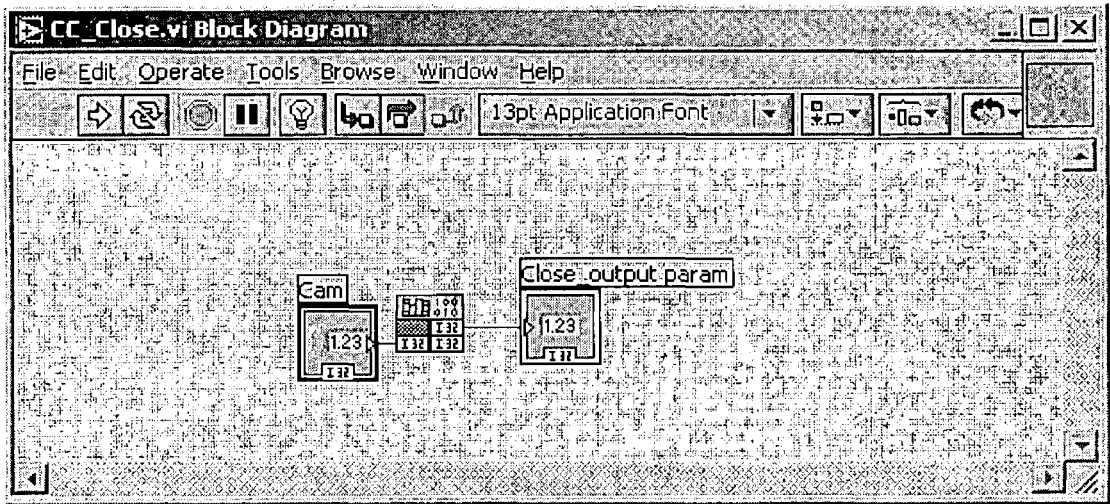


Figure I.15: Block diagram of CC\_Close.vi.